NASA CR-134687

127

NASA

2.5 kW ADVANCED TECHNOLOGY ION THRUSTER

FINAL REPORT

BY

ION PHYSICS DEPARTMENT STAFF
HUGHES RESEARCH LABORATORIES
A DIVISION OF HUGHES AIRCRAFT COMPANY
3011 MALIBU CANYON ROAD
MALIBU, CALIFORNIA 90265

PREPARED FOF

NATIONAL AERONAUTICS AND SPACE ADMINISTRATION
NASA LEWIS RESEARCH CENTER

CONTRACT NAS 3-16949

DAVID BYERS, PROGRAM MANAGER

1. Report No.	2. Government Accession No.	3. Recipient's Catalog No.
NASA CR-134607		

4. Title and Subtitle	5. Report Date
2.5 kW ADVANCED TECHNOLOGY ION THRUSTER	August 1974
	6. Performing Organization Code
7. Author(s)	8. Performing Organization Report No.
R. L. Poeschel, et al.	
9. Performing Organization Name and Address	10. Work Unit No.
Hughes Research Laboratories 3011 Malibu Canyon Road Malibu, California 90265	11. Contract or Grant No. NAS 3-16949
	13. Type of Report and Period Covered 10 Oct 1972 - 10 April 1974
12. Sponsoring Agency Name and Address National Aeronautics and Space Administration Lewis Research Center 21000 Brookpark Road Cleveland, Ohio 44135	14. Sponsoring Agency Code

15. Supplementary Notes

Project Manager: David Byers, NASA-Lewis Research Center, Cleveland, Ohio

16. Abstract This program has been conducted with the goal of providing advanced technology to improve the performance characteristics of 30 cm thrusters. At the outset, the activities and objectives under this program were pursued independently of the Engineering Model Thruster development being performed concurrently under Contracts NAS 3-15523 and NAS 3-16528. Early in the program, a re-direction was put into effect whereby a cooperative effort was established between all of these programs and the internal programs at NASA Lewis Research Center to provide the necessary inputs to the engineering model thruster development. The responsibilities of this program were divided into three distinct, but related Tasks. Under Task I, the discharge chamber and component design modifications proposed for inclusion in the engineering model thruster were evaluated and engineering specifications were verified. Under Task II, thrust losses which result from the contributions of double charged ions and nonaxial ion trajectories to the ion beam current were measured. A number of techniques for reducing these thrust losses were investigated and documented. Task III provided for the specification and verification of power processor and control requirements of the engineering model thruster design verified under Task I.

As a result of this work, proven design modifications which provided improved efficiencies were incorporated into the engineering model thruster during a necessary structural re-design without introducing any additional delay in schedule or new risks. In addition, a considerable amount of data were generated on the relation of double ion production and beam divergence to thruster parameters, and a basis was laid for providing further performance gains. Overall thruster efficiency was increased from 68% to 71% at full power, including corrections for double ion and beam divergence thrust losses, and further modifications to provide 73% thruster efficiency have shown promise.

17. Key Words (Suggested by Author(s))	18. Distribution Statement
Electric Propulsion 30 cm Ion Thruster Double Ion Thrust Loss Automatic Controller Mercury Propellant	UNCLASSIFIED – Unlimited

19. Security Classif. (of this report)	20. Security Classif. (of this page)	21. No. of Pages	22. Price*
Unclassified	Unclassified	173	$3.00

* For sale by the National Technical Information Service, Springfield, Virginia 22151

FOREWORD

The work described herein was performed in the Hughes Research Laboratories Ion Physics Department of the Hughes Aircraft Company in Malibu, California. This department is managed by Mr. J.H. Molitor. The work was performed under Contract NAS 3-16949, monitored by Mr. David Byers of NASA Lewis Research Center. Major technical contributors to this effort were:

R.L. Poeschel	Project Manager, Discharge chamber optimization
R.P. Vahrenkamp	Discharge Chamber Optimization Thrust Loss Measurements
H.J. King	Thruster Component Development
D.E. Schnelker	Thermal Design
B.G. Herron and S.C. Hansen	Power Processor/Thruster Integration
J.W. Ward	Computerized Beam Probe Analysis

PRECEDING PAGE BLANK NOT FILMED

TABLE OF CONTENTS

LIST OF ILLUSTRATIONS

LIST OF TABLES

SUMMARY

The 2.5 kW Advanced Technology Ion Thruster program had as its goal the development of a thruster module with significantly improved performance characteristics. Specific goals for full power operation were reduction of discharge chamber losses to 170 eV/ion or less, improvement of propellant utilization to 95% or more, minimization of the divergence and doubly charged ion content of the extracted ion beam, and maintenance of stable control characteristics. An accelerated optimization program was pursued through a cooperative effort of the personnel of NASA Lewis Research Center (LeRC) and Hughes Research Laboratories (HRL), and a thruster module was developed which very nearly meets these goals. In order to make these performance gains available to the thruster under development in the Low Voltage Thruster Program (NAS 3-16528) with minimal impact on the conduct of that program, the activity under this program was restructured. As a result of this redirection, the activity under this program was conducted under three distinct tasks. Task I was directed toward advancing the development of the basic thruster design specified for the Low Voltage Thruster Program. Emphasis was placed on integration of all modifications necessary to achieve optimum thruster performance with the complete thruster/power conditioning system. This included documentation of thermal properties, control stability and thrust loss factors. Task II was concerned with identifying a means of reducing thrust degradation arising from doubly charged ions and beam divergence, and/or further improving thruster discharge chamber efficiency. The specific goal for this task was to achieve a corrected overall thruster efficiency of 73% or more. Task III was devoted to documentation of the control characteristics of the Task I thruster and to the development of the appropriate circuitry to provide stable thruster control.

Nearly all modifications proposed for inclusion in the engineering model (EM) thruster which could affect operational characteristics or thruster performance were thoroughly evaluated under this program prior to completion of the final EM thruster module. Initial evaluation of the first 700 series EM thruster provided operational and performance

characteristics in good agreement with those obtained with the laboratory prototype tested under tnis program. As a result of the confidence in the design gained in these and other tests, the first EM thruster built (SN701) was committed to endurance testing.

Extensive investigation of double-charged ion production was carried out under this program. Thrust losses from double ionization could not be reduced below 4% during the program, but several factors were identified which could produce further reduction, and perhaps realize the goal of 73% corrected overall efficiency. These factors related to accelerator grid transmission and discharge current oscillation.

Beam divergence thrust loss, which results from the dished grid electrode curvature, has been reduced to about 1% by appropriately adjusting the hole patterns of the screen and accelerator grid. Beam probe techniques for monitoring both beam angle and double ion content were perfected under this program.

An overall thruster efficiency of 71%, corrected for double ion and beam divergence thrust losses, was demonstrated with several discharge chamber designs (including the EM thruster) under this program. In addition, considerable information was generated on factors related to ion beam uniformity, magnetic baffle effects on stability, and dispersion in thruster operational characteristics. The goals of the program were satisfied, in so far as verification of the EM thruster design was concerned, and possible prospects for further advancement of thruster technology have been identified and reported.

I. INTRODUCTION

The 2-1/2 kW Advanced Technology Ion Thruster Program was one of three concurrent programs sponsored by NASA Lewis Research Center (LeRC) to develop a 30-cm diameter thruster module for prime propulsion application. These programs were initiated early in 1972 as the logical continuations of development on the promising prototype thruster produced under the Low Voltage 30-cm Ion Thruster Program (Contract NAS 3-14140, Final Report NASA CR-120919) which had just been completed. Initially, these three programs had well defined, independent goals and objectives. The first program, the Thruster Endurance Test Program (Contract NAS 3-15523), was commissioned with building and endurance testing a thruster of the design developed under the preceeding Low Voltage 30-cm Ion Thruster Program. A second follow-on Low Voltage 30-cm Ion Thruster Program (Contract NAS 3-16528) was assigned responsibility for improving overall thruster efficiency and improving the structural design of the prototype thruster to meet launch requirements, including structural qualification of the new design by vibration testing. The thruster which evolves from the activities of these two programs has been designated as the engineering model (EM) thruster. It is intended that this thruster design will be used in generating data and interface specifications representative of the "state of the art" for use in the design of ion propulsion subsystems. It was recognized at the outset of these two programs that the performance characteristics of the existing thruster design left margin for further improvements. To pursue this potentiality, the Advanced Technology Program was initiated to improve thruster discharge chamber efficiency and ion optical system perveance with the goal of producing an advanced "second generation" thruster design. Completely new concepts, as well as modifications of existing designs, were initially under consideration for development. It was not anticipated that advanced technology developed under this program and similar programs at NASA LeRC would be utilized in the EM thruster programs as originally conceived. Almost before the Advanced Technology Program got under

way, however, it became apparent that significant advances in technology were required by the EM programs to meet their goals. One of the principal factors contributing to this circumstance was a failure of the flat grid ion optical system's center support in preliminary structural testing. The inadequacy of this ion optical system design was further emphasized by erosion around the center support observed in early phases of endurance testing. Thus, it was necessary to accelerate development of the "dished grid" ion optical system for both structural and wearout life considerations. Incorporation of the dished grid ion optical system design also improved thruster discharge chamber efficiency and ion optical system perveance in addition to satisfying structural and lifetime requirements, thus preempting a portion of the work originally planned for the Advanced Technology Programs. When it was determined that a structural redesign was necessary under the Low Voltage Thruster program in order to provide an acceptable mechanical interface for the propulsion subsystem, the Advanced Technology Program was reviewed, and reoriented to coordinate with the requirements of the EM programs. The overall goal of the redirected program was to optimize, integrate and verify the performance of design modifications which represent the most recent advances in technology available from effort under this or similar programs at NASA LeRC for incorporation into a thruster of the EM configuration. A cooperative effort towards this goal under these programs resulted in the development of an EM thruster design, containing proven technology for correcting observed design deficiencies and improving overall thruster performance without incurring significant delays in either the structural testing or endurance test programs.

Before redirection, the 2-1/2 kW Advanced Technology Ion Thruster Program was formulated to produce an advanced thruster design under three distinct but related tasks. Under Task I, discharge chamber optimization was to be conducted to produce an advanced design. The performance goals called for reduction of discharge losses to less than 170 eV/ion at 96% or greater propellant utilization and 200 eV/ion at 90% propellant utilization at the full (2.5 kW) and half (1.25 kW) power

input levels, respectively. The objective of Task II was to develop an ion optical system capable of producing 2.5 A beam current with a net acceleration of 1000 V. The optimum ion optical system was then to be integrated with the optimum discharge chamber, and the power processor/thruster interactions and transfer functions were to be documented under Task III, resulting in a complete new thruster design specification. Thrust losses resulting from divergent beam trajectories and double charged beam ions were to be measured extensively for the first time under this program. Initial measurements of these losses disclosed greater thrust losses than anticipated, and this factor also contributed to the decision to coordinate the efforts of this program with EM thruster development. In redirecting the program, Task I retained its goals as stated but restricted the optimized discharge chamber design to one requiring minimal modification of the EM discharge chamber. In the conduct of the program, nearly equal emphasis was placed on satisfying this restriction as was placed on obtaining improved performance. Task II was completely changed, since nearly all the ion optical system requirements of the original program were satisfied by the dished grid ion optical design. In consideration of the magnitude of the thrust losses, the more significant thruster performance parameter has become the corrected overall efficiency. The efforts under Task II were directed towards obtaining an overall corrected thruster efficiency of 73% or greater at full power (2.5 kW) operation. This goal was pursued by investigating parameter variation and/or design modifications in an attempt to identify empirical relationships between double ion production and thruster parameters. A number of dished grid ion optical systems were evaluated to relate hole pattern design to divergence and double ion thrust losses. Performance of Task III was according to the original plan, and the only change here was in the thruster specified for the investigation. The EM thruster design which was verified and specified under Task I was used to conduct Task III.

Reporting of the work performed under the three tasks of this program has been organized by topic rather than by Task, or in chronological sequence. The major topics are discharge chamber investigation,

ion optical system evaluation, double ion thrust losses, power processor interactions, and advanced component technology. All significant experimental results have been included or discussed whether successful in improving performance or not. While reference is made to work performed under other programs for lending continuity and accuracy to this report, no attempt has been made to systematically identify every experiment where test results have been obtained using hardware or designs developed under either the Thruster Endurance Test Program (NAS 3-15523), the Low Voltage 30-cm Ion Thruster Program (NAS 3-16528) or supplied by NASA Lewis Research Center. Consequently, data reported here may also appear in reports or publications of these other activities.

II. DISCHARGE CHAMBER INVESTIGATION

The performance of the discharge chamber has in the past been measured in terms of discharge losses (eV/ion) required to achieve a given propellant utilization. As stated in the introduction, the objective of the discharge chamber investigation under this program was to reduce discharge chamber losses to less than 170 eV/ion while achieving a propellant utilization of 96% or more at full operating power, and 200 eV/ion for 90% utilization at half power. Discharge chamber performance approaching these levels had been obtained under a prior program using insulated, single grid ion optical systems; however, the same discharge chamber was capable of producing only 93% utilization at full power and 82% utilization at half power for 260 eV/ion discharge loss when operated with a two grid, center supported ion optical system. Dished grid ion optical systems had already been introduced by the start of this program and without modification to the discharge chamber, discharge losses had been reduced to 220 eV/ion with the achievement of 96% propellant utilization at full power and 87% utilization at half power. Discharge investigation under this program began by comparing several discharge chambers which make use of different electron confining magnetic field geometrics. Dished grid ion optical systems of the type which had produced improved performance were used for this evaluation. On the basis of this comparison and other program priorities, several geometries were selected for further optimization. Initially, thruster and discharge chamber performance was evaluated on the basis of metered electrical parameter values, and optimizing parameters for any given configuration was simply a matter of maximizing or minimizing the appropriate meter readings. With the first measurement of double-charged beam ions it became apparent that double ion production rates could be a predominant factor in determining thruster efficiency, and optimization became more laborious and dependent on reproducible results. For the most part, this section describes and compares the metered performance characteristics of discharge chamber design

modifications, and Sections III and IV have been devoted to the discussion of the effects of beam divergence and double ion production. Parameter variations described in this section were made with the goals of reducing discharge losses, increasing propellant utilization and improving the uniformity of the discharge chamber plasma as a means to this end. The initial portion of this discussion treats the experimental technique for evaluating and documenting thruster performance throughout the entire report.

A. Performance Evaluation Measurement Techniques

Discharge chamber and total thruster performance are based on meter measurements of electrical parameters and timed measurement of propellant flow from mercury reservoirs. The basic circuit diagram defining the symbols and measurement locations for the essential parameters is shown in Fig. 1. Ion beam potential is assumed to be that of the grounded beam collector. Throughout this report when quantities such as thrust or electrical efficiency are referred to it is to be understood that the values quoted are meter values. These values defined in terms of the parameters measured are shown in Fig. 1. For example, thrust is

$$T_{metered} = I_B V_B^{1/2} \left(\frac{2M}{e}\right)^{1/2} \qquad (1)$$

where I_B and V_B are the beam current and voltage as measured in Fig. 1. M is the mass of a mercury atom, and e is the electronic charge. Electrical efficiency is given by

$$\eta_e\Big|_{metered} = \frac{I_B V_B}{\text{Total Power Input}}, \qquad (2)$$

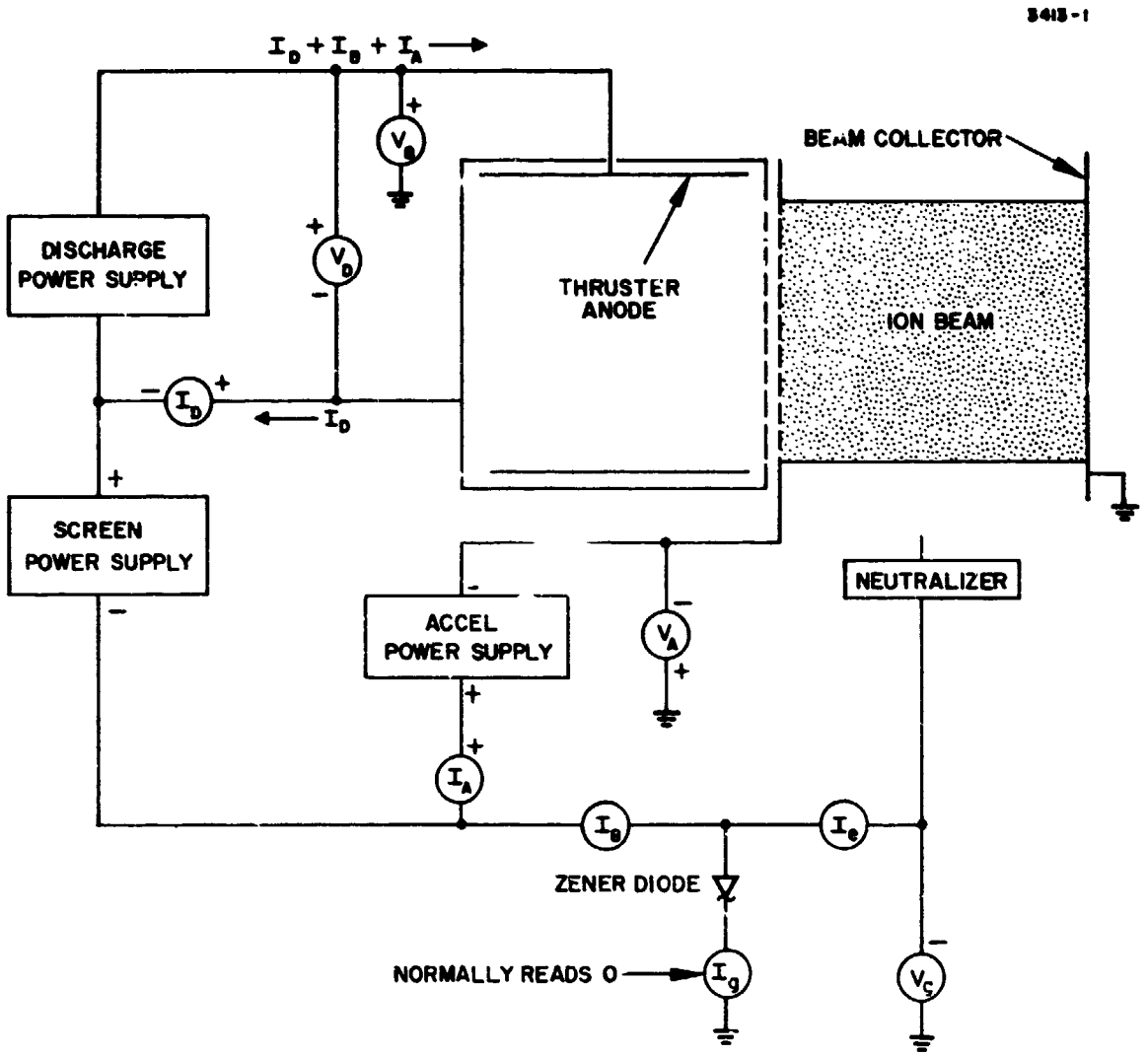

Fig. 1. Schematic diagram of principal thruster power supplies and meter locations for direct measurement of thruster performance parameters quoted in Table 1.

propellant utilization efficiency is given by

$$\eta_u \Big|_{\text{metered}} = \frac{I_B}{\text{Equivalent Neutral Flow Rate}}, \tag{3}$$

and total or overall thruster efficiency is given by

$$\eta_T \Big|_{\text{metered}} = \frac{T^2}{2\dot{m}P_{TOT}} = \eta_e \Big|_{\text{metered}} \cdot \eta_u \Big|_{\text{metered}}, \tag{4}$$

where T is given by equation (1), $\dot{m}$ is the rate of change in mass or propellant flow rate, and P_{TOT} is the total power input. The true or corrected values of these quantities are obtained by reducing the thrust produced on the basis of measured double charged ion content and non-axial components of beam trajectories. Correction or thrust factors have been defined as follows. To account for double charged ion content in the beam the thrust must be reduced by a factor defined as α where

$$T_{\text{actual}} = \alpha T_{\text{metered}},$$

and the beam current must be reduced by a factor β in using equation (3) so that

$$\eta_u \Big|_{\text{actual}} = \beta \eta_u \Big|_{\text{metered}}.$$

To correct thrust for nonaxial beam trajectories, the factor F_t is defined as

$$T_{\text{actual}} = F_t T_{\text{metered}}.$$

Hence for total correction of the total or overall efficiency the relationship is

$$\eta_{T_{\text{actual}}} = \frac{\alpha^2 F_t^2 T^2_{\text{metered}}}{2\dot{m} P_{TOT}} = \alpha^2 F_t^2 \eta_{T_{\text{metered}}}.$$

Measurement of these correction factors is discussed in detail in Appendix A. Quantities are referred to as "corrected" when these factors have been applied or the correction factors may simply be included with other parameters for comparison. Representative values of these factors for optimized discharge chambers and ion optical systems are $\alpha = 0.96 \pm 0.01$, $F_t = 0.985 \pm 0.01$ and $\beta = 0.93 \pm 0.01$ for thruster operation at full power (2 A beam current).

Two methods of monitoring mercury flow from propellant reservoirs have been used during this program. One method uses a standard laboratory glassware type calibrated pipette as reservoir for each vaporizer and reservoir level is read at regular intervals, usually ten minutes, for a period of 1 to 2 hours. Data are plotted and a best fit straight line is fitted graphically to the points. Propellant flow is computed on the basis of 1.81 equivalent amperes per milliliter of mercury consumed per hour. A second method makes use of load cells as weighing devices holding the mercury reservoir for each vaporizer. Readout is obtained in digital form from the load cell electronics and can be calibrated directly (within a constant scale factor) using standard weights. Conversion to equivalent amperes is made on the basis of 0.1333 A per gram of mercury consumed per hour. These two methods of measuring mercury flow rate have been compared and found to agree within 1%.

In addition to these measurements for determining thruster performance, a significant amount of effort has been applied to documenting thruster dimensions, magnetic field and operating conditions for each discharge chamber configuration evaluated. This is an important aspect of developmenta. testing in that ultimately design specifications will be necessary to convert the optimum configuration into more refined hardware. While it is impossible to assess, a priori, the impact of seemingly minor dimensional or configurational changes required to improve structure or reduce weight in a fully engineered thruster design, a complete record of preliminary experimental configurations facilitates the identification of possible differences responsible for changes in performance which may occur. To this end, numerous

measurements of critical dimensions were performed and recorded, geometry modifications were performed in a manner such that critical component parts or subassemblies were preserved for re-evaluation, and notes were entered in test logs relating to operational procedures and characteristics.

Magnetic field shape and strength was documented using both powdered iron field maps and field strength measurements. Field strength measurements were performed using a Hall effect Gaussmeter which has probes with axial or transverse sensing elements to determine the radial and axial field components. Measurements were made at selected locations within the discharge chamber as laid out on a measurement grid which is installed in the discharge chamber. The measurement and representative measured field values are shown in Table 1. Neither the registration of the measurement grid nor the positioning of the gaussmeter probe is a precision operation, and the accuracy of measured values is considered to be no better than ±3%. Documenting and reproducing magnetic field geometries using permanent magnets has been found to be one of the weaker points in discharge chamber specification under this program. A program to find a means of documenting permanent magnets absolutely and reproducibly has been instituted under a Hughes Research Laboratories internal program as a result of this difficulty.

In some selected experiments, measurements of special parameters were performed such as discharge chamber component temperatures or discharge current waveforms. Temperature measurements were made using thermocouples appropriate to the temperature range and calibrated, direct reading thermocouple meters. Spot checks were made by comparing temperatures measured in this manner with temperatures measured using bridge techniques. With the thermocouple resistance properly compensated, the measurements agree to within ±2%, and consequently all measurement locations which require a thermocouple to operate at discharge chamber potential were made using compensated direct readout metered systems. Discharge current waveforms were monitored using either ac or dc clamp-on probes (Tektronix

TABLE 1

Typical Magnetic Field Distribution Documentation

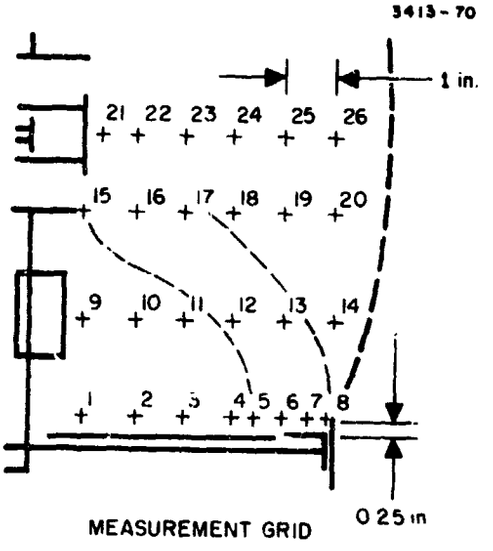

Measurement Grid Location	Axial Magnetic Field Values, G	Radial Magnetic Field Values, G
1	- 4.4	12.0
2	1.8	9.5
3	5.3	7.0
4	8.1	6.0
5	10.7	7.5
6	14.8	17.5
7	3.1	18.0
8	- 9.2	7.0
9	12.5	31.0
10	13.0	18.6
11	11.6	12.5
12	10.0	9.0
13	6.8	7.0
14	3.6	5.5
15	112.0	29.5
16	42.0	15.0
17	26.0	8.9
18	16.6	5.3
19	10.5	3.5
20	6.7	2.5
21	60.0	
22	45.0	
23	29.0	
24	19.0	
25	12.0	
26	8.0	

T1342

type P6042, for example) and oscilloscopes. In almost all cases, it was necessary to divide the current and measure only a fraction of the discharge current to prevent saturation or nonlinear response of the instrumentation.

B. Initial Comparison of Magnetic Geometries

The electron bombardment ion thruster discharge chamber utilizes a magnetic field to confine the energetic electrons extracted from the cathode plasma in order to maximize the probability that these electrons will ionize one or more neutral atoms. The magnetic field values necessary to achieve electron confinement are not strong enough to modify ion trajectories through magnetic forces, but by containing the electron component of the discharge plasma, the magnetic field can strongly influence the potential distribution. Because of the relatively small ion thermal energy, small potential gradients can greatly influence ion trajectories. At the outset of this investigation three concepts for electron confinement and resultant control of ion drift were under consideration. Figures 2, 3, and 4 show these geometries. The first magnetic geometry shown in Fig. 2 has been termed a divergent field geometry in that cathode or primary electrons are contained in a magnetic bottle defined by the magnetic lines of force which "diverge" from cathode to screen pole pieces. Langmuir probe measurements have shown that when operated with an efficient ion optical system, the plasma potential distribution produced has gradients which tend to accelerate ions towards the central area of the ion extraction screen.[1,2] This is a desirable effect and good electrical and propellant efficiency has been established with this configuration in previous programs. The magnetic geometry shown in Fig. 3 had evolved as a combination of the radial magnetic field geometry with variable magnetic baffle controlled electron injection. The goal of this configuration was to render the magnetic lines of force more radial by extending the cathode pole in order to increase ion drift towards the extraction screen, but without the tendency to focus these trajectories on axis. On the basis of prior data using a

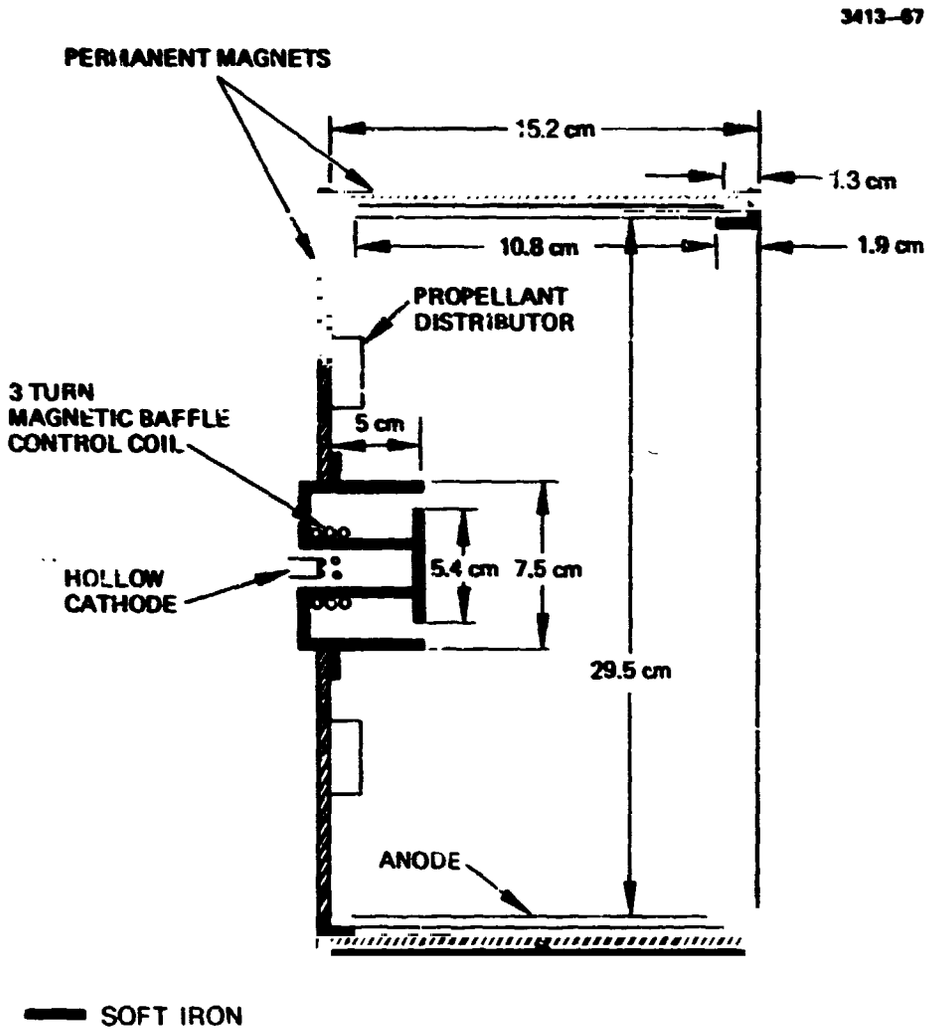

Fig. 2. Schematic of 30 cm divergent magnetic geometry thruster developed under NASA Contract NAS 3-14140.

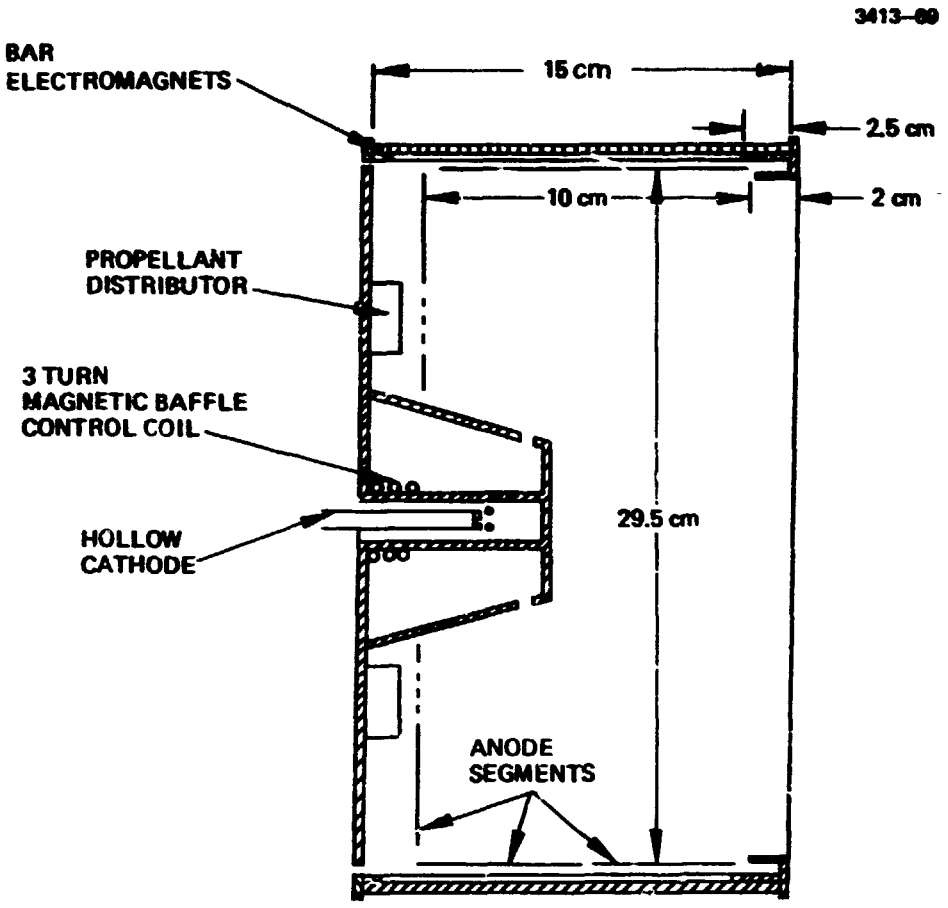

Fig. 3. Schematic of 30 cm radial hybrid magnetic geometry thruster developed under Hughes IR&D program.

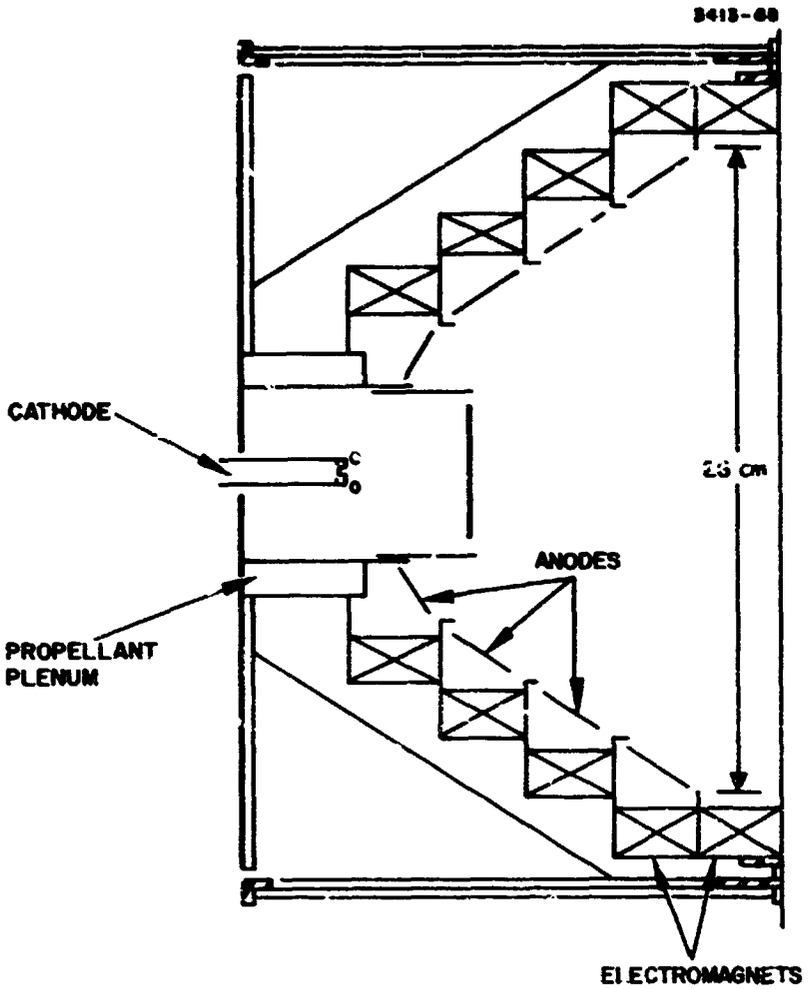

Fig. 4. Schematic of 30 cm boundary of cusp magnetic geometry thruster developed under Hughes IR&D program.

flat, center supported grid ion optical system design with this discharge chamber, it was thought that a highly uniform ion beam current density could be achieved. Both the diverging and the radial hybrid geometries make use of injection of the cathode electrons into the confining field to distribute these electrons throughout the discharge chamber. An alternative approach is represented by the cusped field magnetic geometry shown in Fig. 4. In this configuration, most of the discharge chamber volume is magnetic field free, the electrons being confined by relatively strong fields only at the boundaries by the magnetic cusps. It is thought that because most of the boundary area is at anode potential, ions will be reflected by the boundary sheaths.[3] Whether or not this is the case, depends on plasma potential relative to the anode and ion containment in the cusp geometry, was neither confirmed nor disproved by the work under this program. Table 2 compares representative performance data for these configurations obtained after some preliminary tune-up experiments. Figure 5 compares the ion beam current distribution profiles for these thruster geometries. On the basis of the time required for preliminary tune-up and the relatively mediocre level of performance obtained, the cusped magnetic field geometry was dropped from further consideration under this program. It should be noted, however, that this thruster configuration has not been fully optimized under this program because it possesses considerably more variables than the other configurations. Remaining optimization continued with the diverging and radial hybrid configurations.

C. Radial-Hybrid Magnetic Field Configuration

The radial hybrid magnetic geometry thruster configuration, shown in Fig. 3, was developed and optimized prior to the beginning of this program for operation with the flat grid, center supported ion optical system design. As shown in Table 2, the discharge chamber performance for this configuration was somewhat higher in propellant utilization and lower in discharge losses than the initial divergent field configuration tested. The uniformity of the extracted ion beam current

TABLE 2

Comparison of Performance Data for Divergent, Radial Hybrid and Cusp Magnetic Geometry Discharge Chambers

Fig. No.	Discharge Chamber Configuration	Grid System, SN	Beam Voltage, V	Beam Current, A	Discharge Voltage, V	Discharge Loss, eV/ion	Discharge Mass Utilization, %	Cathode Propellant Flow, mA
2	Divergent Magnetic Geometry	609	1100	2.0	38	220	95.6	161
2	Divergent Magnetic Geometry	609	1100	1.0	38	220	87.4	148
3	Radial Hybrid Magnetic Geometry	609	1100	2.0	38	190	95.8	116
3	Radial Hybrid Magnetic Geometry	609	1100	1.0	38	190	80.5	109
4	Cusped Magnetic Geometry	601	1100	1.5	40	280	80	67

T1334

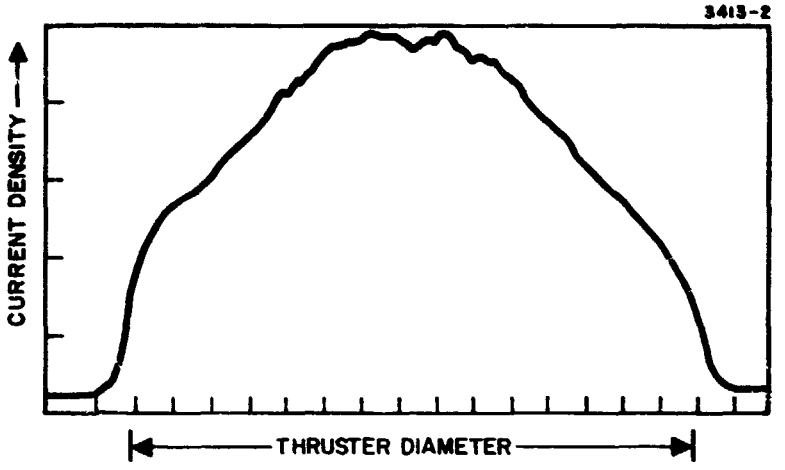

(a) DIVERGENT MAGNETIC GEOMETRY

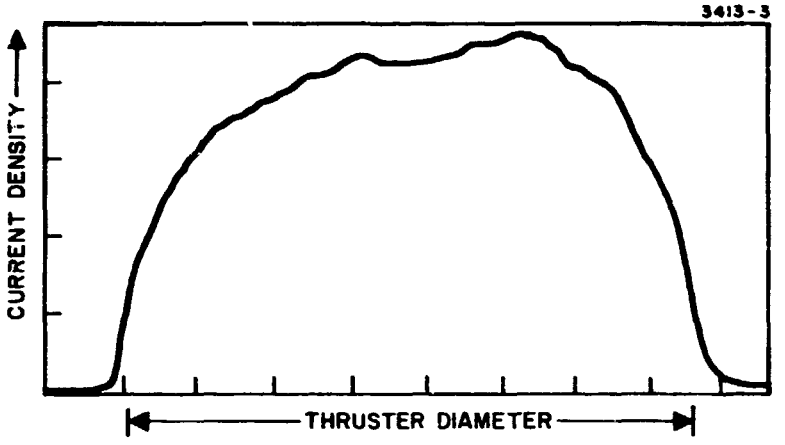

(b) RADIAL-HYBRID MAGNETIC GEOMETRY

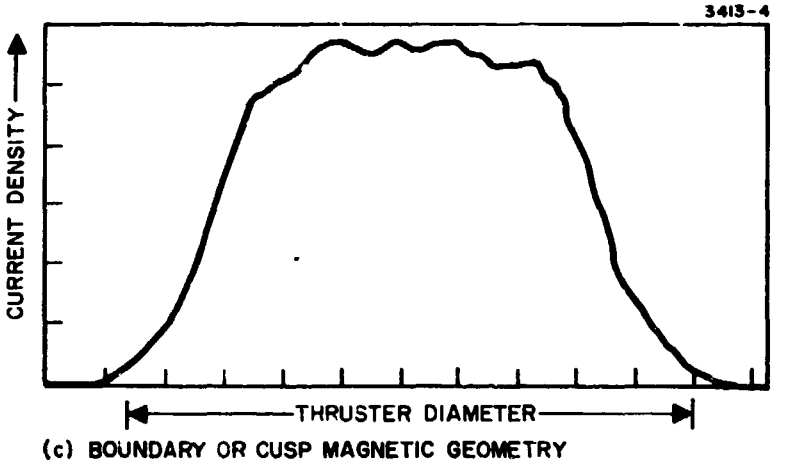

(c) BOUNDARY OR CUSP MAGNETIC GEOMETRY

Fig. 5. Comparison of extracted ion beam current density distribution across beam diameter.

was also better and the configuration was, therefore, thought to be better adapted to higher beam current operation. An accelerated program was pursued to develop this configuration to a point so that the technology could be made available, if required, to the engineering model thruster programs. Figure 6 illustrates modifications made to the discharge chamber to achieve a level of performance approaching the program goals. The configuration shown in Fig. 6(b) represents an attempt to deflect the propellant input to larger discharge chamber radius and, thereby, further improve discharge plasma and extracted ion beam uniformity. Discharge operation and beam uniformity were totally uninfluenced by this modification. In contrast to operation of this thruster configuration with a flat grid ion optical system, the anodes at the upstream thruster boundary were relatively ineffective in modifying discharge chamber operation at the optimum magnetic field strengths required for operation with dished grid ion optical systems. These anodes were consequently removed, and experiments were performed to evaluate variations in the length of the screen pole piece. Optimum performance was obtained with the length shown in Fig. 6(c). This discharge chamber was then operated with several grid designs. A table listing all the dimensions and characteristics of the grid sets evaluated during this program is included in Table 13 of Section III. Performance data are supplied in Table 3 for comparison of the thruster configurations of interest, operation with several grid sets and a short parameter mapping for the best grid systems available. All of the grid sets listed have the same basic hole pattern. The performance variation observed was attributed to variation in grid to accel spacing for grid systems 609 and 638, and to the difference in dish depth for grid systems 636 and 638. The dish depth is 1 cm for grid system 636 and 2 cm for grid system 638. Variations in magnetic field strength using the radial, axial, or magnetic baffle windings were unsuccessful in improving discharge chamber performance over the level shown when the shallower dished grid system was used. This type of performance degradation with decreased grid dish depth has also been observed in

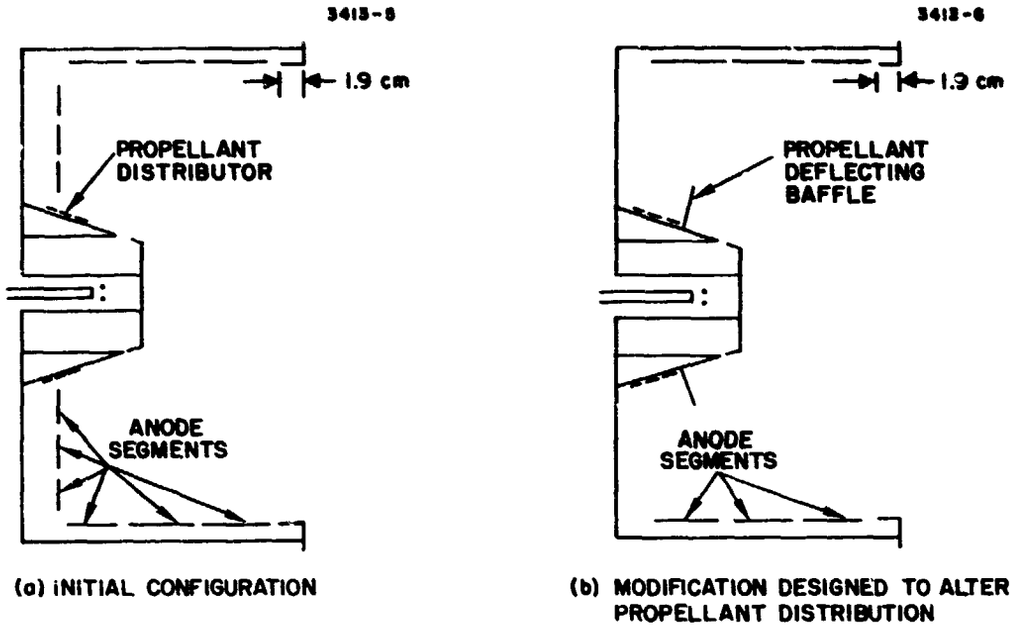

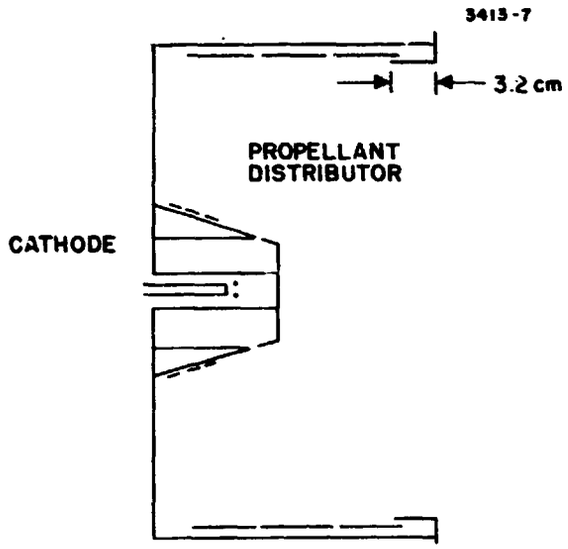

Fig. 6. Discharge chamber configurations representing modifications of the radial hybrid magnetic geometry. All configurations were operated with electromagnets and variable magnetic baffle.

TABLE 3

Comparison of Performance Characteristics for the Radial Hybrid Thruster Configuration for Modification as Noted

Fig. No.	Thruster Configuration	Grid System, SN	Beam Voltage, V	Beam Current, A	Discharge Voltage, V	Discharge Loss, eV/ion	Discharge Mass Utilization, %	Cathode Propellant Flow, mA
6	1.9-cm Screen Pole	609	1100	2.0	38	190	95.8	116
6(c)	3.2-cm Screen Pole	609	1100	2.0	38	190	97.4	127
6(c)	Ion Optical System Changes	636	1100	2.0	38	190	89.5	71
		636	1100	2.0	38	201	94.0	73
		638	1100	2.0	38	190	96.6	82
6(c)	Operational Parameter Variation	638	1100	2.0	37	190	92.3	91
		638	1150	1.45	38	190	92.8	78
		638	1150	1.45	37	190	87.0	83
		638	1300	0.85	38	190	79.0	98

T1335

operation with the diverging magnetic geometry discharge chamber. The discharge chamber performance obtained with grid system 638 was considered good enough to warrant some additional performance mapping and double-charged ion documentation before proceeding with any further modifications. The latter entries in Table 3 compare operation at different discharge voltage and beam current, and a representative example of the beam current density distribution is shown in Fig. 7.

During the measurement of double-charged ion content for determining thrust correction factors, an unexpected discovery was made. While the mass spectrometer recordings showed distinct, separated peaks for each ion species for thruster operation at 2 A beam current, the output recordings deteriorated at beam currents less than about 1.3 A, and the separation in the peaks completely disappeared below 1 A beam current. Figure 8 compares spectrometer recordings for 2 A and 0.85 A beam current. The cause of this condition was eventually traced to a modulation of the discharge current at a somewhat random rate, but with a repetition frequency in the 500 to 1000 Hz range. Onset of this modulation occurred at about 1.6 A beam current and increased in amplitude so that at 1 A beam current, discharge current was cut off instantaneously during each cycle. This also modulated both the beam current and voltage and explained the deterioration in both the spectrometer recording and the propellant utilization shown for 0.85 A beam current in Table 3. Correction factors and other performance parameters for this discharge chamber are shown in Table 4. Because of the relatively good performance of this discharge chamber geometry, a concerted effort was begun to eliminate this undesirable modulation of the discharge current. After a number of unsuccessful attempts were made to vary magnetic field strength and the baffle geometry, all observations led to the conclusion that the relatively strong magnetic field isolating the cathode plasma and main discharge plasma was responsible for the discharge modulation. To test this hypothesis, the thruster geometry shown in Fig. 9, which has axial instead of radial electron injection, was tested. As a result the current modulation disappeared, propellant utilization decreased by about 5%, and the uniformity of the beam profiled was degraded as seen in Fig. 10. In an attempt to regain

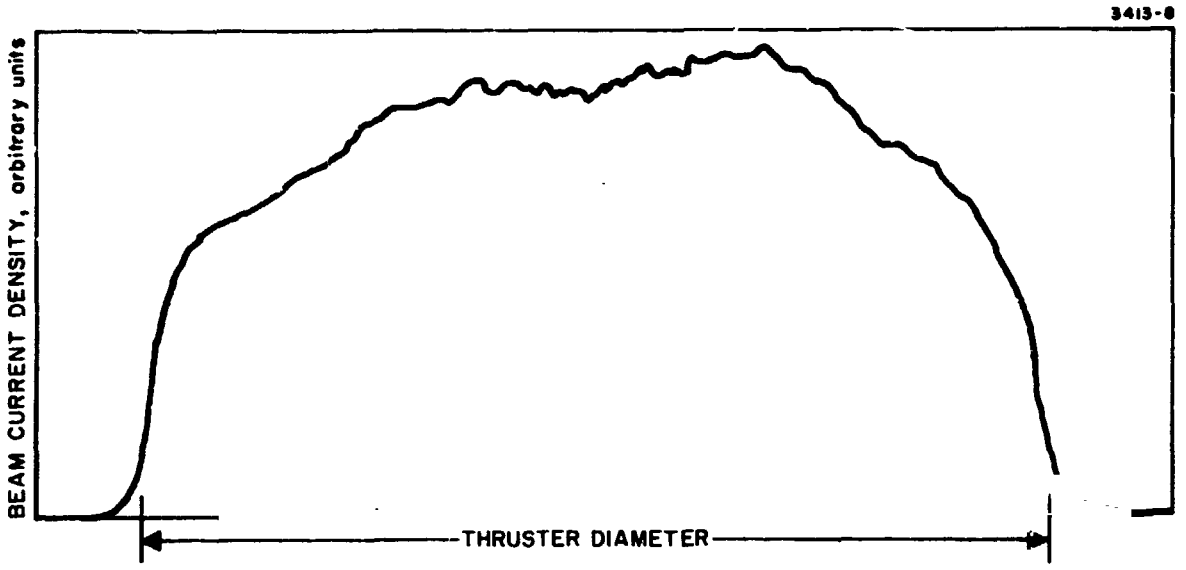

Fig. 7. Profile of radial distribution of ion beam current density measured 1 cm downstream of the accel electrode with the HRL experimental thruster operated with ion optical system SN 638 at 2 A beam current.

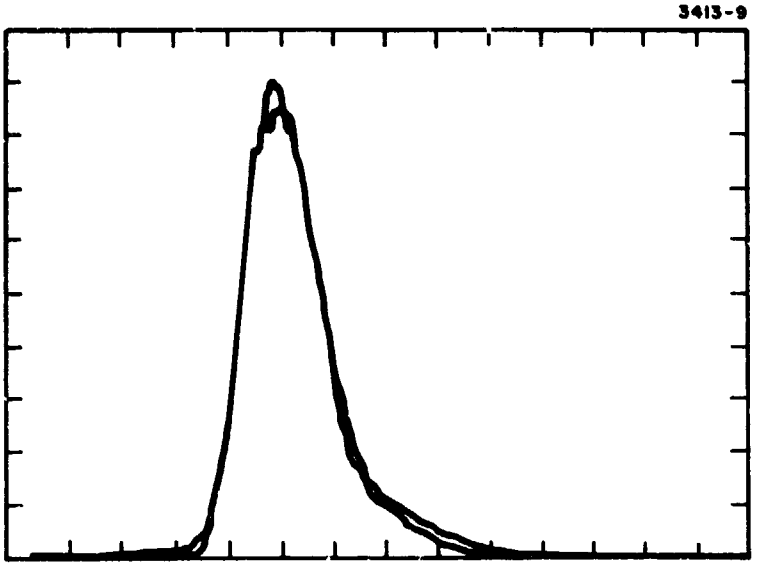

(a) RECORDING AT 0.85 A BEAM CURRENT

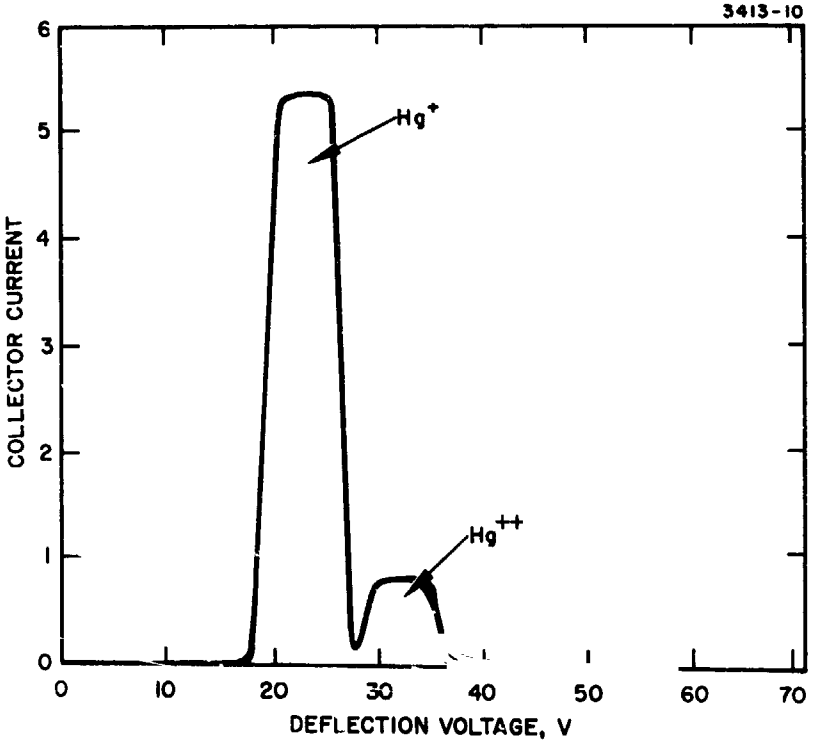

(b) RECORDING AT 2 A BEAM CURRENT

Fig. 8. Mass spectrometer recordings at 0.85 A and 2 A beam currents.

TABLE 4

Thruster Parameters for Operation of the HRL Experimental Thruster With Ion Optical System SN 638 at Full Power, 3/4 Power, and 1/2 Power Input

	Full Power	3/4 Power	1/2 Power
Total Power, W	2640	2000	1313
Beam Power, W	2200	1670	1100
Discharge Power, W	380	276	162
Heater Power, W	16	16	16
Keeper Power, W	14	16	22
Neutralizer Coupling, W	30	22	13
Electrical Efficiency, %	83.3	83.5	83.7
Propellant Efficiency, %	94.5	90.8	76.2
Overall Efficiency, %	78.8	75.8	63.8
Effective I_{sp}, sec	3100	3050	2750
Discharge Voltage, V	38	38	38
Discharge Loss, eV/ion	190	190	190
Discharge Utilization, %	96.5	92.8	79
Neutralizer Propellant Flow, mA	43	37	38
Coupling Voltage, V	14.7	14.3	14.3
Neutralizer Keeper Voltage, V	13.0	13.7	15.8
Neutralizer Keeper Current, A	1.0	1.2	1.3
Beam Voltage, V	1100	1150	1300
Beam Current, A	2.0	1.45	0.85
Accel Voltage, V	500	500	500
Accel Current, mA	4.8	3.5	2.3
Thrust Correction Factor, α	0.963	0.972	
Propellant Correction Factor, β	0.937	0.952	
Thrust Correction Factor, F_t	0.98	0.98	
Corrected Overall Efficiency	70.2	68.7	
Corrected Propellant Efficiency	88.5	86.4	
Corrected Thrust, mlb	30	23	
Corrected Power/Thrust, mlb	88	87	

T1343

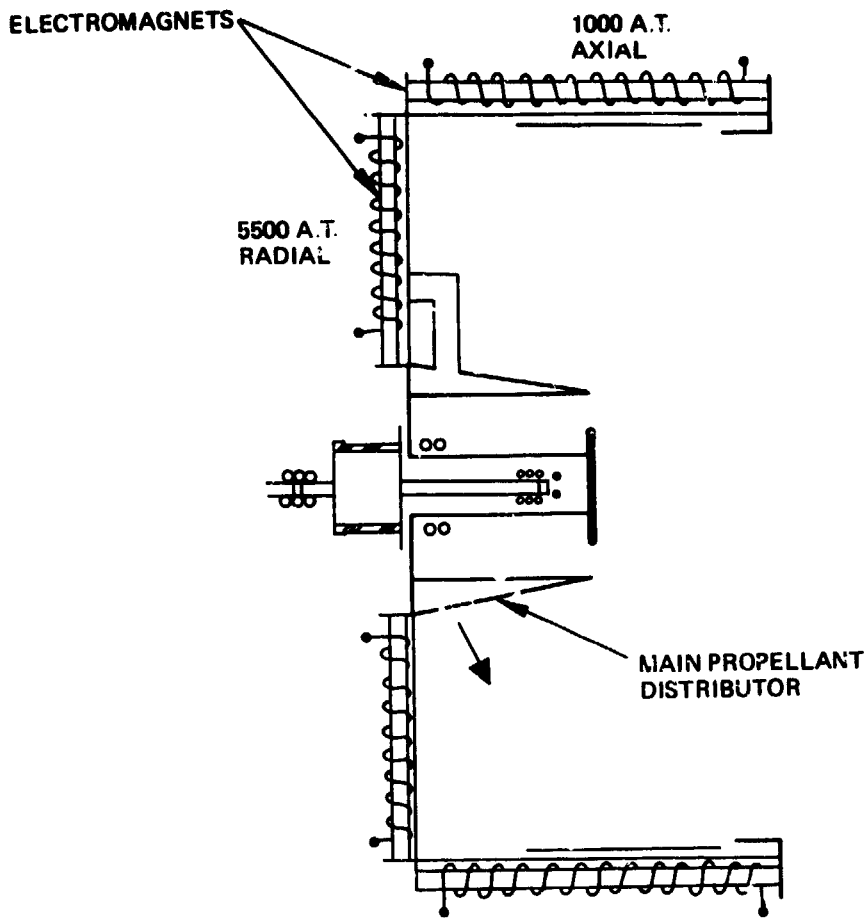

Fig. 9. Radial hybrid magnetic geometry discharg. chamber with axial electron injection.

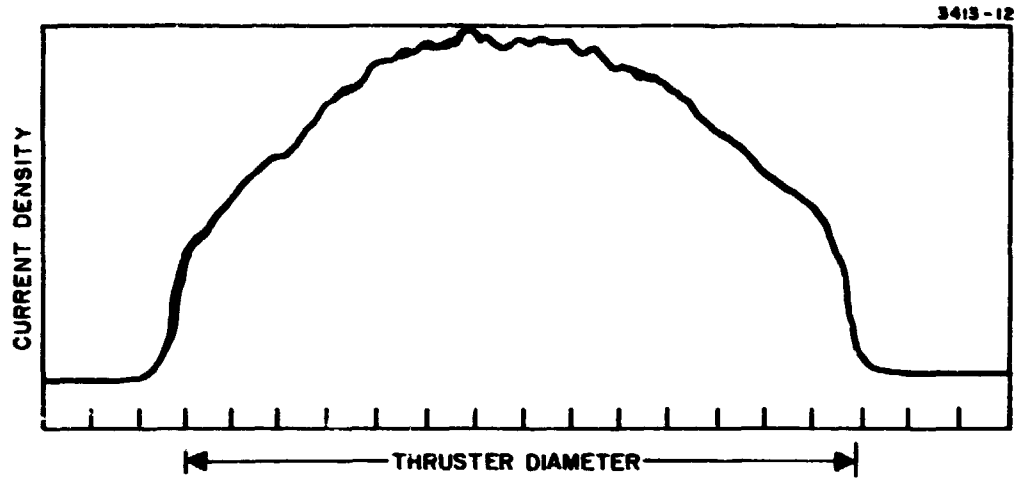

(a.) AXIAL ELECTRON INJECTION

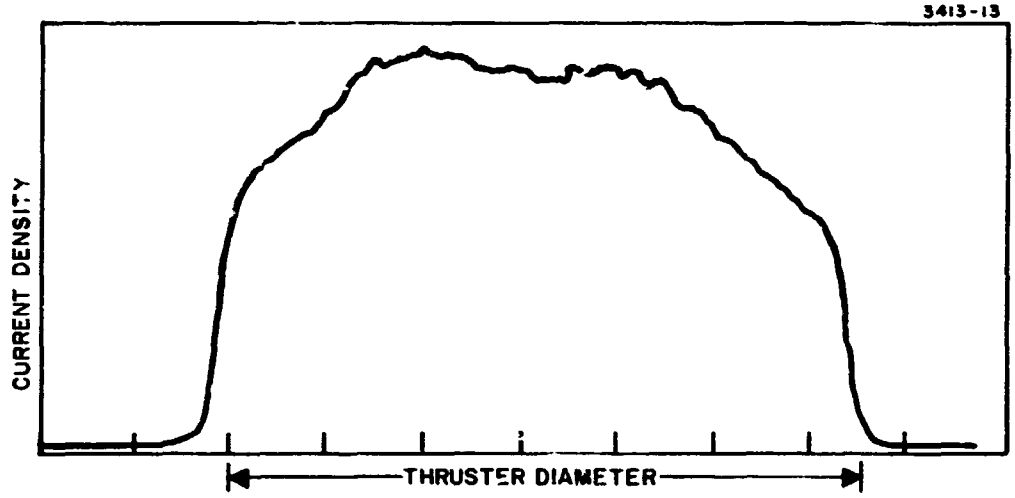

(b.) RADIAL ELECTRON INJECTION

Fig. 10. Comparison of beam current density distributions for discharge chamber operated with axial and radial electron injection (vertical scale arbitrary).

the desirable aspects of radial electron injection, modifications were explored to reduce the field in the gap through which electrons must pass from the cathode plasma into the main discharge chamber. Figure 11 shows a modified radial electron injection geometry which was found to be stable against the low frequency current modulation first observed. In this geometry the electrons are not injected into the magnetic field in the main discharge chamber in a manner so that good confinement is achieved and, therefore, the propellant utilization is found to be reduced even at high discharge loss values. Moreover, an excessive amount of iron was required to reduce the magnetic field around the injection gap, and it was considered improbable that a practical correction (in terms of weight, complexity, etc.) would be found for the radial injection instability. Consequently, the radial hybrid geometry was abandoned and discharge chamber optimization efforts were concentrated on the more conventional divergent magnetic geometry.

D. Divergent Magnetic Field Configurations

The divergent magnetic field discharge chamber shown in Fig. 2 is the configuration originally scaled from the 15 cm SERT II geometry and further optimized under the Low Voltage 30 cm Ion Thruster Program (NAS 3-14140). The design of the thruster developed under that program became known as the 400-series thruster. At the beginning of this program, the 400-series thruster discharge chamber design had undergone few changes. Performance gains were realized primarily as a result of improvements in the ion optical system. When it was decided that modifications to provide maximum discharge chamber efficiency should be factored into the engineering model thruster programs, the NASA Lewis Research Center programs assumed the responsibility for optimizing the divergent field thruster configuration, while this program concentrated on the radial hybrid geometry. It soon became apparent that the radial hybrid geometry was unacceptable because of extreme discharge current modulation, and the development of the divergent geometry was resumed under this program. The primary goal was to confirm the promising results obtained by NASA and to translate these results into firm design specifications as rapidly as possible.

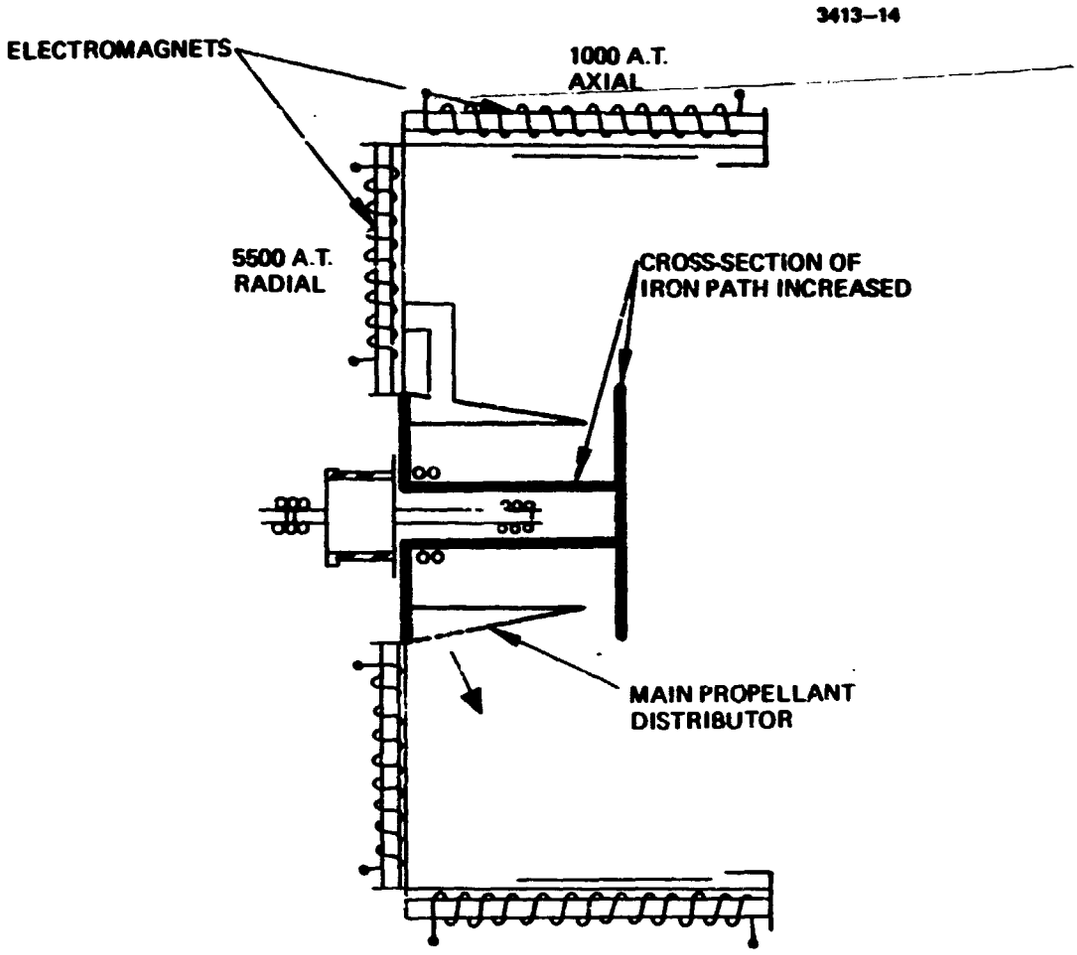

Fig. 11. Radial hybrid geometry with "stable" radial electron injection.

To confirm the performance gains obtained at NASA Lewis Research Center, a 400-series thruster was modified according to the specifications shown in Fig. 12. Typical discharge chamber performance data obtained at NASA Lewis Research Center are compared with the initial operating point of the modified thruster at 2 A beam current in Fig. 13. After considerable scrutiny of thruster dimensions, magnetic field shape, measurement instrumentation and operating techniques, it was determined that the principle difference in the thrusters tested was in the ion optical system (see Table 13, system 638 versus NASA 281). An ion optical system of the design used in obtaining the NASA data of Fig. 10 was obtained and thruster performance was consequently improved at the 2 A beam current level as seen in Fig. 14. The operating point of 185 eV/ion discharge loss at 95% propellant utilization was considered adequate to satisfy the EM thruster program goals, and a second thruster was prepared to evaluate all proposed discharge chamber design modifications. The prototype of this discharge chamber configuration is shown in Fig. 15. This discharge chamber module incorporated the modified isolator designs and structural elements which were considered necessary to verify thermal and operational characteristics of the revised EM design prior to fabrication. Development efforts performed under this program on some of these components or subassemblies are described in a later section. Initial testing of this discharge chamber at the 2 A beam level again displayed a difference of approximately 5% in propellant utilization for the 185 eV/ion discharge loss operating point. Again, considerable effort was spent in checking all dimensional and operational parameters and instrumentation. Minor dimensional differences in the magnetic baffle, cathode pole piece geometry were discovered and several parameter variations for this subassembly were evaluated. These variations are shown schematically in Fig. 16 and the accompanying performance changes listed in Table 5. While the performance variation shown cannot be conclusively explained, recent magnetic field measurements inside the cathode pole tip region indicate that the fringe fields which exist in the vicinity of the cathode orifice are influenced by the geometry and dimensions of both the baffle

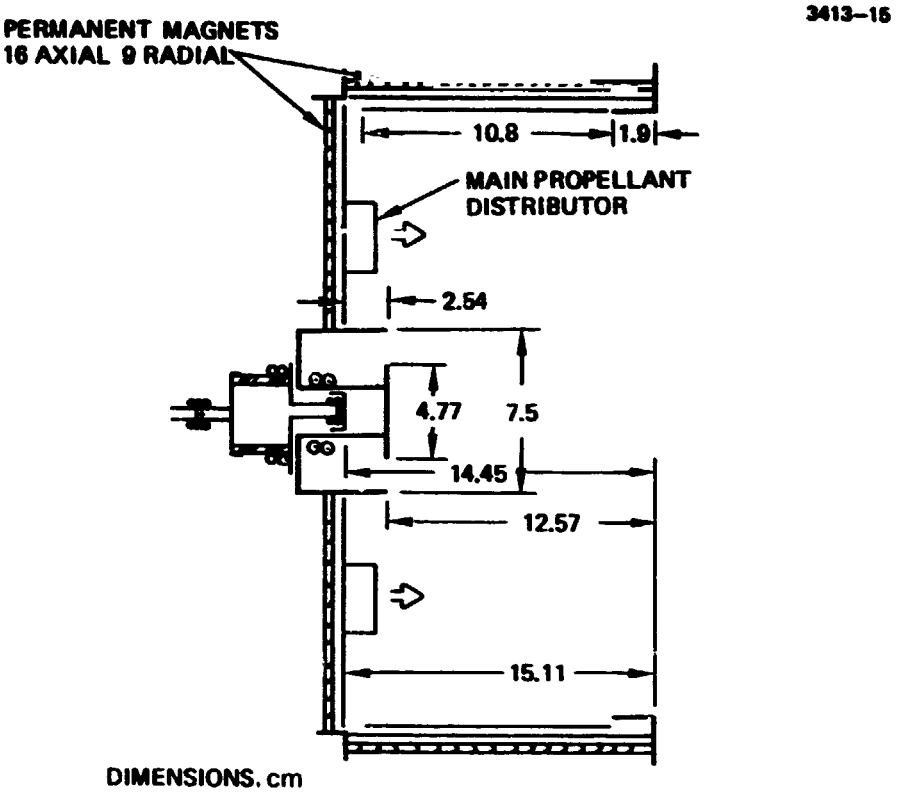

a) DISCHARGE CHAMBER CONFIGURATION (SN403-A)

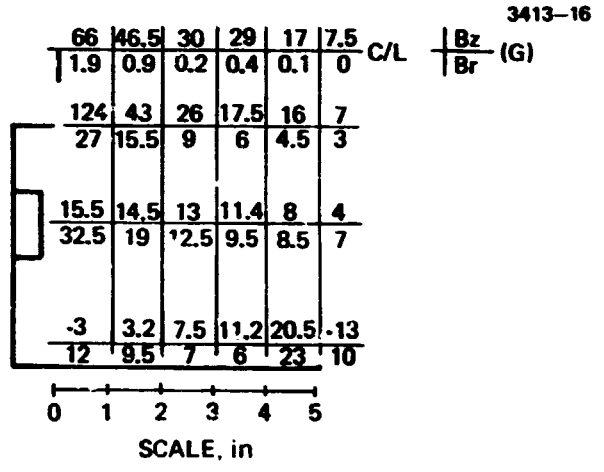

b) MAGNETIC FIELD STRENGTH DISTRIBUTION

Fig. 12. Initial modified divergent field thruster specifications.

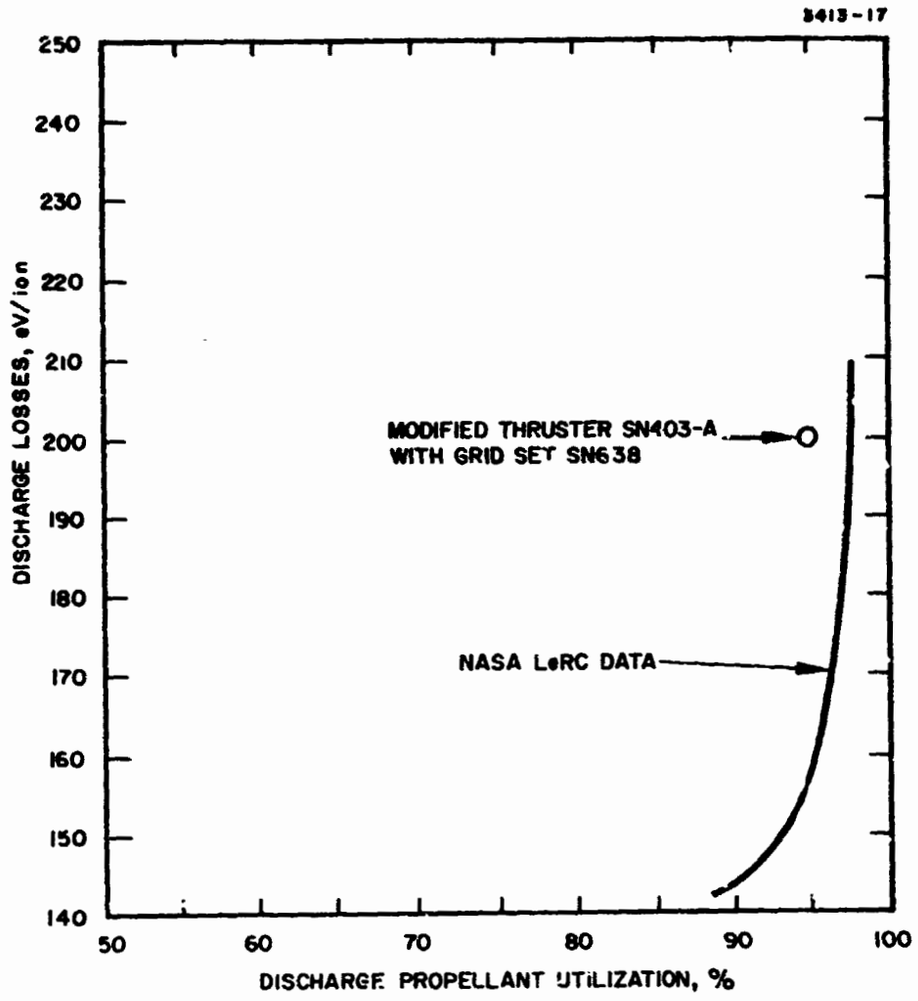

Fig. 13. Initial discharge chamber performance point for thruster geometry shown in Fig. 10, compared with performance achieved at NASA LeRC.

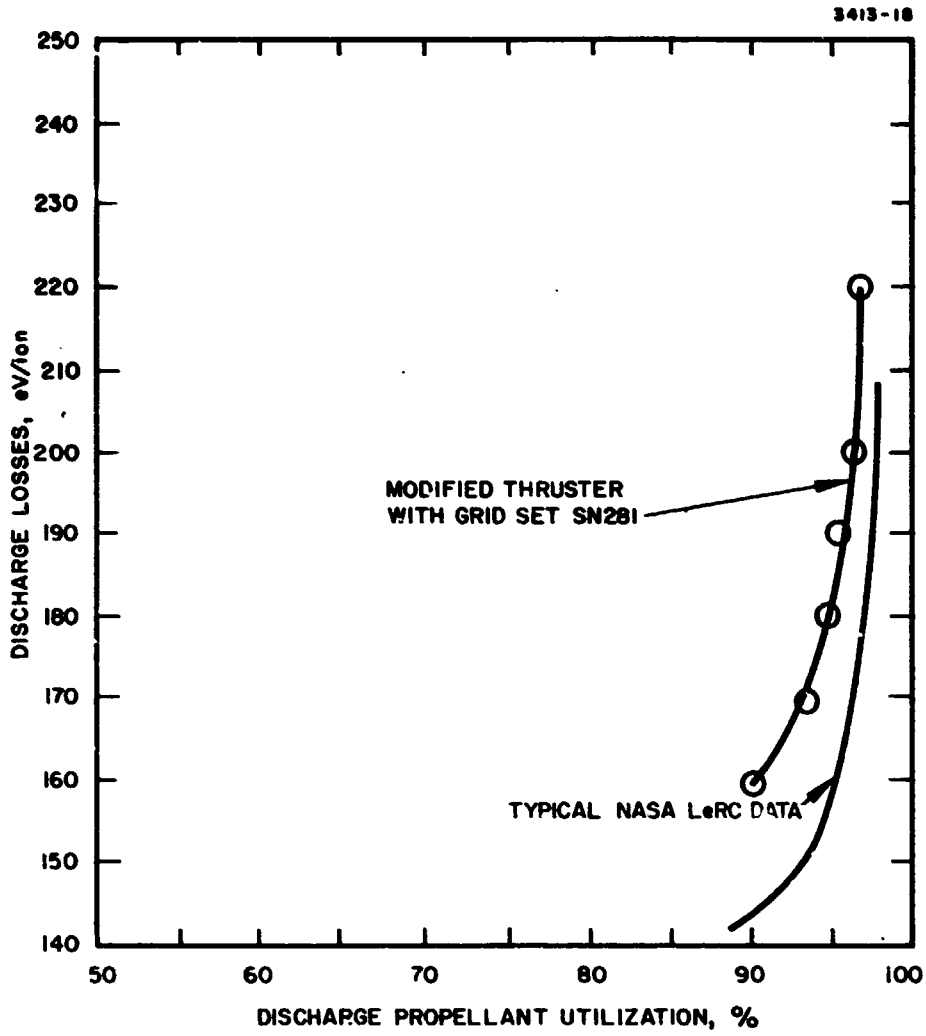

Fig. 14. Comparison of discharge chamber performance characteristic for thruster geometry shown in Fig. 10 with typical NASA LeRC performance using same design grid system.

3413-19

16 AXIAL AND 9 RADIAL PERMANENT MAGNETS

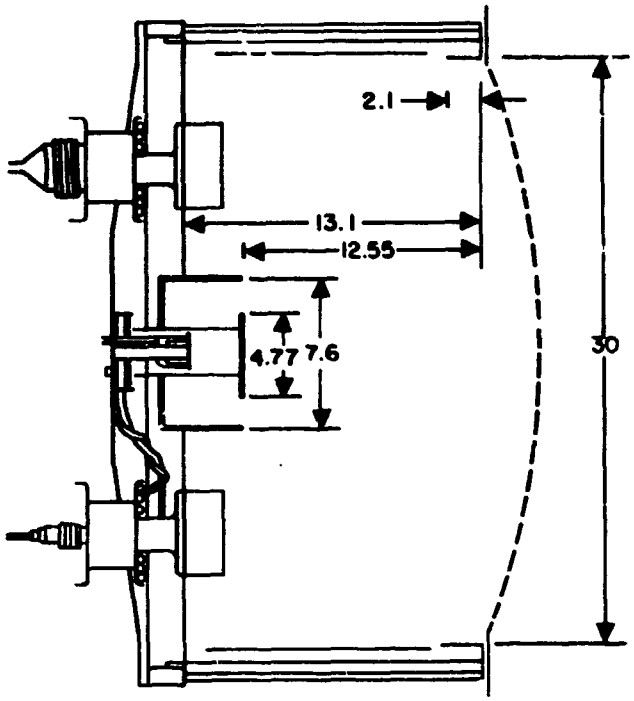

ALL DIMENSIONS ARE GIVEN IN cm

(a) DISCHARGE CHAMBER CONFIGURATION (SN 301-A)

3413-20

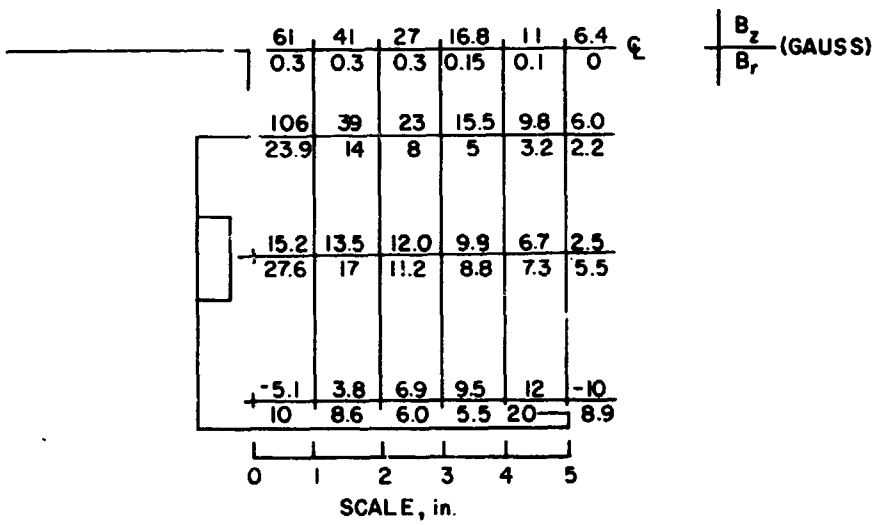

(b) MAGNETIC FIELD STRENGTH DISTRIBUTION

Fig. 15. Prototype EM thruster discharge chamber specifications.

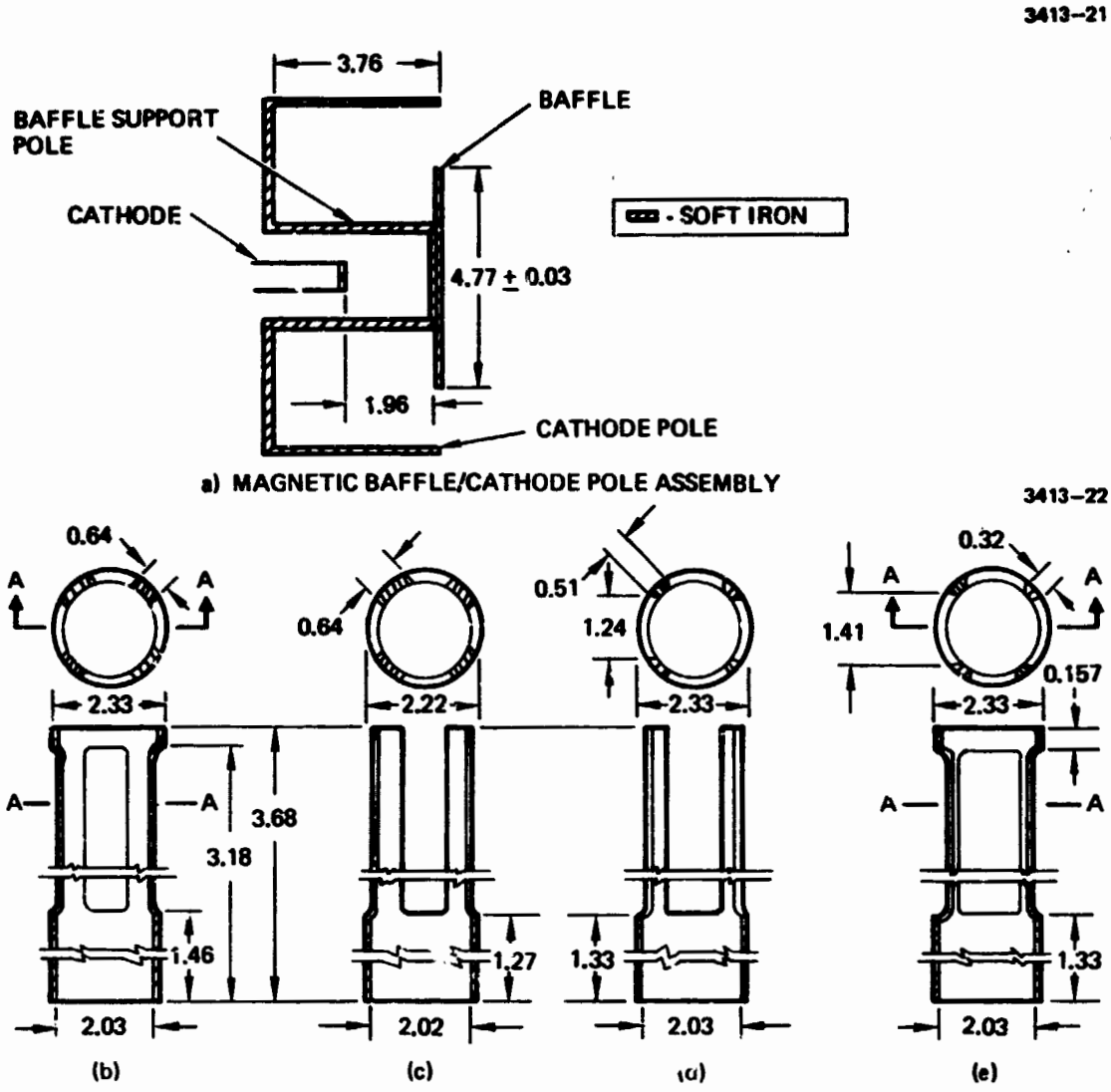

Fig. 16. Schematic drawing of magnetic baffle geometry and baffle support variations.

TABLE 5

Comparison of Discharge Chamber Performance for the Baffle Support Geometries Shown in Fig. 13

Baffle Support Pole (See Fig. 13)	Beam Current, A	Discharge Voltage V	Discharge Loss eV/ion	Discharge Mass Utilization, %[a]	Cathode Propellant Flow, mA	Magnetic Baffle, Amp-turns
(b)	2.0	37	185	83.4	79	50
(b)	2.0	37	185	90.4	78	52
(b)	2.0	37	185	91.3	72	52
(c)	2.0	37	185	88.3	94	60
(c)	2.0	37	185	89.0	76	57
(c)	2.0	37	185	91.7	79	60
(d)	2.0	37	185	97.7	107	90
(d)	2.0	37	185	94.5	136	91
(d)	2.0	37	185	95.5	101	71
(e)[a]	2.0	37	185	95.6	100	45

[a] Baffle diameter increased to 5.1 cm to reduce baffle coil ampere-turn requirement.

T1344

support and the baffle control coil. The desired performance level was restored by the configuration shown in Fig. 16(e) with the baffle diameter increased to 5.1 cm in order to reduce the magnetic baffle ampere turn requirement. The tradeoff between magnetic baffle diameter and baffle coil ampere-turns for the baffle support shown in Fig. 16(e) is illustrated in Table 6. It is not considered practical to employ a magnetic baffle geometry which requires more than 50 A turns of control coil excitation. This constraint is imposed by the engineering model power processor specification which limits maximum power supply current to 5 A, and by the space available in the cathode pole region which limits the control coil to approximately 10 turns. This thruster configuration was also operable in the "passive" magnetic baffle mode of operation (whereby the discharge current is used to excite the baffle coil).

The structural symmetry of the revised EM thruster design requires the permanent magnets to be sized so that 12 radial and 12 axial magnets produce the required magnetic field configuration. Table 7 compares magnetic field values for the magnet dimensions used originally and for the magnets required to achieve the required field distribution with 12 magnets. Performance of this discharge configuration was evaluated at several operating points for both active (control coil energized by a separate power supply) magnetic baffle and passive magnetic baffle operation. Performance data obtained with 12 magnets, a 5.1 cm diameter baffle, and the baffle support geometry shown in Fig. 16(e) is given in Table 8. With the specification of magnet dimensions for producing the required magnetic geometry, the development of this geometry was considered completed.

In the course of investigating double charged ion production, another variation of the divergent magnetic field configuration was evaluated which operated at essentially equivalent performance levels and is described here. The discharge chamber configuration and magnetic field distribution were essentially unchanged from the 400 series design, with the exception of the cathode position, cathode pole piece length, and baffle diameter as shown schematically in Fig. 17. The thruster was operated with several ion optical systems of the EM design to obtain performance data such as that shown in Table 9.

TABLE 6

Magnetic Baffle Characteristics for Variation in Baffle Diameter (Baffle Support Geometry Shown in Fig. 16(e))

Cathode Propellant Flow Rate, mA (Equivalent)	Baffle Diameter, cm	Baffle Control Coil, amp-turns	Discharge Propellant Utilization, %
101	4.77	71	95.5
100	5.1	45	95.6
145	5.4	19	92.8

All parameters obtained with

Discharge Voltage	37 V
Beam Current	2 A
Discharge Losses	185 eV/ion
EM Design Grid System	

T1338

TABLE 7

Comparison of Discharge Chamber Magnetic Field Values Obtained with Several Combinations of Axial and Radial Magnets

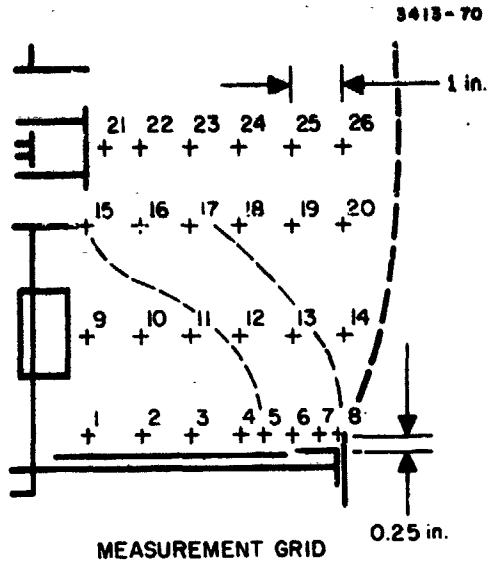

Thruster Magnets: Radial / Axial — Field Values	NASA LeRC 8 400 Series, 3 300 Series, 12 400 Series, 4 300 Series		SN 301-A 9 ea 0.36 cm x .99 cm, 16 ea 0.36 cm diam.		SN 301-A 12 ea 0.36 cm x .76 cm, 12 ea 0.36 cm diam.	
	Axial, g	Radial, g	Axial, g	Radial, g	Axial, g	Radial g
Position on Measurement Grid						
1	5.0	10.5	-5.2	10.5	-4.4	12.0
2	10.5	7.2	2.3	8.5	1.8	9.5
3	13.0	6.7	5.9	6.6	5.3	7.0
4	14.5	5.8	8.8	5.7	8.1	6.0
5	16.0	10.5	11.4	7.6	10.7	7.5
6	16.7	20.0	16.0	19.3	14.8	17.5
7	3.0	1.5	0.8	15.8	2.1	18.0
8	-9.8	14.5	-10.0	7.9	-9.2	7.0
9	17.0	21 0	12.0	28.0	12.5	31.0
10	17.7	15.0	12.0	17.2	13.0	18.6
11	16.0	10.7	11.0	11.3	11.6	12.5
12	13.0	8.8	9.2	8.9	10.0	9.0
13	9.0	8.0	6.4	7.7	6.8	7.0
14	4.0	6.0	2.8	5.6	3.6	5.5
15	125.0	31.0	95.0	25.5	112.0	29.5
16	42.0	13.5	37.6	14.0	42.0	15.0
17	25.0	7.5	24.0	8.1	26.0	8.9
18	17.0	4.5	15.5	59.0	16.6	5.3
19	11.5	3.2	10.0	4.0	10.5	3.5
20	7.0	2.3	6.0	2.8	6.7	2.5
21	60.0	2.0	53.5	0	60.0	-0.6
22	45.0	2.0	41.5	0	45.0	-0.7
23	28.0	1.0	27.0	0	29.0	-0.6
24	18.7	1.0	17.5	0	19.0	-0.6
25	12.5	0.5	10.5	0	12.0	-0.5
26	7.7	0.5	6.5	0	8.0	-0.4

T1345

TABLE 8

Discharge Chamber Performance of Thruster SN 301-A in Final Configuration for Verification of EM Thruster Design

Beam Voltage, V	Beam Current, A	Discharge Voltage, V	Discharge Loss eV/ION	Discharge Mass Utilization, %	Cathode Propellant Flow, mA	Magnetic Baffle Excitation, Amp-Turns	No. of Control Coil Turns	Mode of Baffle Operation
1100	2.0	37	185	97.3	100	39	14	Active
1100	2.0	37	185	95.6	100	45	14	Active
1100	1.5	37	185	90.9	94	34	14	Active
1100	1.5	37	185	92.9	89	34	4 1/2	Passive
1333	1.5	37	185	93.2	98	34	4 1/2	Passive
1333	1.0	37	185	83.6	101	23	4 1/2	Passive

T1346

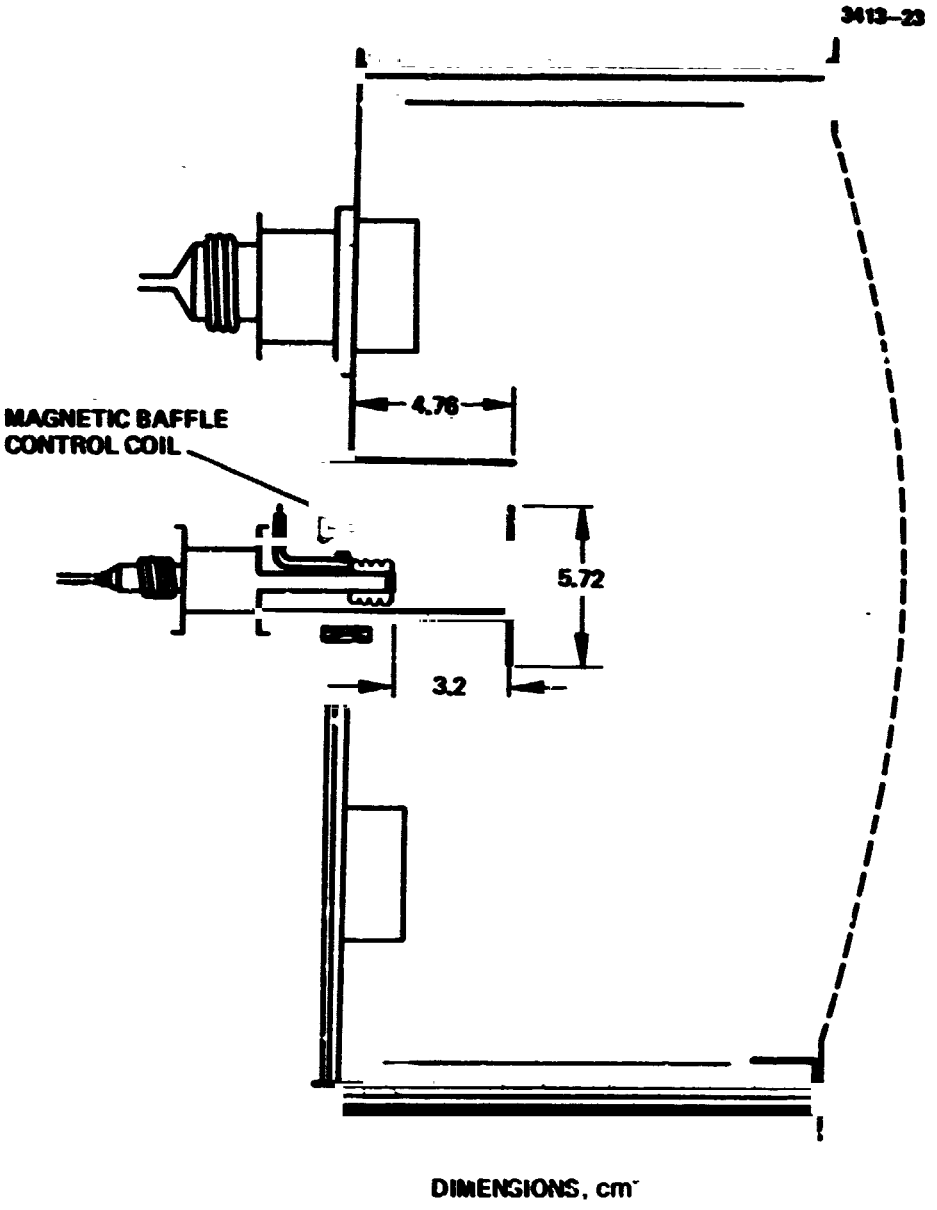

Fig. 17. Schematic diagram of 400 series discharge chamber with modified cathode location.

TABLE 9

Discharge Chamber Parameters for the Configuration Shown in Fig. 14

Beam Current, A	Discharge Voltage, V	Discharge Loss, eV/ION	Discharge Mass Utilization, %	Cathode Propellant Flow, mA	Magnetic Baffle, amp-turns
2.0	37	185	96.7	76	14
2.0	37	185	95.5	80	18
1.48	37	188	92.8	112	19
Beam Voltage 1100 V Accel Voltage 500 V Magnetic Baffle Coil 3.5 Turns					

T1347

In addition to the performance evaluations, parameter comparisons and conventional thruster documentation which took place during this development program some new insights into discharge chamber operation have been formulated. Foremost is the realization that all discharge chambers of this basic design which were tested under this program exhibited oscillations in discharge current to some degree. While basic research in this area is meager, a number of experimental observations during this program, and reported elsewhere, indicate that electron flow from the hollow cathode plasma across the magnetic field of the cathode pole and into the main discharge volume is anomalous and dependent on some type of plasma turbulence. It has been empirically determined that the discharge conditions can be adjusted to obtain coherent oscillations in discharge current by adjusting parameters which affect the magnetic field, neutral density or plasma density in the baffle gap vicinity. The frequency and amplitude of these oscillations is usually such that there is no reason to suspect any appreciable impact on discharge chamber or thruster performance. For this reason, a detailed discussion of these oscillatory characteristics is deferred to the discussion on power conditioning interactions in Section V.

E. Preliminary Evaluation of 700 Series EM Thruster Discharge Chambers

Except for the permanent magnet specification, fabrication and preliminary testing of the first EM thruster module (SN 701) proceeded under the low voltage thruster program (NAS 3-16528) without incident. Two difficulties were encountered in obtaining the required field distribution. The first was a fundamental problem associated with absolute specification of permanent magnets. It had been considered that by specifying material and dimensions all magnets would be obtained from the vendor with equal strength. This assumption was found to be erroneous, and an absolute means of assuring equal magnet strength or magnetization has not yet been formulated, although progress is being made under an internal HRL program. The second difficulty arose from a modification in the retainers for the radial magnets which had been

introduced into the EM thruster design to save weight. This modification is illustrated in Fig. 18. In order to achieve the desired field distribution in the first EM design thruster, SN 701, it was necessary to employ a trial and error technique, selecting radial and axial magnets from stock until the measured field values were in favorable agreement with those measured in thruster 301-A. Table 10 compares this distribution of magnetic field values with those obtained by appropriate selection of radial magnets with the first two 700 series thrusters and thruster 301 modified to duplicate the EM magnet retainer design (301-B).

As compared in Table 11, the initial discharge chamber performance parameters obtained with the first EM thruster were in good agreement with those obtained with the laboratory version of the EM design embodied in thruster 301-A. These data were all obtained using a 5.1-cm diameter baffle; however, continued operation of thruster 701 was observed to require ever increasing magnetic baffle coil current to avoid discharge mode shifting. Installation of a 5.4-cm diameter baffle corrected this situation and is thought to be another consequence of the magnetic circuit difference shown in Fig. 18. Insofar as this program was concerned, this completed the activity in verifying the EM thruster discharge chamber specifications. Representative thruster performance parameters, including corrections for beam divergence and double-charged ions, are listed for full power, three fourths power, and half power levels in Table 12 (throttling at nearly constant specific impulse).

From a discharge chamber efficiency standpoint, the performance of the EM thruster design as documented under this program is exemplary and requires no further optimization. Some relatively minor difficulties were encountered in obtaining reproducible results on a week to week basis insofar as operational characteristics and thruster transfer functions are concerned. On the basis of the data obtained under this program, it has not been possible to identify these performance variations with either thruster design characteristics procedural variations, or test facility conditions, and additional performance testing will be required to fully document and verify all operational aspects of this design.

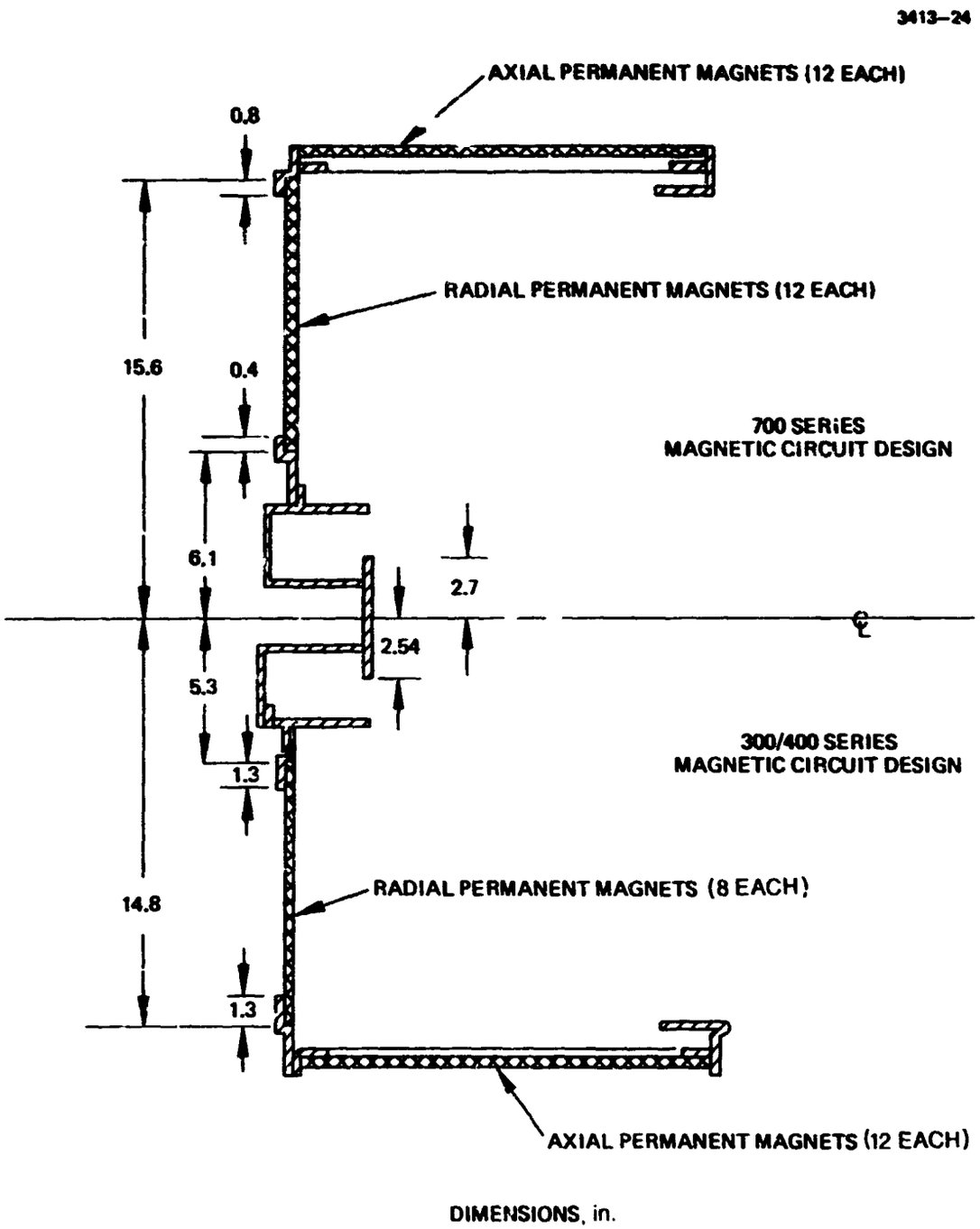

Fig. 18. Comparison of magnetic circuits in modified 301/400 series thrusters (301A) and 700 series thrusters (701).

TABLE 10

Comparison of EM Design Thruster Magnetic Field Distributions

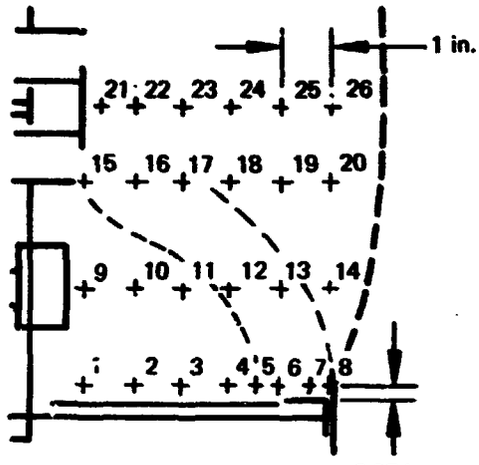

MEASUREMENT GRID

	Axial Magnetic Field Values-Gauss				Radial Magnetic Field Values-Gauss			
Thruster SN	301-A	301-B	701	702	301-A	301-B	701	702
Measurement Grid Location								
1	-4.4	-2.9	-2.3	-3.1	12.0	16.4	14.8	12.3
2	1.8	2.6	2.9	2.9	9.5	11.0	10.2	9.7
3	5.3	5.7	6.0	6.3	7.0	7.9	7.8	7.3
4	8.1	8.3	8.5	9.1	6.0	7.2	7.1	6.4
5	10.7	9.7	10.3	10.9	7.5	8.9	10.2	7.8
6	14.8	9.7	11.9	12	17.5	15.7	16.8	15.7
7	3.1	2.0	2.6	3.2	18.0	13.8	15.7	14.3
8	-9.2	-5.1	-6	-5.3	7.0	7.8	9.2	8
9	12.5	16.1	14.4	16.9	31.0	29.1	28.9	30
10	13	14.3	13.7	14.9	18.6	18.1	17.8	18.3
11	11.6	12.2	11.8	12.9	12.5	12.1	11.9	11.8
12	10	9.7	9.6	10.5	9.0	9.6	8.9	8.8
13	6.8	6.8	6.9	7.4	7.0	8.1	7.6	7.2
14	3.6	3.3	3.4	4.0	5.5	6.0	5.8	5.6
15	112	104	110	90	29.5	27.8	28.1	20.0
16	42	38.4	38.5	39	15.0	13.4	13.4	13.0
17	26	23.5	24.4	25.1	8.9	8.3	8.4	8.2
18	16.6	15.3	15.6	16.5	5.3	5.9	5.3	5.0
19	10.5	10.2	10.5	11.1	3.5	4.5	3.8	4.0
20	6.7	6.6	6.7	7.1	2.5	3.2	2.9	2.8
21	60	49.2	49.5	61.5				
22	45	39.5	41	42				
23	29	26.2	26.8	27.9				
24	19	16.6	16.9	18				
25	12	11.1	11.2	12				
26	8	7.1	7.1	7.65				

T1217

TABLE 11

Comparison of Discharge Chamber Performance Obtained
With Thrusters 301-A and 701

Thruster, SN	Grid System, SN	Beam Current, A	Discharge Voltage, V	Discharge Losses, eV/ion	Cathode Propellant Flow, mA (equiv)	Discharge Propellant Utilization, %	Baffle Coil, amp-turns
301-A	644	2.0	37	185	100	95.6	45
701	645	2.0	37	185	90	95.6	54
301-A	645	1.50	37	185	94	90.9	34
701	645	1.45	37	185	108	92.7	54
301-A	644	1.0	37	185	101	83.6	23
701	645	0.85	37	185	92	82.2	19

T1339

TABLE 12

Representative Thruster Parameters for the EM Thruster Design

Parameter	Full Power			3/4 Power			1/2 Power		
	Voltage, V	Current, A	Power, W	Voltage, V	Current, A	Power, W	Voltage, V	Current, A	Power, W
Ion Beam	1100	2	2200	1150	1.45	1667.5	1350	0.85	1147.5
Accelerator	500	0.0039	2	500	0.0025	1.3	500	0.0016	0.8
Discharge	37	10	370	37	7.25	268.3	37	4.25	157.3
Magnetic Baffle	0.65	10	6.5	0.45	7.25	2.3	0.25	4.25	1.1
Main Vaporizer	5.3	0.9	4.8	5.5	0.9	5.0	4.8	0.8	3.8
Cathode Vaporizer	2.9	0.9	2.6	3.2	1.0	3.2	3.3	1.1	3.6
Neutralizer Vaporizer	3.0	0.7	2.1	3.4	0.72	2.4	3.8	0.9	3.4
Cathode Keeper	5.0	0.4	2.0	5.0	0.4	2.0	7.0	0.4	2.8
Neutralizer Keeper	14.0	1.3	18.2	14	1.3	18.2	14	1.3	18.2
Neutralizer Coupling	11	2.0	22	10.5	1.45	15.2	11	0.85	9.4
Total Power	2630.2			1986.4			1338.6		
Propellant Flow	Amp (Equivalent)			Amp (Equivalent)			Amp (Equivalent)		
Main Vaporizer	2.0			1.466			0.941		
Cathode Vaporizer	0.090			0.085			0.092		
Neutralizer Vaporizer	0.025			0.025			0.038		
Total	2.125			1.574			1.071		
Electrical Efficiency	83.6			83.9			85.7		
Propellant Efficiency	94.1			92.1			79.4		
Total Efficiency (Meter Value)	78.7			77.3			68.0		
Thrust Factors									
Doubly Charged Ions	0.958			0.96			0.981		
Beam Divergence	0.993			0.993			0.993		
Efficiency Correction	0.905			0.922			0.949		
Corrected Efficiency	71.2%			71.2%			64.5%		
Corrected Propellant Utilization	87.3%			86.8%			76.9%		
Effective Specific Impulse	2900 sec			2920 sec			2800 sec		
Corrected Thrust	29.5 mlb			21.9 mlb			14.1 mlb		
Power/Thrust	89.2 W/mlb			90.7 W/mlb			94.9 W/mlb		

T1348

F. Investigation of Discharge Chamber Configurations to Improve Ion Beam Uniformity

Development of a discharge chamber that produces a plasma which is uniform in density over the entire ion extraction surface has been one of the secondary goals of this program. When operated with flat grids, the radial hybrid magnetic configuration produced an ion beam with considerably improved uniformity in current density. This section describes other configurations which were evaluated to find a more stable substitute for this geometry.

The first configuration investigated made use of the versatile electromagnetic discharge chamber in the configuration shown in Fig. 19. The discharge chamber could be operated in either a divergent magnetic configuration by connecting the radial and axial electromagnets in "aiding" polarity or as a two cusp, boundary magnetic configuration. The primary electrons from the cathode plasma were introduced at relatively large radius in comparison to other thruster geometries with the intention of getting more ionizing collisions at larger radii. The extracted ion beams for both modes of operation were quite uniform (see Fig. 20); however, the discharge chamber efficiencies were unacceptable. Propellant utilization could not be increased above 80% even at discharge losses greater than 400 eV/ion. As a matter of curiosity, double charged ion production was measured for this thruster configuration and found to be extremely low (5% as compared to the usually observed 12 to 15%). Whether the low percentage utilization of the beam uniformity was responsible for this double charged ion production could not be determined.

The substandard performance of the discharge chamber configuration shown in Fig. 19 was attributed, at least in part, to the relatively large cathode plasma volume. The thruster was modified as shown in Fig. 21 to reduce cathode plasma volume while retaining the same discharge chamber magnetic geometry. Some improvement in discharge chamber efficiency was achieved by this modification; however, performance still fell far below that of the EM thruster design, and the uniformity of the beam profiles was not greatly different from that of the EM thruster (Fig. 22).

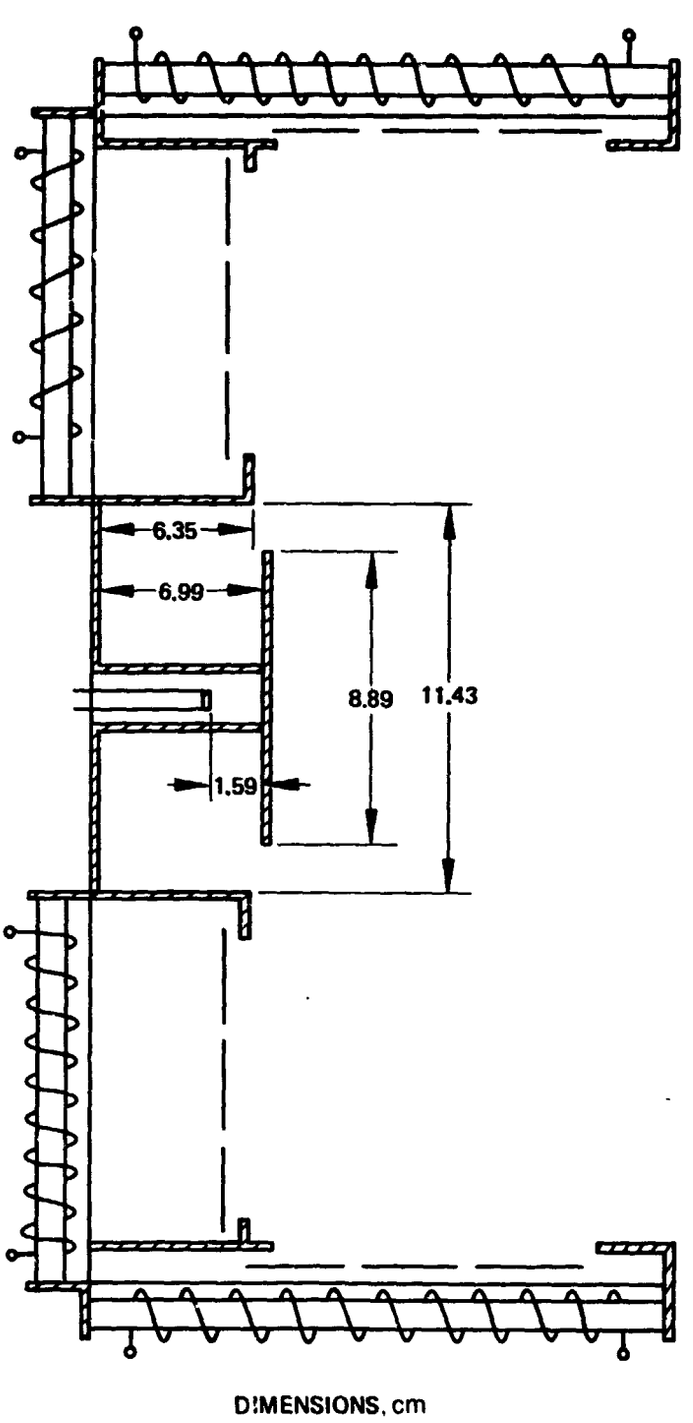

Fig. 19. Diagram of thruster geometry with electron injection area expanded to produce uniform ion beam profile.

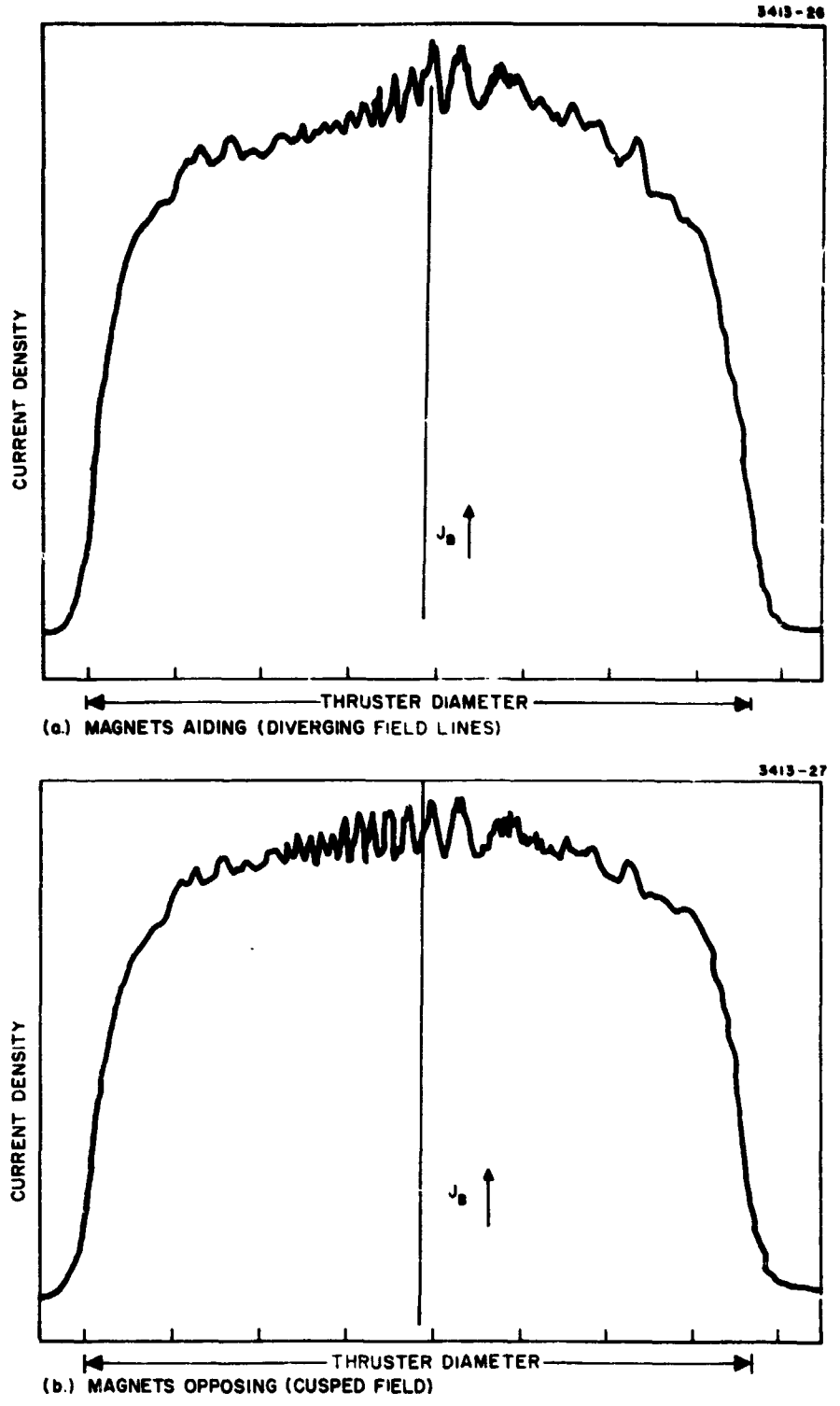

Fig. 20. Beam current density profiles for discharge chamber shown in Fig. 15.

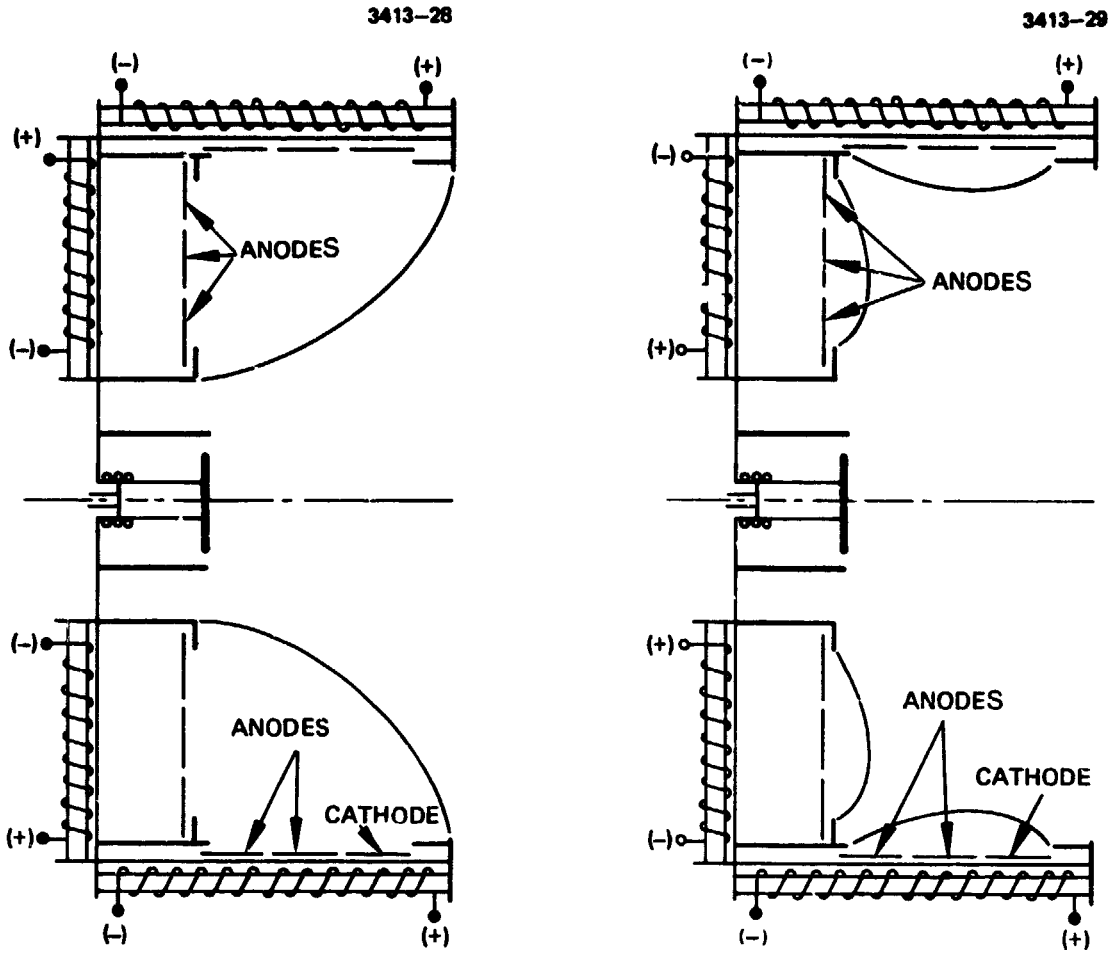

(a) DIVERGING FIELD SHAPE (MAGNETS AIDING)

(b) CUSPED FIELD SHAPE (MAGNETS OPPOSING)

Fig. 21. Magnet currents and field shapes for two conditions showing appreciably different beam current density profiles, see Fig. 11.

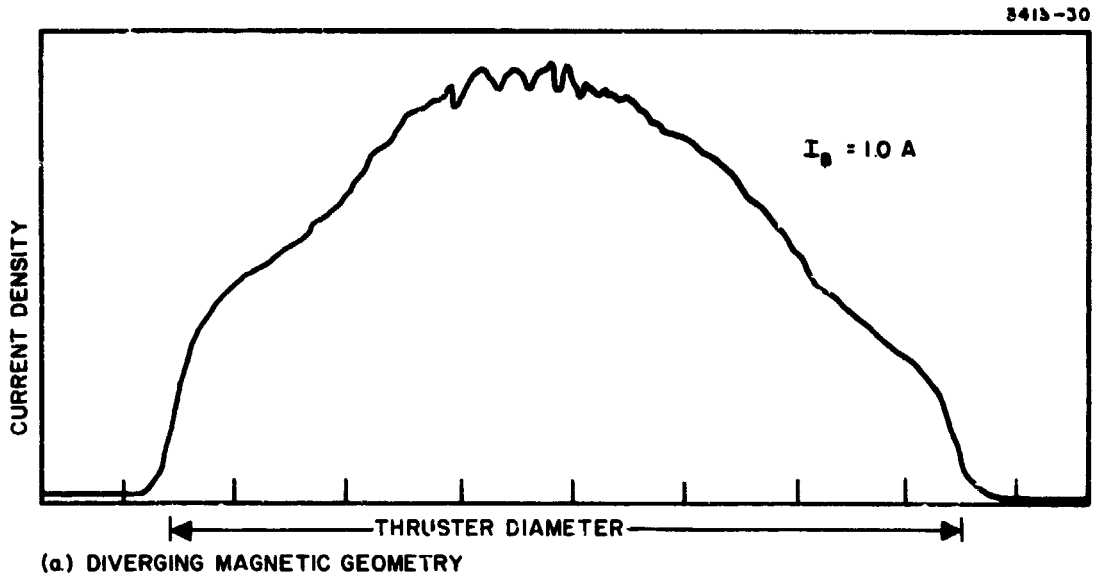

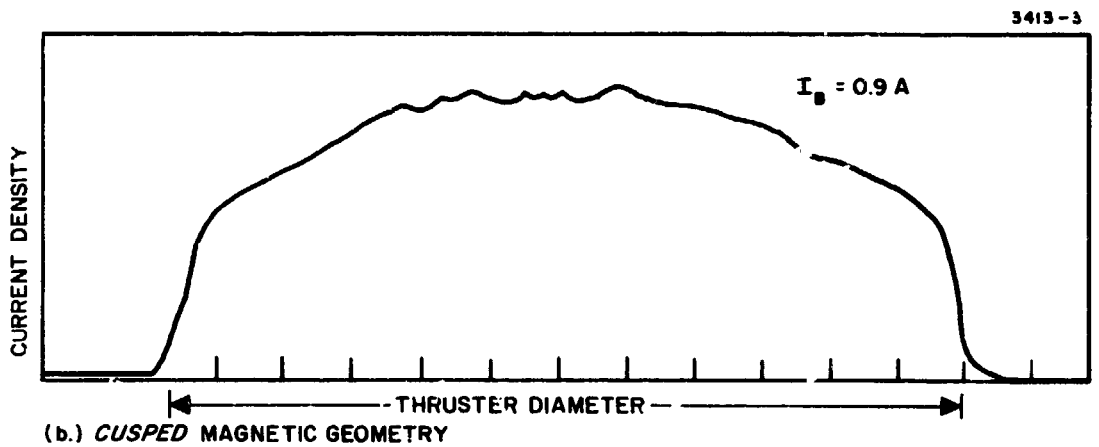

Fig. 22. Beam current density profiles for thruster conditions shown in Fig. 17.

The final efforts to restore both discharge performance and beam uniformity under this program are represented in the configurations shown in Fig. 23. The discharge chamber shown in Fig. 23(a) made use of the same magnetic field geometry but relocated the cathode plasma and injected electrons radially into the main discharge chamber region. Again, the magnetic field could be operated as either a divergent or boundary configuration. As before, discharge chamber performance was relatively poor (about 90% utilization at 350 eV/ion discharge loss). Figure 24 compares the ion beam profiles obtained by operating this discharge chamber in the two magnetic configurations. The cusp magnetic geometry operated at slightly lower propellant utilization and produced a reasonably uniform beam current. The thruster discharge chamber shown in Fig. 23(b) represents a single boundary cusp geometry which was intended to provide a field free central discharge region. The ion beam current distribution obtained with this discharge chamber (Fig. 25) differed very little from the EM thruster design, and again the performance does not approach that of the EM thruster discharge chamber.

While this activity represented a somewhat negative result, it emphasizes the high degree of refinement which the EM thruster design represents. It is possible that with considerable optimization, one of these configurations could be tuned to the same state of development, however, considerable effort could be required. A second notable point is that the ion beam current distribution could not be changed appreciably by a variety of configurations, and only the discharge chambers of the radial field type have produced beams having remarkably uniform current densities without significant performance loss. Consequently, future attempts at developing discharge chambers with improved beam uniformity would probably be most successful with use of a radial or radial hybrid type magnetic geometry.

G. Summary of Discharge Chamber Investigations

The developmental efforts described in the preceding sections represented an intense effort to identify a discharge configuration which could meet the discharge chamber efficiency goals for this program while

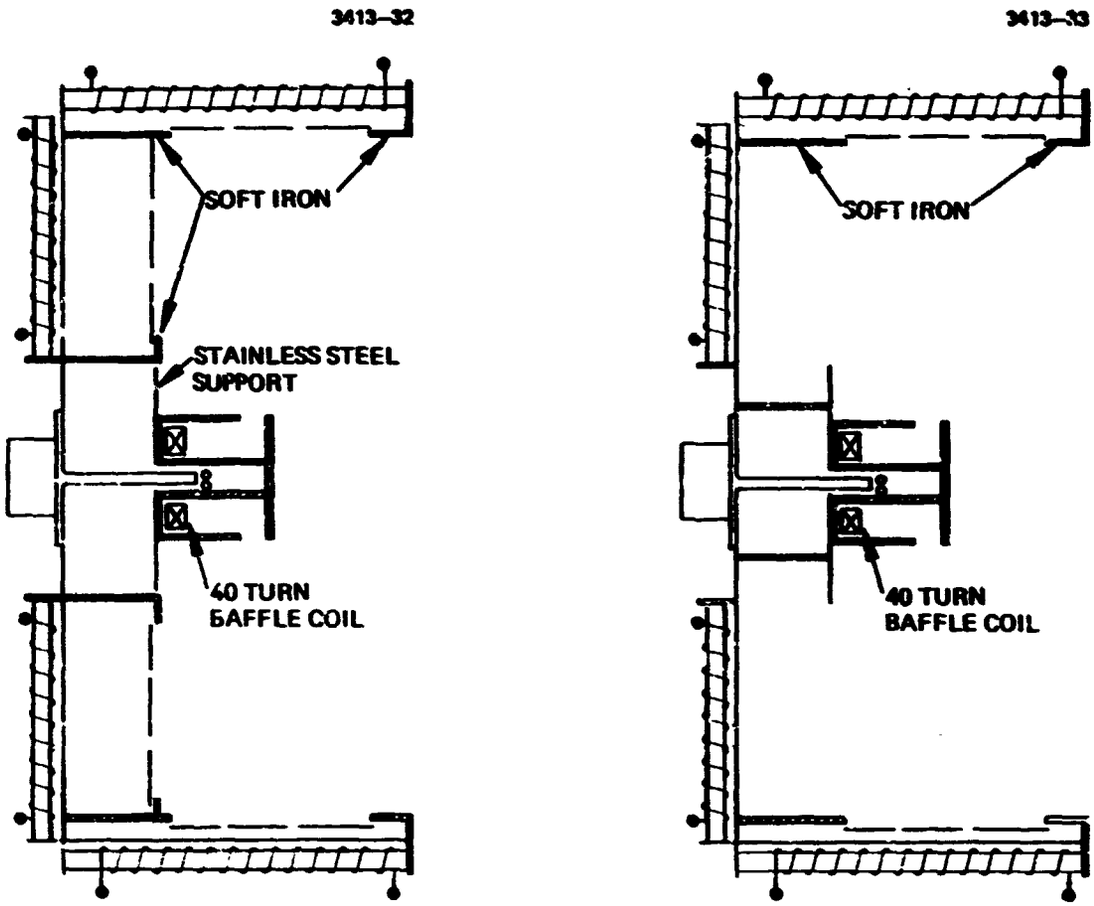

(a) DIVERGING OR CUSP FIELD GEOMETRY WITH RADIAL ELECTRON INJECTION

(b) SINGLE BOUNDARY CUSP FIELD GEOMETRY WITH RADIAL ELECTRON INJECTION

Fig. 23. Thruster configurations evaluated for beam uniformity.

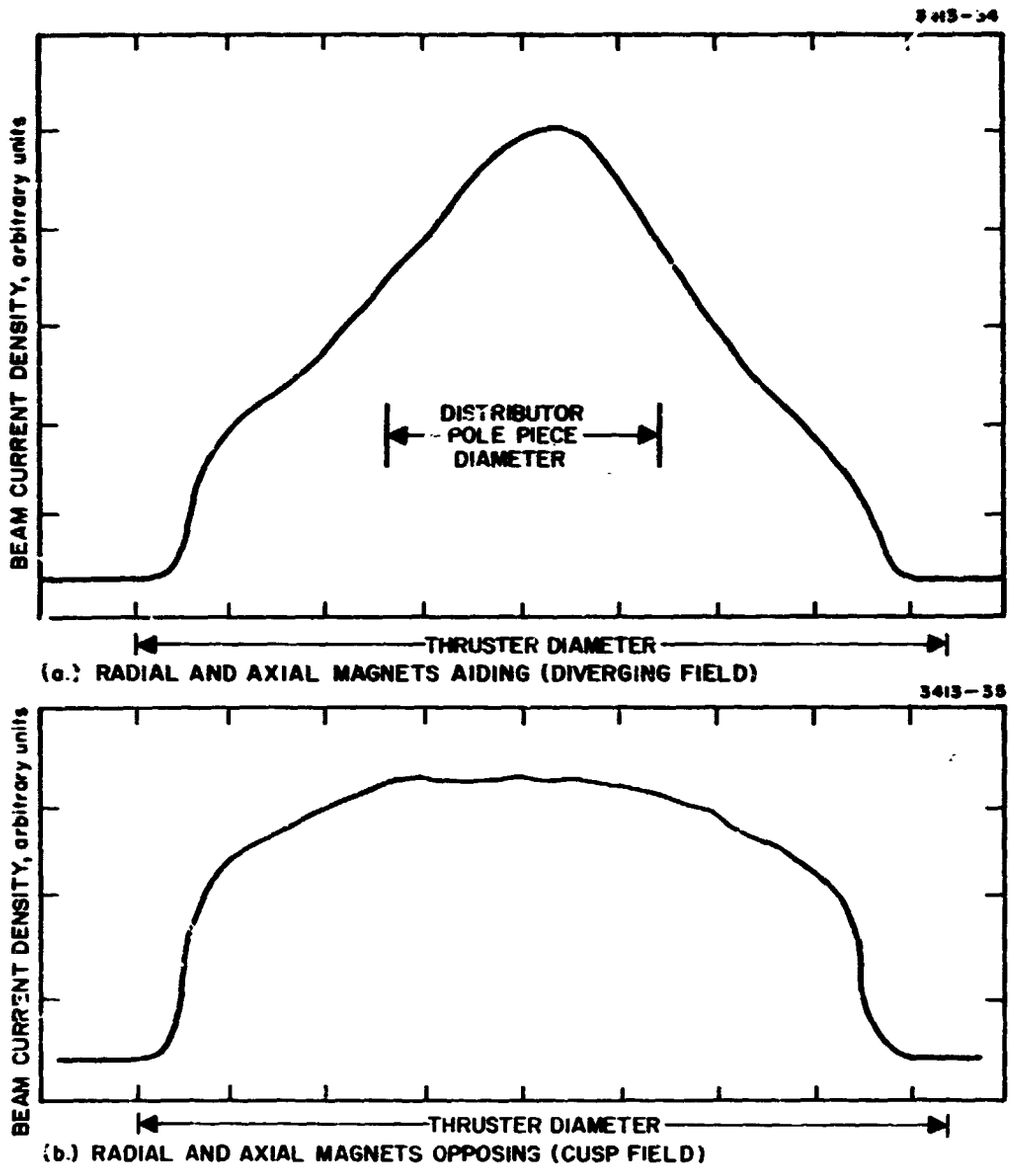

Fig. 24. Beam current density distributions for the thruster configurations shown in Fig. 19(a).

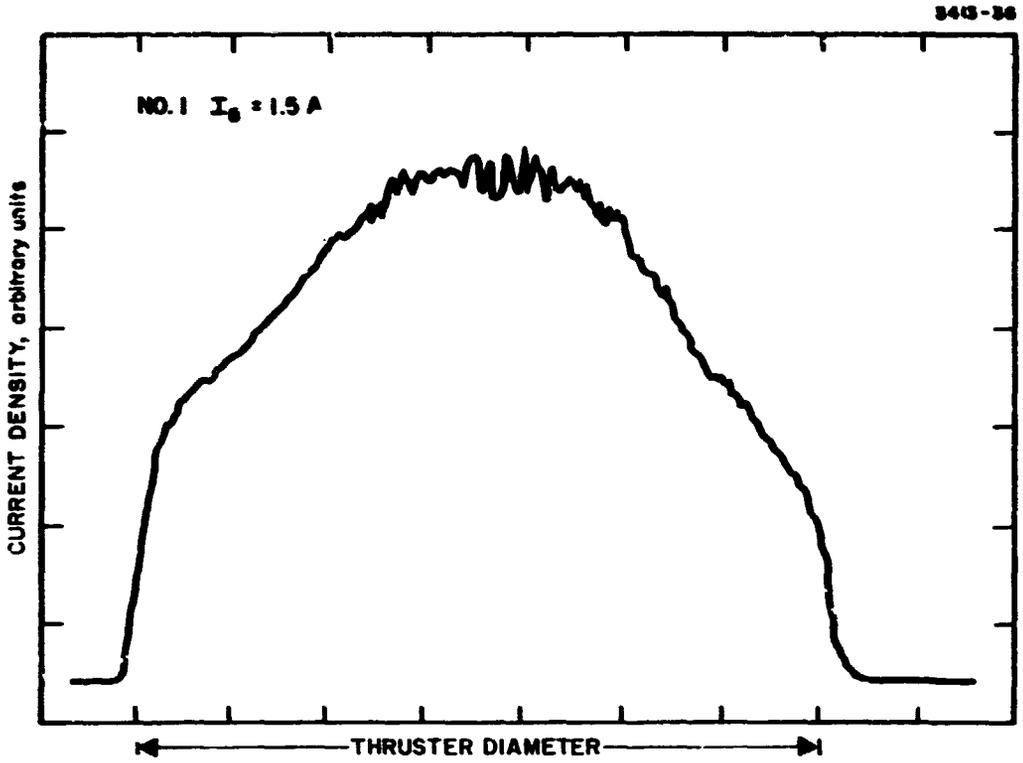

Fig. 25. Beam current density distribution for the thruster configuration shown in Fig. 19(b).

satisfying a number of secondary requirements as well. The divergent magnetic field configuration most nearly meets these goals at the 2 A beam level with a capability of producing 96% propellant utilization at 185 eV/ion discharge loss. These performance gains are attributed primarily to the ion optical system design and reduction of losses in the cathode plasma region. While further optimization of these parameters might have reduced the discharge losses to surpass the program goal of 170 eV/ion or less, it was considered more important to investigate and satisfy the alternate requirements necessary to transfer this technology to the EM thruster programs. Among the requirements considered were operational constraints on thermal properties, component lifetime and control stability. The identification, documentation, and elimination of potential problems provided for incorporation of the improved divergent field discharge chamber into the engineering model (EM) thruster development without difficulty.

Investigation of several other discharge chamber configurations has provided insight and documentation which form a basis for identifying critical parameters affecting discharge current oscillations, ion beam uniformity, and double charged ion parameters. This basis is essential to future discharge development in that gains to overall thruster efficiency may be more closely related to eliminating, or at least diminishing, discharge oscillations or double charged ion production than to reduction of discharge losses by a few eV/ion. Further gains may also be anticipated from improved ion optical systems as discussed in the following section.

III. ION OPTICAL SYSTEM DEVELOPMENT

The early development of the "dished grid" ion optical system under the concurrent EM thruster programs greatly reduced the scope of activity originally planned for this program. Initial evaluation of this type of structural design showed that the domed or dished grid systems had excellent mechanical stability under both thermal and mechanical stresses. Variables which remained to be investigated under this program were "dish depth" (or radius of curvature), hole pattern design, and compensation for the divergent beam trajectories which result from the grid curvature. Refinements in fabrication and assembly techniques were improved of necessity as a part of this program, however discussion of these contributions is deferred to Section VI. This section concentrates on a description of the dished grid ion optical system and the investigation and evaluation of its performance under this program.

A. Description of the Dished Grid Ion Optical System Subassembly

The dished grid ion optical system makes use of spherically dished, or domed, electrodes to provide structural stability. The grids are mounted from a rigid tubular structure which had been developed earlier for flat grid ion optical systems as shown in Fig. 26. The screen and accelerator electrodes are formed in pairs by hydroforming a flat molybdenum sheet which has been imprinted with a masking substance to provide for chemically milling the holes (performed by Buckbee-Mears Inc.). After hydroforming, the grids are chemically milled and then heat treated while clamped in a fixture to relieve internal stresses. Stiffening rings made of heavier gauge molybdenum are then fastened to the thinner grid material by brazing or with mechanical fasteners. When mounted on the support structure, as shown in Fig. 26, the ion optical system becomes an independent subassembly which can be used on any thruster equipped with suitable mounting brackets. The main variables of the ion optical system are the dimensions of the screen and accelerator grid holes, the hole patterns, and

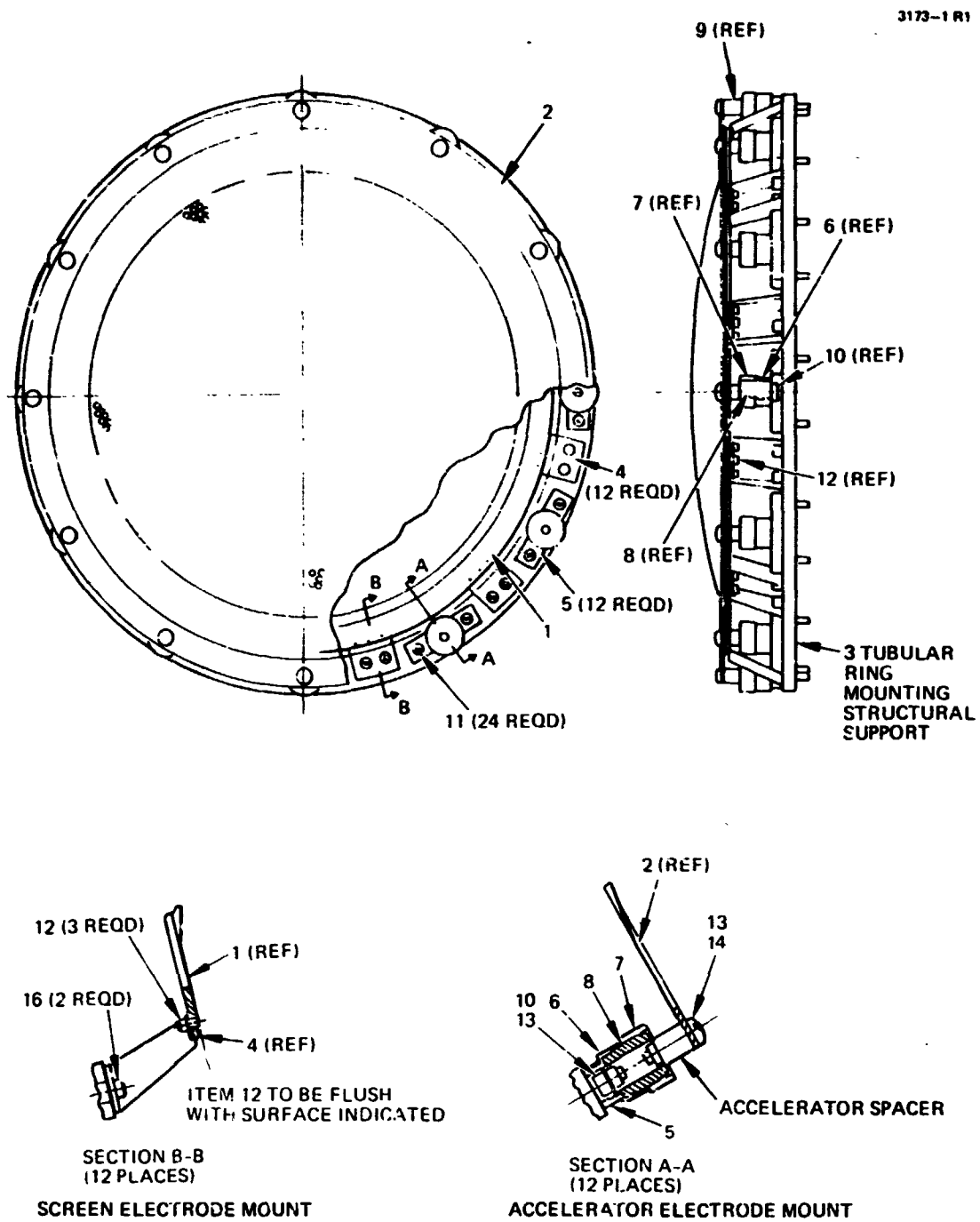

Fig. 26. Dished grid ion optical system assembly.

the depth of the dish. Table 13 contains the specifications of all the grids fabricated or tested under this program. A number of these grid sets have similar specifications, and performance differences were observed primarily as a function of inadvertent fabrication and assembly variations discussed below and in Section VI.

B. Ion Optical System Effects on Discharge Chamber Performance

Discharge chamber efficiency, stability and control functions have been found empirically to be critically dependent on the properties of the ion optical system. It has been known for some time that reduction of the screen grid transparency or open area fraction results in higher discharge losses, increased difficulty in isolating cathode and main discharge plasmas, and a beam current distribution which is highly concentrated near the thruster axis. While most of the variations in grid hole pattern and diameter under this program were directed towards reduction of thrust losses arising from beam divergence and double charged ions, data obtained in the evaluation of these variations have pointed out an important factor about the accelerator electrode design. Under the Low Voltage 30-cm Thruster Program and briefly during early experiments under this program, grid sets were evaluated which had a wide range of variation in screen and accelerator open area or transmission. Through use of hexagonal aperture shapes, it was possible to increase the screen grid open area to 79% and it was expected that superior discharge chamber performance would have been achieved as a consequence. What was not recognized initially was that by using the convention ratio of screen to accel aperture size, increasing screen grid transmission also increases the transmission of the accelerator grid, a factor that is now considered detrimental to the achievement of high propellant utilization. In attempting to explain the reduction in propellant utilization observed when a conventional accel electrode was replaced by the electrostatic deflection system used in the 5-cm thruster programs,[4,5] a view factor analysis was made[6] to determine the effect of the accelerator

TABLE 13

Ion Optical System Grid Parameters

Grid Set Serial Number	Screen Grid					Accelerator Grid				System
	Aperture Diameter, cm	Aperture Spacing, cm	Thickness, cm	Open Area, %	Compensation, %	Aperture Diameter, cm	Aperture Spacing, cm	Thickness, cm	Open Area, %	Dish Depth, cm
601	0.216	0.254	0.038	65.5	-	0.191	0.254	0.038	51.2	2.54
609	0.241	0.279	0.038	67.7	-	0.193	0.279	0.076	43.5	2.54
623[a]	0.208	0.234	0.038	79.1	-	0.178	0.234	0.076	57.9	2.54
636	0.241	0.279	0.038	67.7	0.25	0.193	0.279	0.076	43.5	1.0
637	0.241	0.279	0.038	67.7	0.25	0.193	0.279	0.076	43.5	1.3
638	0.241	0.279	0.038	67.7	0.5	0.193	0.279	0.076	43.5	2.1
NASA 281	0.191	0.221	0.038	67.6		0.152	0.221	0.051	43.3	2.1
642	0.191	0.221	0.038	67.6	0.5	0.152	0.221	0.051	43.3	2.1
643	0.191	0.221	0.038	67.6	0.5	0.152	0.221	0.051	43.3	2.1
644	0.191	0.221	0.038	67.6	0.5	0.152	0.221	0.051	43.3	2.1
645	0.191	0.221	0.038	67.6	0.5	0.152	0.221	0.051	43.3	2.1
648	0.191	0.221	0.038	67.6	0.4	0.152	0.221	0.051	43.3	2.1
650	0.191	0.221	0.038	67.6	0.5	0.152	0.221	0.051	43.3	2.1
656	0.191	0.221	0.038	67.6	0.35	0.152	0.221	0.051	43.3	1.5
NASA 35[a]	0.203	0.234	0.038	75.2	0.3	0.122	0.234	0.038	27.2	2.1

[a]Hexagonal Shaped Apertures

T1349

on the reflux of neutral propellant. This analysis, showed that the open area or transmission of the accelerator could significantly affect propellant utilization. Data obtained during grid system evaluation under the Low Voltage Thruster Program (NAS 3-16528) could be characterized by the following observations:

1. Discharge chamber efficiency was not improved by increasing screen grid open area above 65% when screen aperture to accel aperture ratio was held at 1.25 or less.

2. Discharge chamber efficiency improved with increasing dish depth (in the downstream direction).

Selected performance data has been shown in Table 14 for the grid systems evaluated during this program (parameters given in Table 13). Grid system SN 601 not only has less screen grid open fraction than the other systems, but also has greater accel transmission. The resultant performance is consequently seen to be significantly poorer than for the other grid systems. Grid systems 609 through 638 are essentially of the same hole pattern design; however, grids 636 and 637 have reduced dish depth. The results for these systems are in agreement with the observations stated above (for other hole patterns). Grid systems numbered NASA 281 through SN 656 are again all of the same hole pattern, but with the same screen grid open area as those numbered SN 609 through SN 638. The accel transmission is somewhat smaller, however, and the perveance is higher. The increased discharge chamber performance seen is attributed to these two factors. Here again, grid system SN 656 was dished to a reduced depth, and the discharge efficiency was less than for other grid systems of the same hole pattern. Variation in discharge chamber performance is also seen between grids of the same hole pattern, with no discernible difference in thruster parameters or grid system parameters. It is not known with certainty whether this variation implies that experimental error in performance evaluation is greater than has been assumed, or whether there is some real variation which

TABLE 14

Grid System/Discharge Chamber Performance Comparison

Grid System, SN	Beam Voltage, V	Beam Current, A	Discharge Voltage, V	Discharge Loss, eV/ION	Discharge Propellant Utilization, %[a]	Cathode Propellant Flow, mA	Thruster, SN	Magnetic Baffle, amp-turns
601	1100	2.0	38	220	93.6	150	403	35
609	1100	2.0	38	190	97	127	Radial Hybrid	35
636	1100	2.0	38	200	94	73	Radial Hybrid	50
637	1100	2.0	38	190	89	97	301	35
638	1100	2.0	37	200	94.5	67	403-A	44
NASA 281	1100	2.0	37	185	95	66	403-A	45
643	1100	2.0	37	185	91.3	72	301-A	52
644	1100	2.0	37	185	95.6	100	301-A	45
645	1100	2.0	37	185	95.6	100	301-A	45
648	1100	2.0	37	185	94.5	71	701	31
650	1100	2.0	37	185	96.5	81	702	28
656	1100	2.0	37	185	93.3	80	301-B	21
NASA 35	1100	2.0	37	185	99	84	301-B	21
NASA 35	1100	1.5	37	185	96	88	301-B	26
644	1100	1.5	37	185	90.9	94	301-A	34
642	1333	1.5	37	185	95	66	403-A	45
648	1100	1.5	37	185	91.4	80	701	31

[a]Not corrected for double charged ions.

T1350

results from minor variations in either the grid system assembly or installation on the thruster. Grid system SN 643, for instance, was known to be unevenly spaced because of distortion in the grid shape which occurred during brazing of the support rings to the grids. The performance observed with this system became progressively worse with each test, and the data shown in Table 14 represents the performance shortly before this system became inoperable and had to be scrapped.

Finally, near the end of the program, a grid system (NASA 35) which had very high screen grid transmission (75%) and very low accel transmission (27%) was evaluated with excellent results as shown. Summarizing the results of testing this grid system, using typical power inputs in the manner shown previously in Table 12, the overall corrected thruster efficiency was increased to 72.8% at full power and 72% at three-fourths power. These final data tend to establish the validity of the accel open area hypothesis and provide a basis for explaining some other observations as well. With the hypothesis that the reflux of neutral atoms is significant to discharge chamber efficiency, the dish depth and direction now becomes an important factor as well. Figure 27 shows an exaggerated example of what is thought to take place. With curvature downstream as shown in Fig. 27 (a) the neutral atoms are reflected towards the center of the discharge chamber, where the primary electron density is higher and the probability of ionization is greater. This effect would be expected to increase the plasma density in the center of the discharge chamber and reduce the loss of neutral atoms at the periphery. Thus, propellant utilization could be improved and double charged ion production would also be increased, as is observed. If the dish depth is reduced, the effective "focussing" of these neutral atoms would be modified and relatively small changes could affect performance significantly. If the direction of dish depth is changed, as shown in Fig. 27 (b), the neutral atom reflux is directed towards the periphery of the discharge chamber, where few energetic electrons are present and ionization is less likely. In this case, the effect is the opposite of that described above –

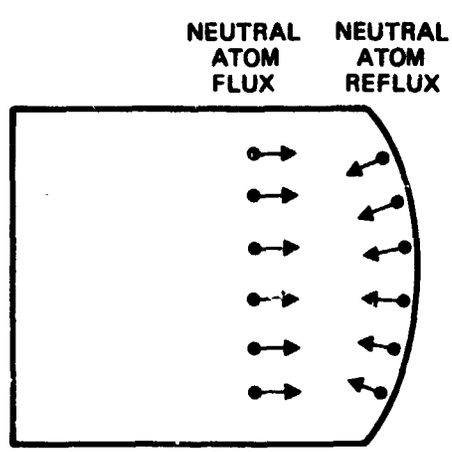

a) CURVATURE OF GRIDS IN THE DOWNSTREAM DIRECTION

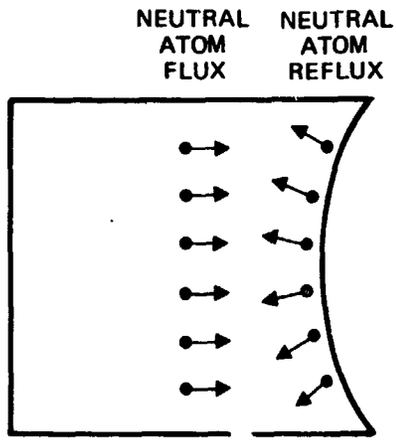

b) CURVATURE OF THE GRIDS IN THE UPSTREAM DIRECTION

Fig. 27. Neutral atom reflux focusing by dished grid ion optical systems.

propellant utilization and double ion production would be decreased, which also agrees with the observed behavior.

While it is now possible to offer a plausible explanation of observed discharge chamber operational characteristics, it is by no means obvious what should be recommended as the ultimate design of ion optical systems. Increasing the dish depth increases the resultant beam divergence and correction of beam trajectories, as described in the following section, is limited to about 2 cm dish depth. Reducing accel open area is also limited in that direct interception will erode away the accel electrode apertures to the diameter required by the individual beamlets, and the performance will deteriorate to whatever value is dictated by the resultant accel transmission. Changing the direction of dish depth to an upstream curvature cannot be ruled out altogether but the discharge chamber requires a modification to get increased electron density near the periphery. Thus it appears that new options have been opened which require further investigation of ion optical system/discharge chamber interactions.

C. Beam Divergence Thrust Loss Evaluation and Reduction

Although initial thruster performance with dished grid systems was quite good in terms of efficiency and perveance, excessive beam spreading was observed even at low accelerator potentials. Because the screen and accelerator grids had the same center-to-center aperture spacing, the hydroforming process caused a "vectoring" of the beam at increasing electrode radius, which produces excessive beam divergence. Thus, a compensation technique was required to reduce this excessive beam divergence. The basic method applied was to adjust the center-to-center spacing of the apertures in the screen grid relative to those in the accelerator so that each individual beamlet is vectored to emerge from the ion extraction system with its axis parallel to the thruster axis of symmetry. The steps required to achieve the desired compensation are shown in Fig. 28. Figure 23 (a) shows the electrodes as they are formed. Angle α is the angle subtended at the center of curvature by the radius vector passing through

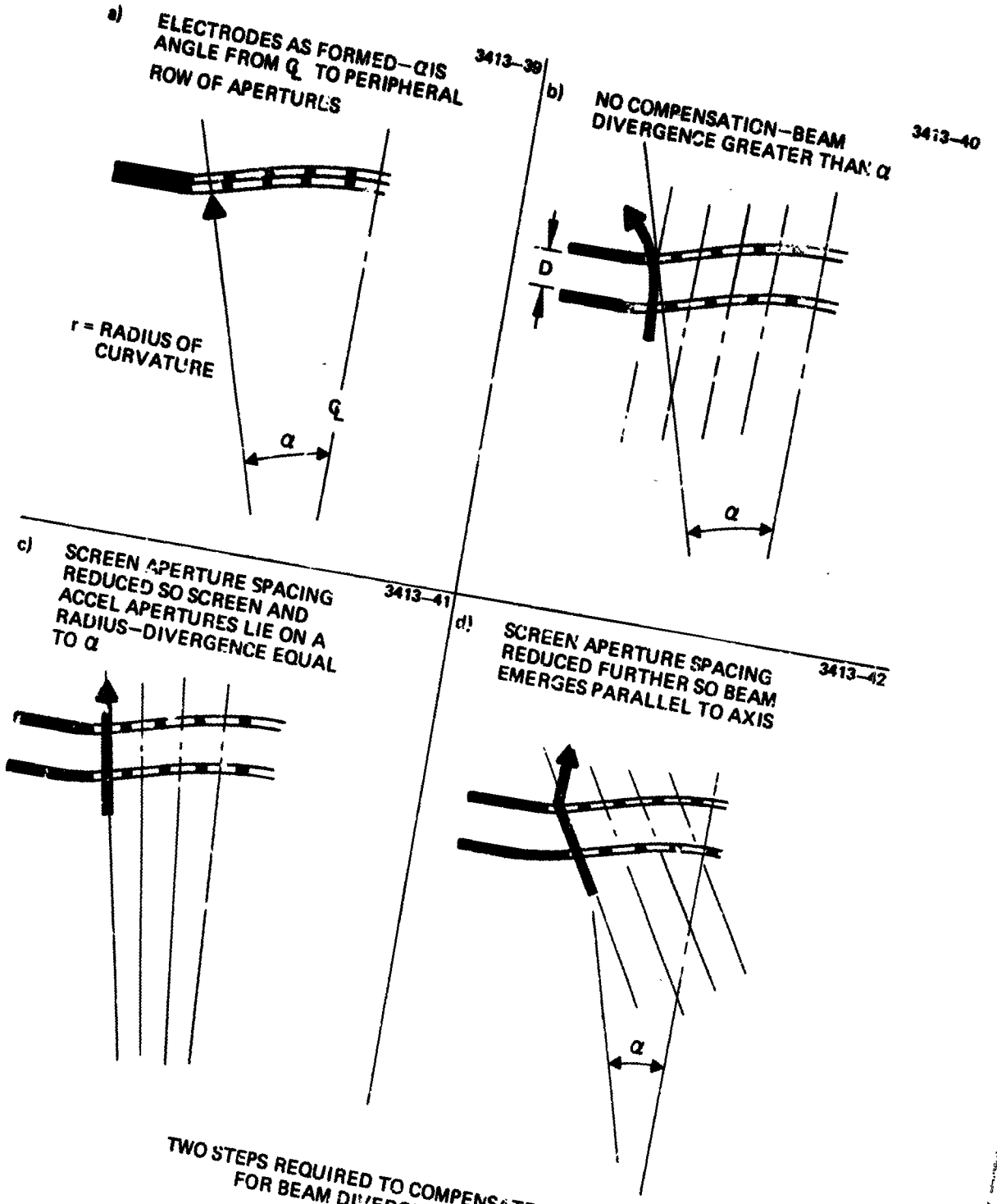

Fig 28. Steps required to offset hole pattern to compensate for beam divergence.

the outermost row of holes in the screen electrode. When these electrodes are separated, as shown in Fig. 28 (b), the apertures in the screen and accelerator are equidistant from the centerline of the thruster. When viewed perpendicular to a plane tangent to the electrode surface at a given radius the screen aperture actually appears to lie outside the radius of the acclerator aperture by a distance d (tan α) and therefore deflects the beamlet to an angle greater than α as measured from the thruster center line. Figure 28 (c) illustrates the electrode system when this misalignment is corrected. The beamlet now passes undeflected through the screen and accel apertures at an angle α with the centerline. If the screen dimension is reduced still further, as shown in Fig. 28 (d), the beamlets are deflected toward the centerline and may be made to lie parallel to the thruster centerline. A fully compensated electrode of the type shown in Fig. 28 (d) should have no more divergence than a flat electrode system with equivalent aperture diameter and spacings. The degree of reduction or compensation of the screen grid hole pattern required to "vector" the peripheral beamlets for minimum thrust loss is dependent on the dish depth, interelectrode spacing, and aperture diameter. An iterative computer technique was developed to evaluate grid compensation for dished optics based on data for thrust vectoring by electrode misalignment. The results of the computation are shown in Fig. 29, where the compensation factor is plotted as a function of dish depth for a fixed aperture diameter and grid spacing. Also shown are the approximate limits for structural stability as well as for direct ion interception. Throughout the program a nominal dish depth of 2 cm was considered standard. Additional optic sets of 1-cm and 1.5-cm dish depth were also assembled and tested. Two compensation factors of 0.5% and 0.4% were used in association with the 2-cm dish depth, while the corresponding factors for the 1-cm and 1.5-cm grids were 0.25% and 0.35%, respectively.

1. Planar Probe Data

In order to evaluate the effectiveness of the compensation technique, data was initially taken with a large planar probe array

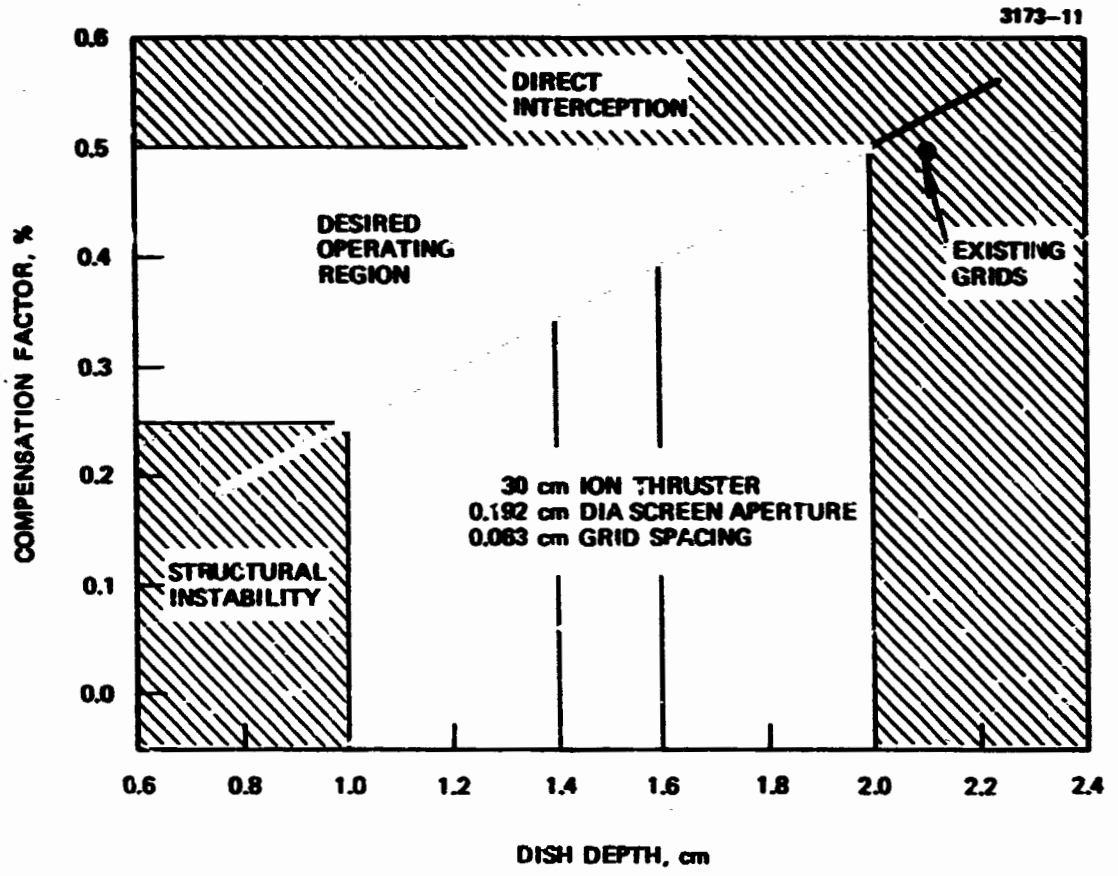

Fig. 29. Data for determining dished grid compensation.

located 48 cm from the thruster. The optics tested during this period were those constructed under the Low Voltage 30-cm Ion Thruster Program and consisted of the uncompensated set SN 623, and two compensated sets SN 636 and SN 638. For all tests conducted during this program, a screen voltage of 1100 V was maintained while a 500 V potential was applied to the accelerator electrode. As seen in Fig. 30, there is a significant decrease in the beam width with the use of compensated optics. The thrust factors shown in the figure are approximate, since the planar probing technique assumes the thruster as a point source. Thus, although beneficial for determining relative changes in beam divergence, a planar probe cannot evaluate an absolute factor, or determine whether an exact degree of compensation has been achieved. However, since dish depths of 1 cm and 2 cm were tested during this period, the compensation technique itself was verified. Not only were the thrust losses reduced, but the high degree of grid stability was maintained with minimum accelerator drain currents.

2. Collimated Probe Data

As mentioned previously, the ion extraction system must be evaluated not only in terms of its ion optical properties, but also in terms of optimum thruster performance. Tests conducted at HRL and at NASA LeRC revealed that smaller diameter apertures, coupled with the discharge chamber modifications as discussed in the preceding section, were sufficient to obtain the higher performance specifications required of the EM thruster design. Thus, during the program redirection it was felt that thruster discharge performance was of primary importance and that beam divergence could then be controlled by accel-decel ratio, and the successfully tested grid compensation technique. The EM thruster ion optical system design specifications are listed below.

Screen aperture diameter	= 0.191 cm
Accel aperture diameter	= 0.152 cm
Center-to-Center spacing	= 0.221 cm
Screen thickness	= 0.038 cm

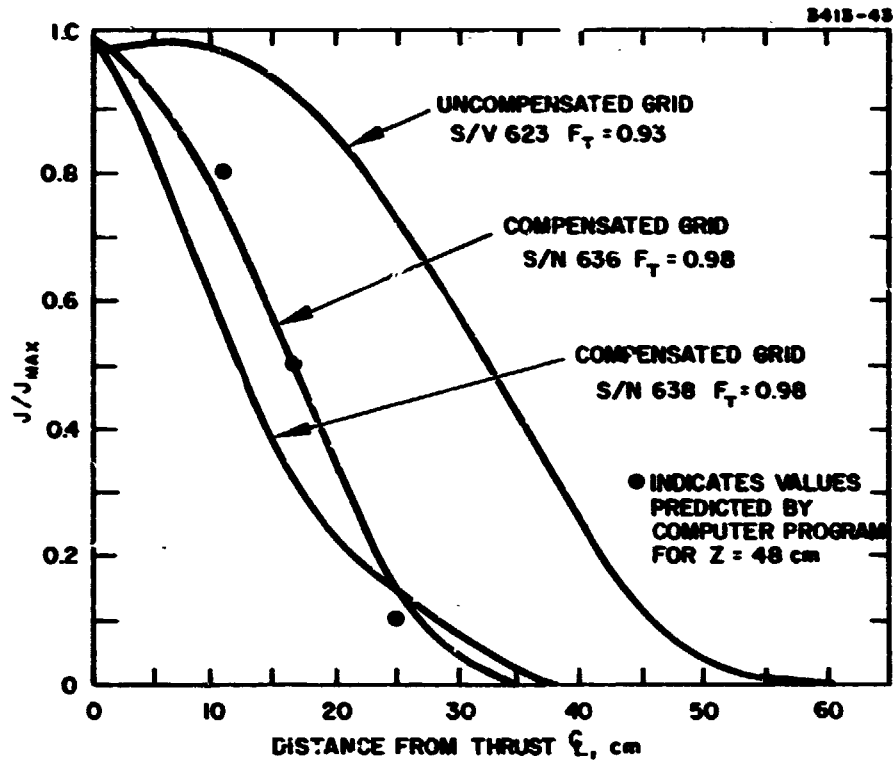

Fig. 30. Comparison of downstream beam current density distributions for compensated and uncompensated screen grids.

Accel thickness	=	0.051 cm
Dish depth	=	2.1 cm
Compensation	=	0.5%
Electrode spacing	=	0.056 cm

In order to completely evaluate the newer systems, a more sophisticated probing technique was developed. The construction of the E x B mass separator probe proved to be a valuable tool not only for the double charged ion measurements but also for the beam divergence evaluation as well. A detailed description of the probe mechanism and the methods of data acquisition and analysis are given in Appendix A. The basic probing technique was to focus on a sufficiently small area of the accelerator grid at equally spaced radial positions, and to sample the ion current at each of these locations over a range of dispersion angles. Figure 31 defines the thruster and probe geometric parameters, r, R and θ used in this discussion. This technique eliminated the point source assumption and provided a more detailed description of ion trajectories. Four grid sets were tested during this period, SN 644 and SN 650, which were identical and were constructed to the specifications as listed above. Grid set SN 656 had similar dimensions, but was dished to a depth of 1.5 cm with a corresponding compensation factor of 0.35%. An additional set, SN 648, was also dished to 2 cm but was compensated at 0.4%. Computer output traces of data obtained with three of the grid sets are shown in Figs. 32, 33, and 34, where the probe collector current is plotted as a function of dispersion angle with the thruster radial position as a parameter. Both the single and the double ion profiles are shown. A number of beam and ion optical system parameters can be evaluated from such plots and each will now be discussed.

- First, the grid compensation factor can be verified. Figures 32 and 33 for optics 644 and 650 show that the curves peak at a relatively constant angle for the thruster radial positions indicated. Figure 34 is typical of grid sets 656 and 648, where there is a shift in the curves towards larger positive angle becoming more pronounced at increased radius.

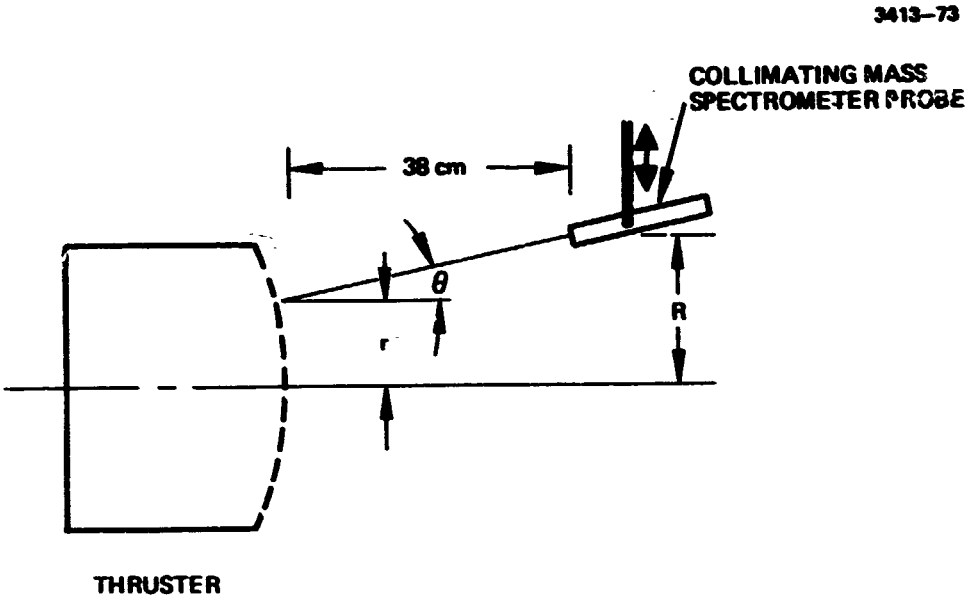

Fig. 31. Diagram showing mass spectrometer probe, thruster, and geometric parameters used in the discussion of probe results.

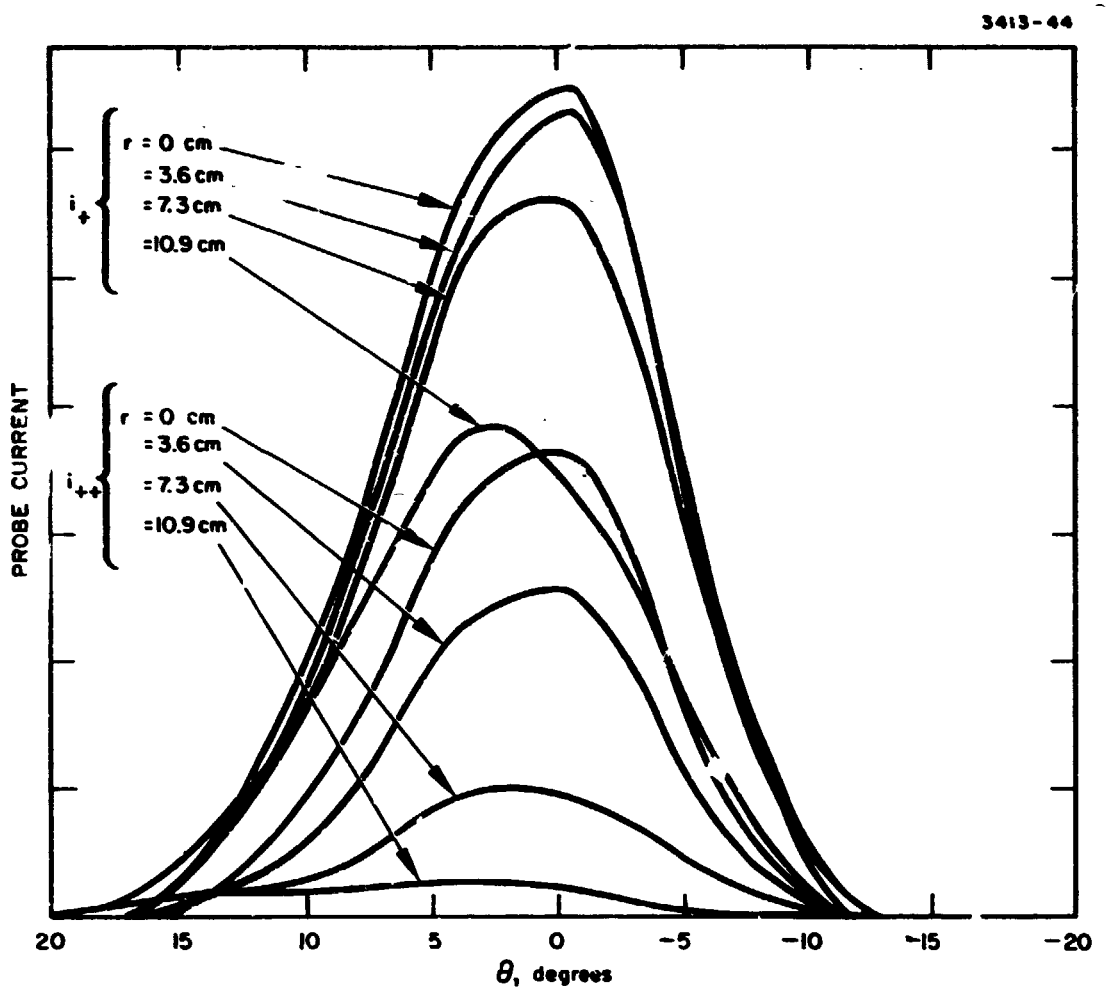

Fig. 32. Computer generated plot of measured ExB analyzer probe currents as a function of theta for r = 0, 3.6, 7.3, and 10.9 cm. Measurements made with grid set SN 644

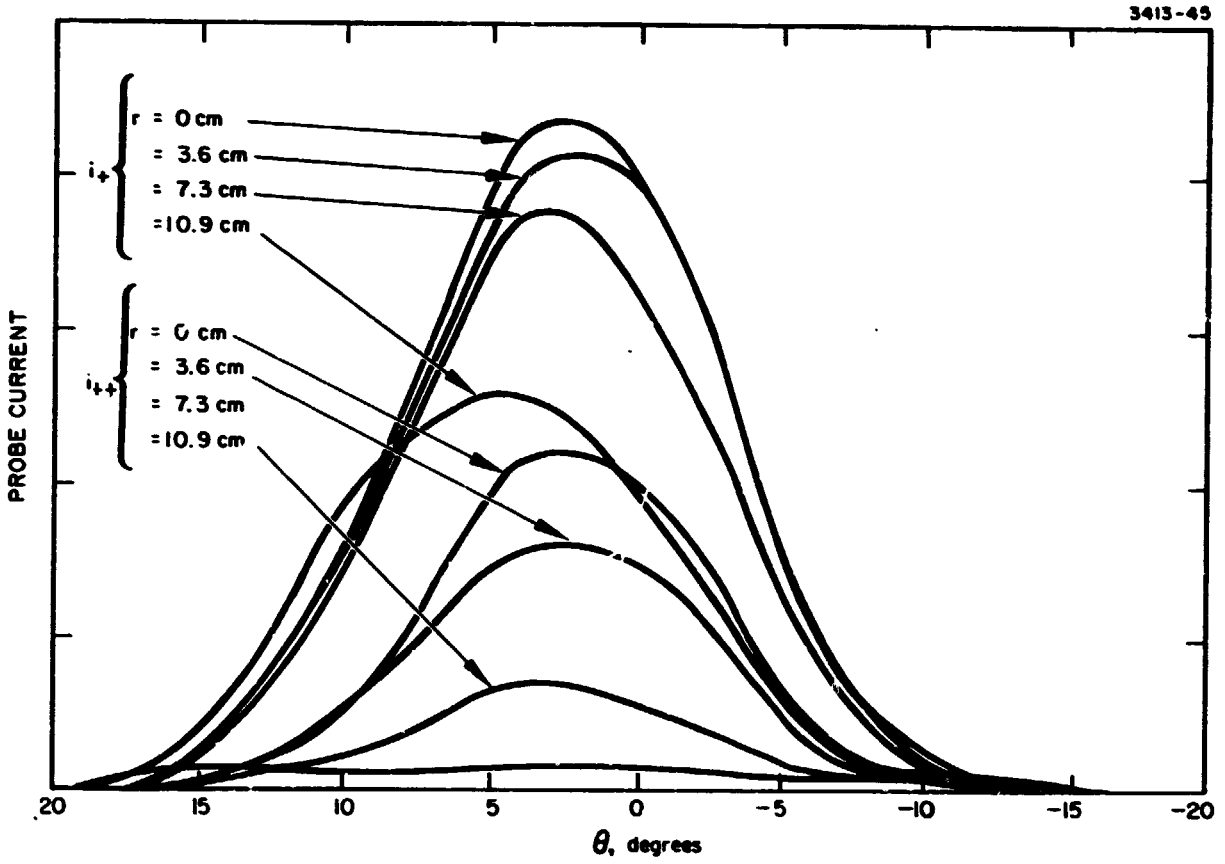

Fig. 33. Computer generated plot of measured ExB analyzer probe currents as a function of θ for r = 0, 3.6, 7.3, and 10.9 cm. Measurement made with grid set SN 650.

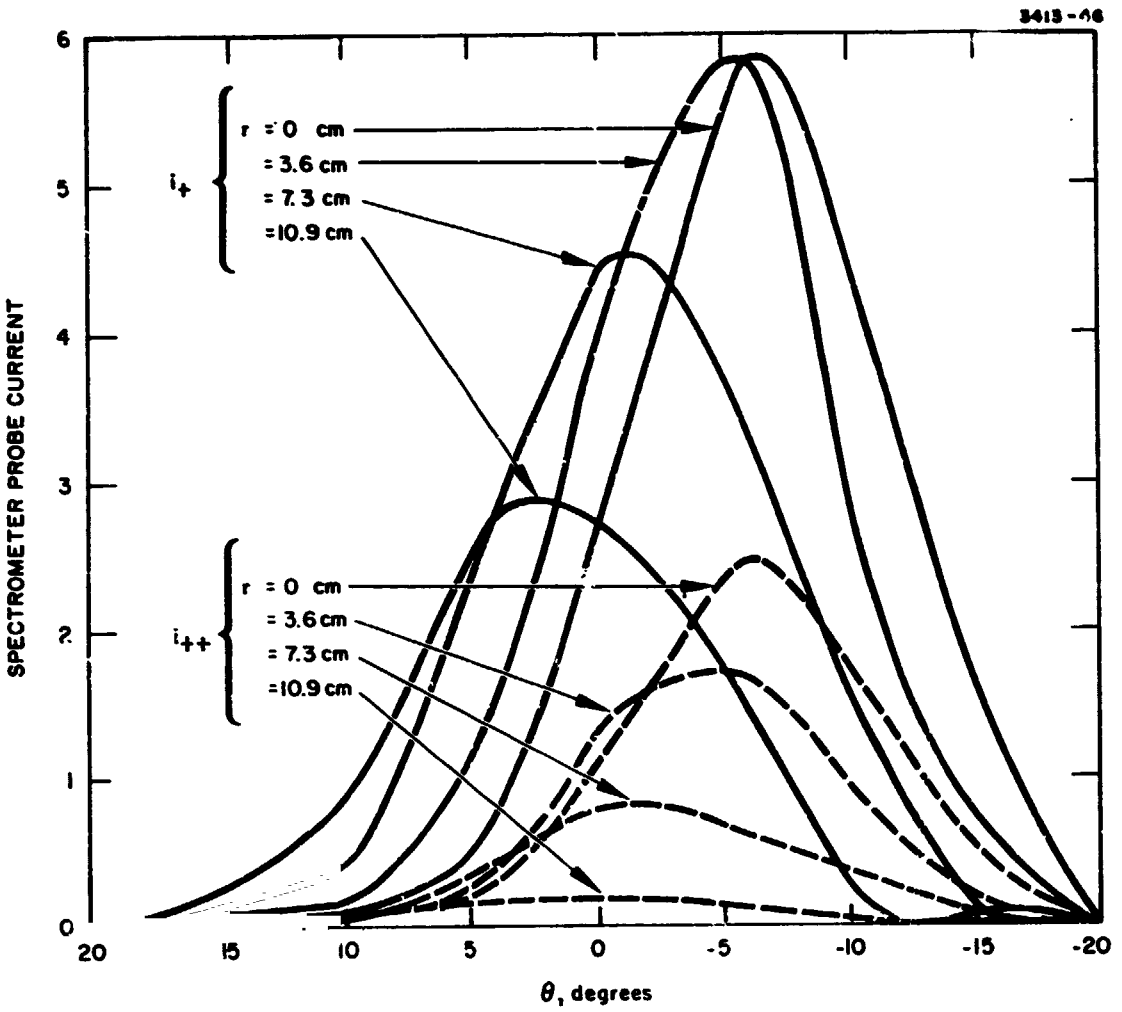

Fig. 34. Computer generated plot of measured ExB analyzer probe currents as a function of θ for r = 0, 3.6, 7.3, and 10.9 cm. Measurements made with grid set SN 656.

These curves indicate an insufficient amount of compensation due either to increased interelectrode spacing or too low a compensation factor. Grids 650 and 644, on the other hand, appear to be fairly well compensated with only the aperture effects contributing to beam divergence.

- The thrust vectoring in the direction of probe motion is the second factor which can be observed from the current versus angle plots. It can be seen that the r = o curves do not usually peak at exactly $\theta = 0$, but rather, are slightly shifted, either positive or negative, depending on the particular optics set. Slight variations in the alignment of the electrodes are felt to be the major causes of this shift.

- The third parameter to be evaluated is the beam divergence thrust factor, which is defined as the ratio of the axial component of thrust to the thrust that would be obtained if all ions were directed along the thruster axis. This parameter is dependent on current density, thruster radius, and dispersion angle (see Appendix A). The divergence thrust factors (F_t) for the various grid sets were computed and found to be 0.994 for optics 644 and 650, while the corresponding factors for 656 and 648 were 0.989 and 0.985, respectively. These parameters remained relatively invariant to changes in beam level or discharge conditions.

- A final item of interest which was observed from the curves for current versus angle was that the single ions were slightly more divergent than the double ions. This is shown in Fig. 35 where normalized profiles for both species are plotted at r = o. Tangential velocity components at the sheath can have an effect on the final ion trajectories, and as shown in Fig. 36 can account for the different divergent properties of the two species. The only way the tangential velocity components can be the same for both species, however, is for the double charged ions to be more axially directed. This suggests the existence of an axial potential gradient which would have a greater directionality effect on the double ions. Thus, the probing system used for these tests cannot only evaluate beam properties, but can give an insight into discharge chamber properties as well.

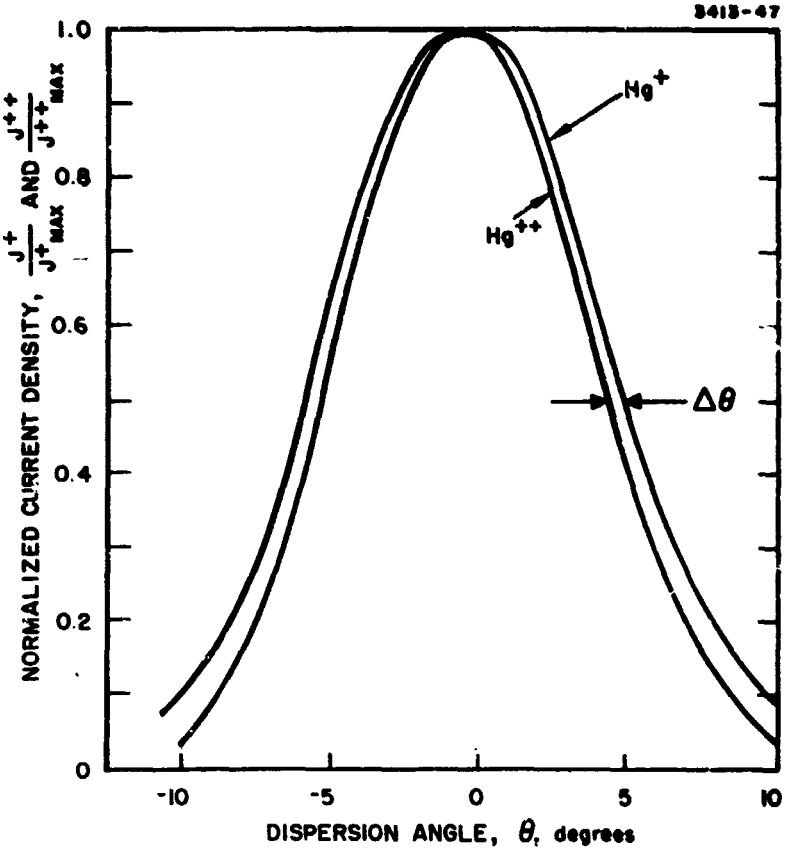

Fig. 35. Normalized current density profiles for experimental determination of $\Delta\theta$; r = 0.

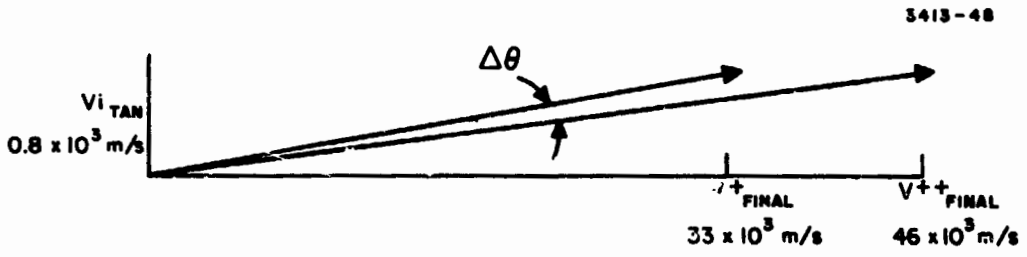

Fig. 36. Velocity diagram for determination of Δθ.

3. Additional Probe Data

In order to investigate the highest angle at which primary ions could be detected, a collimating total current probe was constructed. The probe was positioned to view a small area (≈4 accel holes) at the periphery of the grid, since it was felt that the highest divergence would occur at the plasma boundary. The probe could then be rotated about this point to a max of 90°. Figure 37 shows the probes angular relation to the thruster. Figure 38 shows an output trace of probe current versus angle for grid SN 650. As can be seen, a small amount of primary ion current can be detected to approximately 40 to 45° at which point it intercepts the ground screen. Although the ion current beyond approximately 20° has very little effect on the total thrust factor, it could have a damaging effect in terms of sputtering erosion of spacecraft surfaces unless accounted for in spacecraft design.

D. Summary

The dished grid ion optical systems evaluated during the Advanced Technology Program have proven to be extremely effective in the optimization of the EM thruster design. Because of their high structural stability, close electrode spacings could be maintained, thereby improving not only the system perveance but the discharge chamber efficiency as well. The reduction of the center-to-center spacing of the screen apertures has been shown to be an effective means of compensating dished grids to reduce thrust losses. Collimated probing techniques have verified the validity of the computed compensation curves, and have shown the thrust loss for properly compensated grids to be less than 1%.

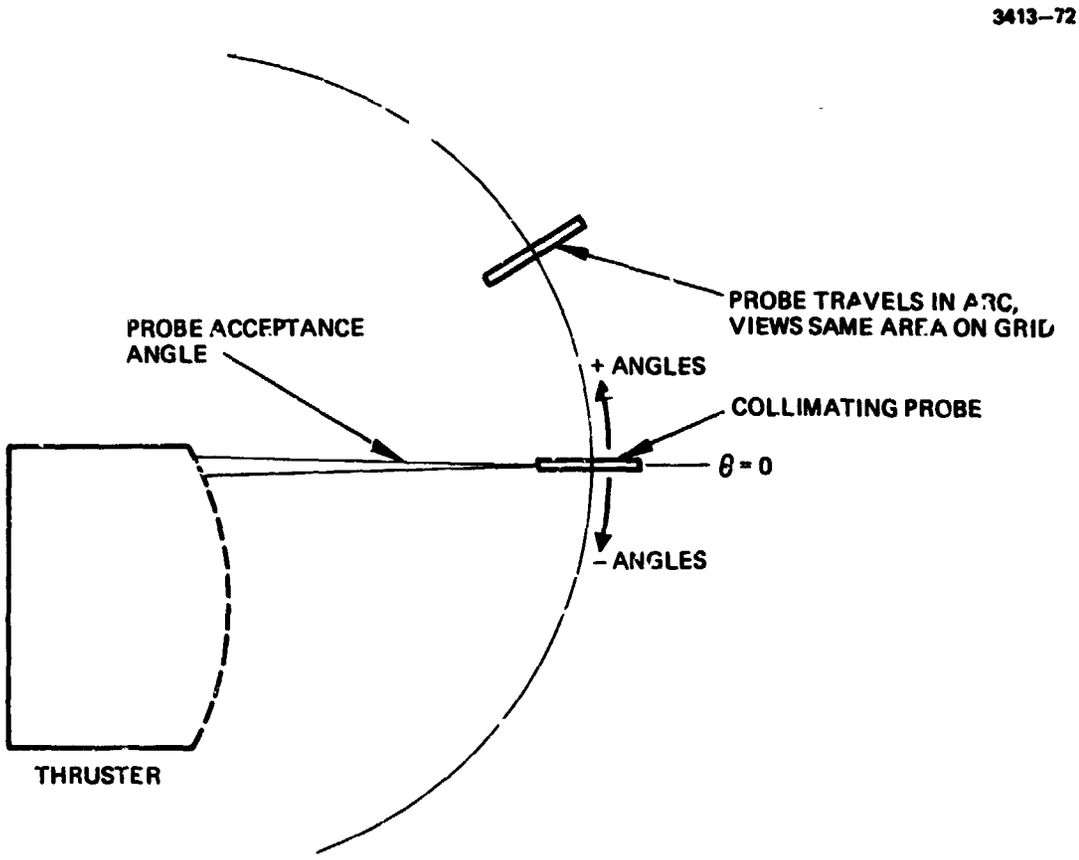

Fig. 37. Geometric configuration of collimating probe and thruster for measurement of high angle peripheral beamlet trajectories.

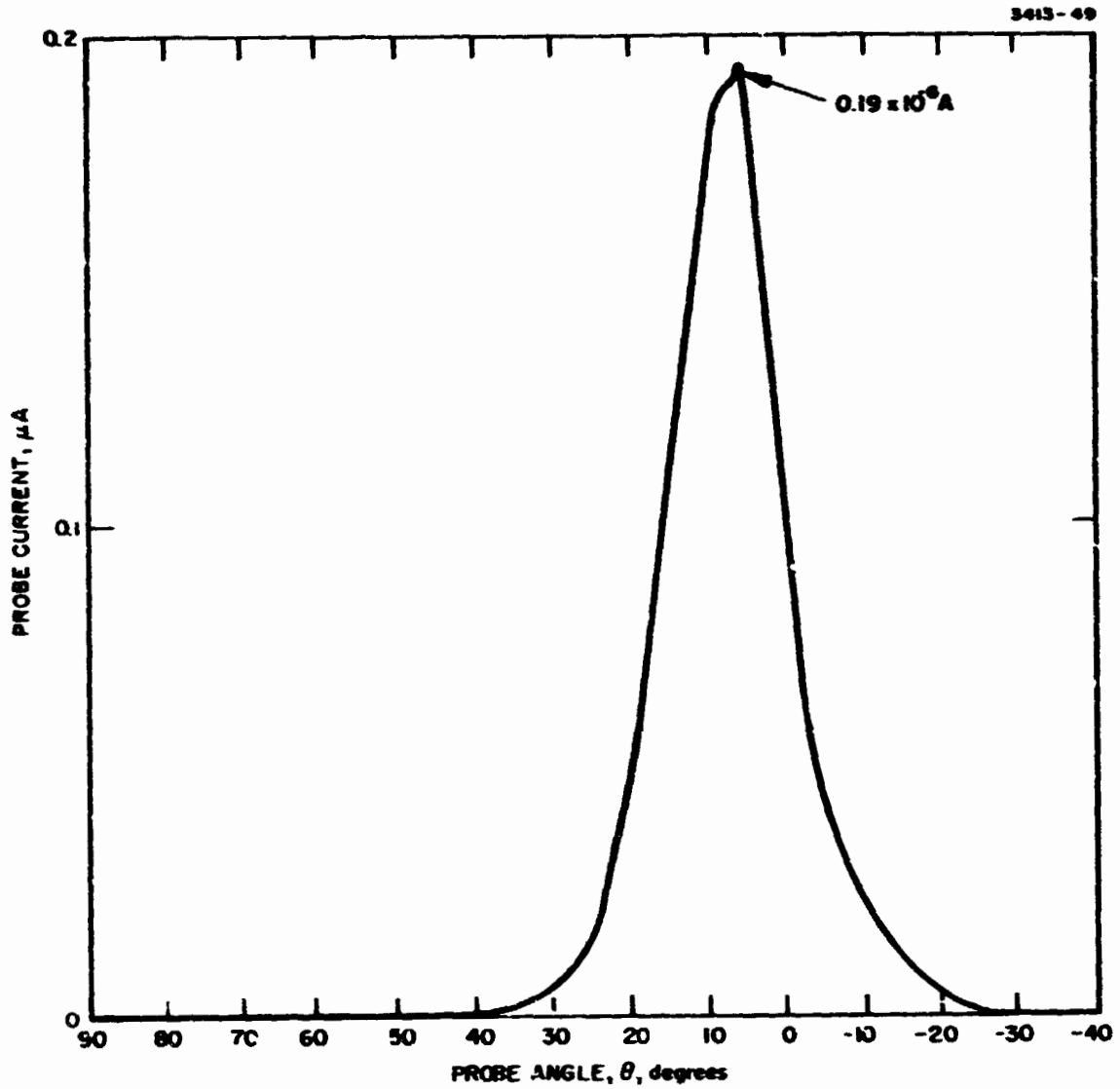

Fig. 38. Collimated probe current versus angle θ (Fig. 37).

C-7

IV. DOUBLE CHARGED ION MEASUREMENTS

Under the Advanced Technology Ion Thruster Program a comprehensive measurement of double charged ions in the beam of the 30-cm thruster was performed for the first time. At the outset of the program it was anticipated that the thrust losses due to multicharged ion content were small and that only minor correction factors would result. Such was not the case, however, as sequential ionization processes were found to be dominant. Thus, considerable effort was expended in order to evaluate the multicharged ion content and to compute the various loss factors associated with thrust and propellant utilization.

A. Measurement Technique

A collimated mass spectrometer probe, complete with articulating and positioning mechanism, was used to provide separation of different charge species in the extracted ion beam. The probe unit could be positioned across the thruster diameter to collect current components over a range of angles from $+40^{o}$ to -40^{o}. Samplings of single- and double-ion currents were collected from seven angular positions at each of four equally spaced radial locations. These data were then computer analyzed to provide current distributions in the plane of the accelerator grid, as well as the effective thrust and thrust loss factors for beam divergence and double-ion content. A more detailed description of the E x B analyzer and the method of data analysis is given in the Appendix. The following section will summarize the results of this probing technique as applied to multicharged ion evaluation.

B. Preliminary Probe Results

During the early stages of both probe and thruster development, a number of experiments were performed in order to more fully characterize the thruster ion beam, and to determine all factors which must be considered in arriving at absolute correction factors. It was

during this period that the interdependence of thruster stability and spectrometer output traces was resolved, whereby large fluctuations in the discharge chamber caused a degradation in the probe's separation capability. Outgassing of the probe was also investigated to ensure that no charge-exchange reactions were occurring within the collimating section. The advent of dished grid ion optical systems with associated compensation techniques added a degree of complexity to the probing system, and it was soon discovered that the angular distribution of both single and double ions must be examined. Interrelated with beam divergence due to grid curvature was the divergence due to aperture effects and accel-decel ratio which also encouraged the examination of the angular dependence for each ion species.

A strong radial dependence of multicharged ion ratios was suspected at the outset of the program and this was confirmed in subsequent tests where probe measurements of the ratio of double- to single-ion current were made at various thruster radial positions. Measurements of the ratio of single to double charged ion species were made in the plane of the probe as shown previously in Fig. 31. These measurements are converted to absolute current density values through use of the computerized data reduction technique, and a total current density distribution measured near the plane of the accelerator. Taking into account the angular dependence at each radial location, the double-to-single-ion current density ratio is plotted as a function of total current density and the results shown in Fig. 37. Not only is this ratio a strong function of the total current density (approximately proportional to the square of the total current density) but the ratio also increases with decreasing beam current at any given total current density. Since the lower values of total current density shown correspond to larger radii for the higher beam current values, this latter observation also supports the sequential ionization theory in that the ion density is known to decrease at larger radii, whereas, the neutral density variation with radius is thought to be relatively small. It is reasonable to assume that continuing to increase beam current would produce curves like those of Fig. 39 with approximately the same

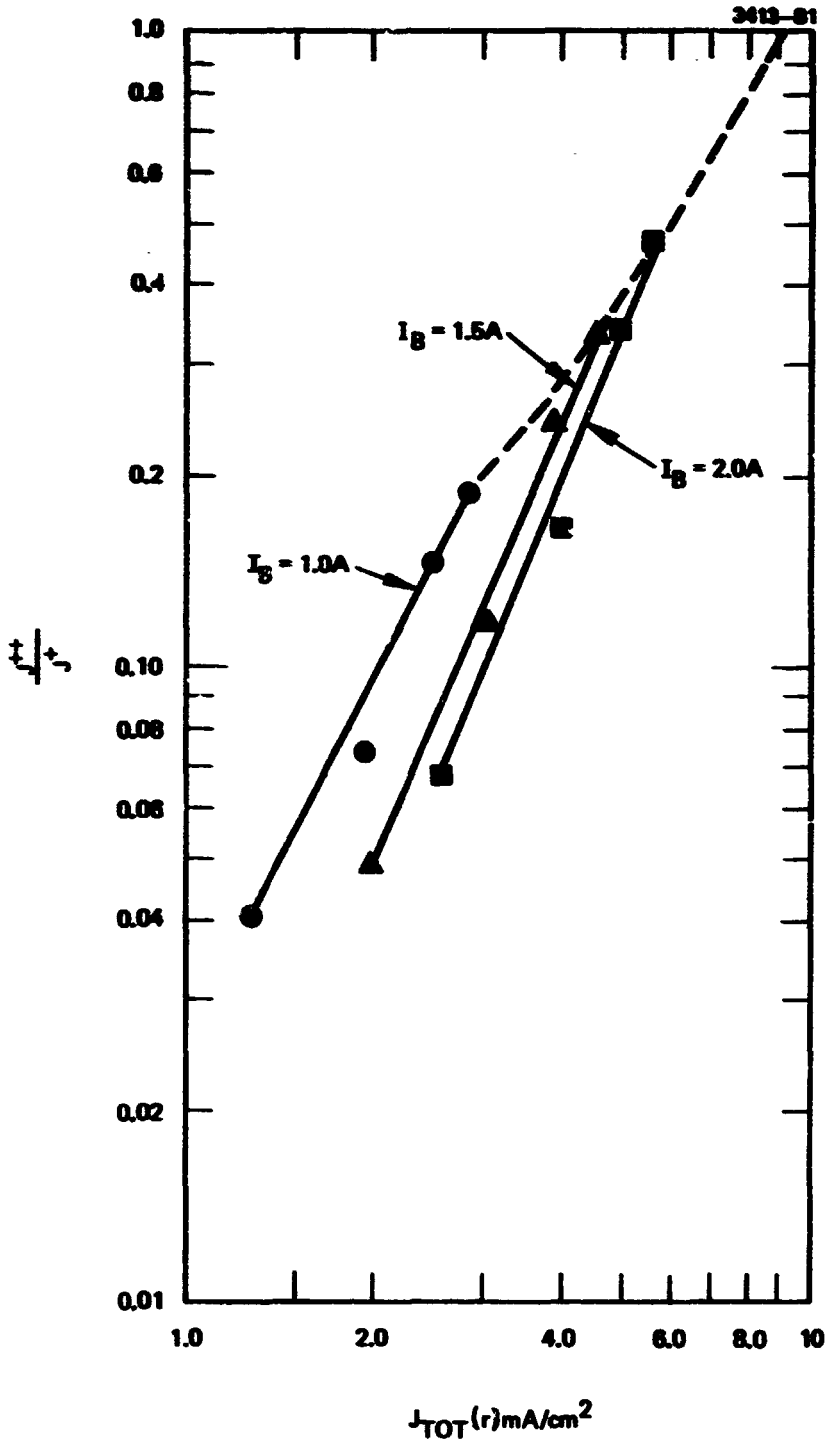

Fig. 39. Ratio of double to single ion current density as function of total ion current density with total beam current as a parameter.

slope, but shifted to slightly higher current densities. Extrapolating the maxima of the family of curves shown implies that the single and double ion currents become equal at approximately 9 mA/cm^2 total current density. Assuming that the relationship between maximum total current density and beam current is the same as indicated by Fig. 39, this current density corresponds to a beam current of approximately 3.2 A. The contribution of triply charged ions would also be expected to become significant under these circumstances, and would have to be accounted for as well.

Another experiment was performed to determine whether measurement of double ion ratios is influenced by the distance that the measurement is made downstream from the thruster. It was felt that if any ionization reactions occur in the beam it would be possible to determine the extent of such processes by collecting data at several axial as well as radial locations. The data in Table 15 show that the double-to single-charged ion ratio is independent of axial position and that the probe could be located at any desired downstream location consistent with collimator viewing area at the accelerator grid.

TABLE 15

Ratio of Double to Single Charged Ion Current As Function of Thruster Radius and Axial Position

Z (cm) \ R (cm)	12.7	10.2	7.6	5.1	2.5	0
45	0.053	0.105	0.185	0.260	0.305	0.344
27	0.046	0.098	0.185	0.250	0.313	0.350
14	0.053	0.098	0.193	0.250	0.310	0.350

T1340

One last experiment was undertaken to determine all of the ionization reactions which were taking place in the thruster discharge chamber and to evaluate the thresholds for these reactions before proceeding with the more complete double ion documentation. This was done while maintaining the probe position on the centerline of the thruster where maximum current ratios would be obtained. It was found that as discharge current was increased at fixed beam level and discharge voltage, the ratio of double-to single-ion current density approached a constant value. This was expected, since the thruster operates well above the "knee" of the discharge loss versus propellant utilization characteristics under this condition and the total ion density approaches a constant level. Thus, at a fixed beam current and with high discharge losses (230 to 240 eV/ion), the discharge voltage was varied over the range of stable operation. The results are shown in Fig. 40, where the threshold for the production of double-charged ions is extrapolated to a discharge voltage of approximately 23 V. Because the cathode plasma potential is about 5 to 10 V, the actual electron energy is considered to be 2 to 5 V less than the anode voltage. Thus, the extrapolated value is in good agreement with the known threshold of 19 V for sequential ionization from the single charged state. The agreement is also good for triple ionized mercury where the threshold for the production of triple-charged ions from the double ionic state was found to be approximately 33 V. Because of the slight shift in slope of the double ion curve, it was felt that ionization from the atomic state was occurring at potentials above 30 V. This is represented by the dashed line in Fig. 40. This contribution, however, was felt to be relatively small. Thus, the sequential ionization processes were confirmed as being the major contribution to multiple ion formation.

C. Thrust Loss Evaluation

During the preliminary testing, the discharge voltage and beam current were two parameters found to have the greatest influence on boththe production of double charged ions, and on the thruster propellant

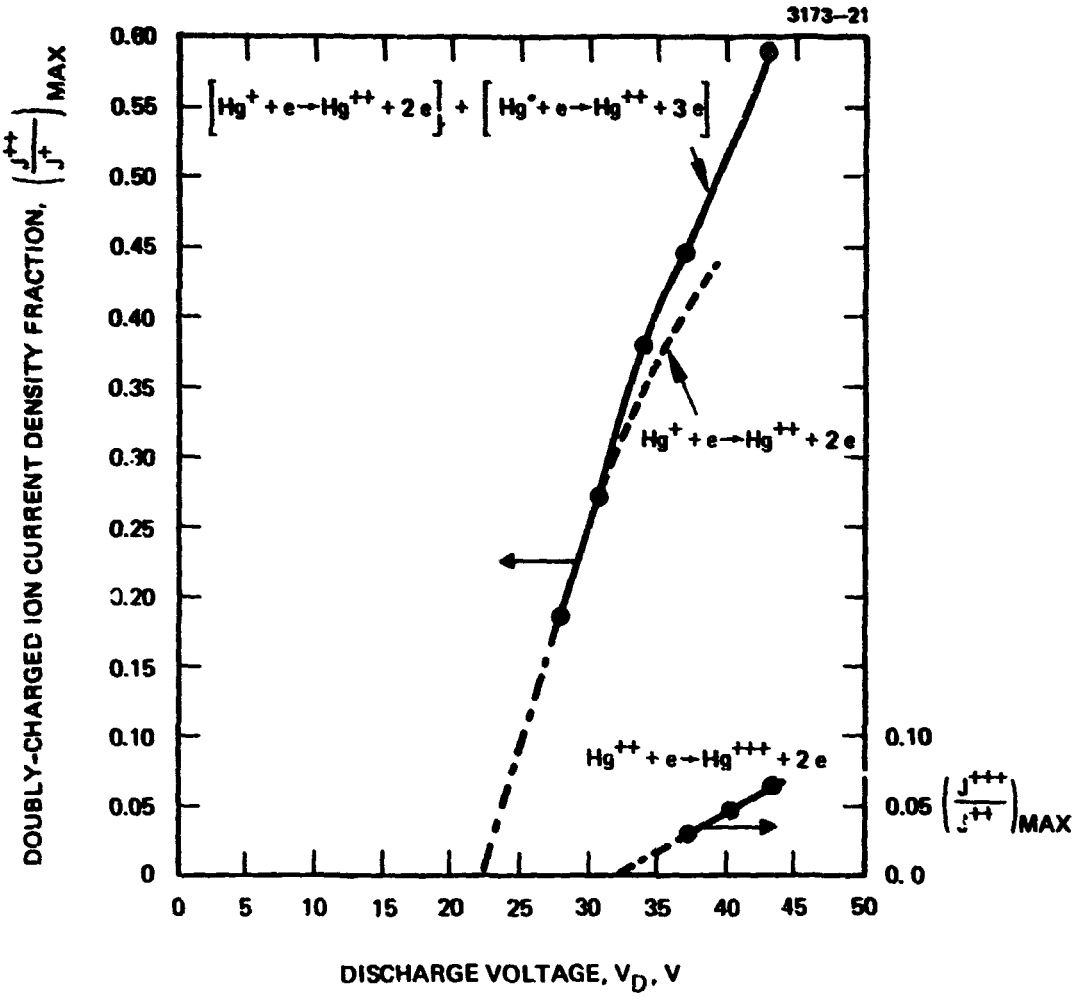

Fig. 40. Maximum multiple ion current density ratios in the Hughes 30-cm thruster.

efficiency. By operating at constant discharge loss (eV/ion), the variation of total thruster efficiency in terms of these two parameters could then be evaluated. Using the measurement technique discussed in Appendix A, the data for Fig. 41 was obtained, where the ratio of double to total ion current is plotted as a function of discharge voltage with beam current as parameter. The associated correction factors are listed in Table 16, along with the measured propellant efficiencies at each point, where α is the ratio of actual thrust to thrust computed from metered current and voltage, and β is the ratio of actual to measured propellant utilization (as defined in Section II). As can be seen, an increase in discharge voltage led to an increase in propellant efficiency, but also caused an increased double charged ion content. The parameter $\eta_u \alpha^2$ is directly proportional to the total thruster efficiency and is plotted as a function of discharge voltage, as shown in Fig. 42. Thus, the total efficiency approached a maximum value in the 40 to 41 V range, and above these voltages any further gains in propellant efficiencies were nullified by the double charged ion contribution. Also, at voltages greater than 40 V the triple charged ion contribution may become significant and is not considered in these curves.

The above data were obtained using thruster SN 403, which was a pre-EM thruster design, and optics set SN 644. In order to extend the evaluation to EM thruster designs, data was collected with thrusters SN 301-A and SN 301-B with the various optic sets mentioned in Section III. The results are shown in Table 17. The data is consistent with variations in propellant efficiency as well as with the data obtained with thruster SN 403. Thruster operation with grid set SN 656 (shallow dish) produced data which show a decrease in mass utilization and an associated reduction in double ion content. The reduction in double charged ion production, however, was not sufficient to result in a net increase in total thruster efficiency. On the other hand, operation with the decreased accel transmission grid set (NASA 35) showed a significant increase in propellant utilization without a proportional increase in multicharged ions. The net result was an increase in total thruster efficiency, and again demonstrated the type of unpredictable effects geometric changes, particularly in the ion optical system, can have on both thruster efficiency and thrust correction factors.

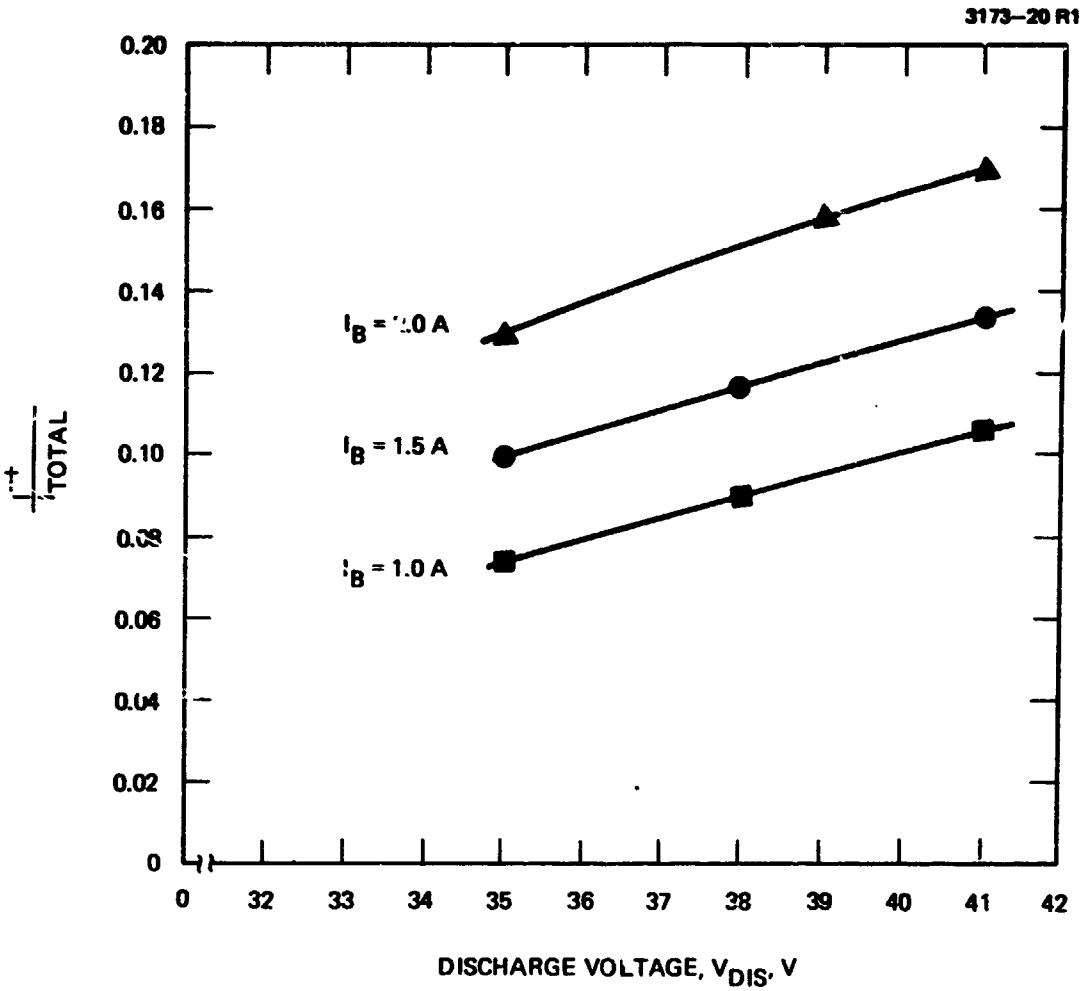

Fig. 41. Ratio of double to total ion current as a function of discharge voltage and beam current.

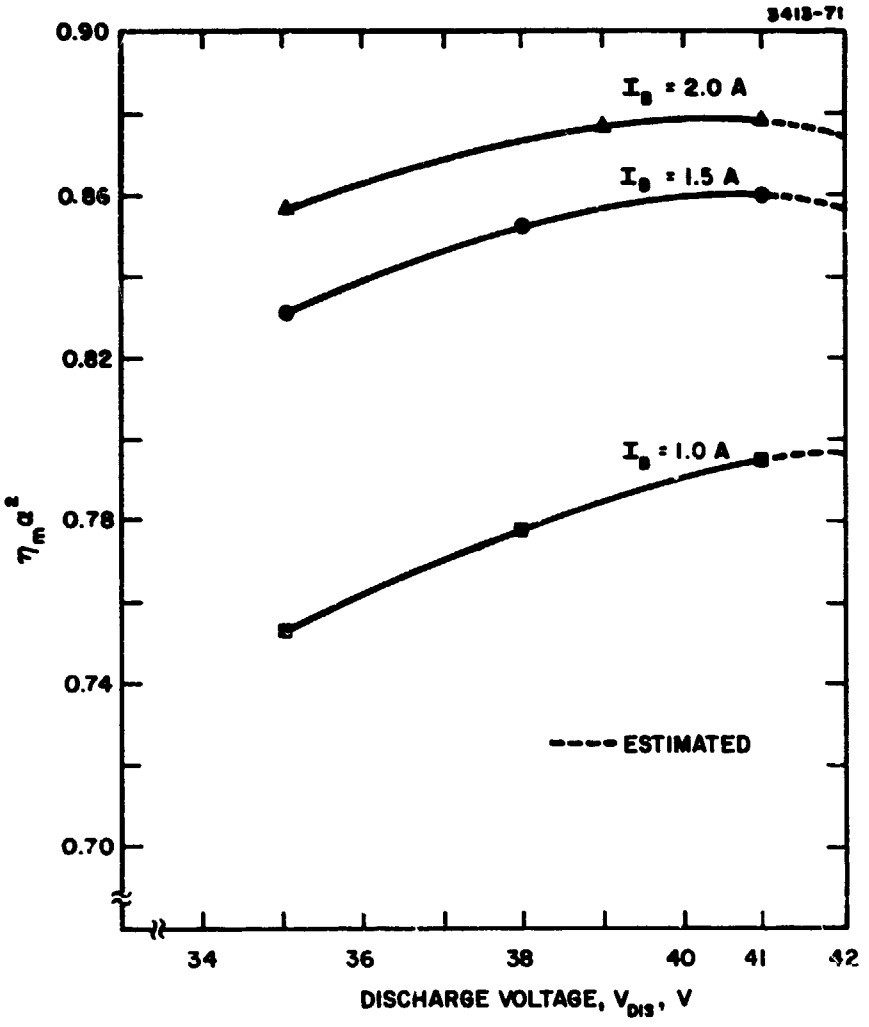

Fig. 42. Efficiency parameter as function of discharge voltage.

TABLE 16

Efficiency Factors

I_B, A	V_{DIS}, V	η_u	α	β	$\eta_u \alpha^2$
2.0	35	0.926	0.962	0.935	0.857
2.0	39	0.966	0.953	0.920	0.877
2.0	41	0.974	0.950	0.915	0.879
1.5	35	0.882	0.971	0.950	0.832
1.5	38	0.913	0.966	0.942	0.852
1.5	41	0.932	0.961	0.934	0.861
1.0	35	0.786	0.979	0.964	0.753
1.0	38	0.819	0.974	0.955	0.777
1.0	41	0.848	0.969	0.947	0.796

T1351

D. Discussion and Conclusions

The above testing served to identify a number of parameters which are dominant in affecting ionization processes in electron bombardment thrusters. The first and most obvious parameter is the ionization cross-section which is dependent on primary electron energy. Cross-section curves for the reactions indicated are shown in Fig. 43. These curves are approximations based on the Gryzinski analysis as well as experimental data, and correlate well with the data of Fig. 40. Thus, a reduction of double ion content could be accomplished by lowering the discharge voltage. However, this would also reduce the efficiency of producing single ions thus penalizing total thruster efficiency.

The second parameter of interest in the formation of double ions is the containment time. This is the time a particle of given charge state spends in the discharge plasma (also a measure of plasma

TABLE 17

Efficiency Factors at Constant V_{dis} = 37 V, eV/ion = 185

Thruster	Optics	I_B (H)	η_u	$\frac{I^{++}}{I_{tot}}$	α	β	$\eta_u \alpha^2$
301-A	644	2.0	0.95	0.145	0.958	0.928	0.871
		1.5	0.91	0.115	0.967	0.942	0.851
		1.0	0.81	0.062	0.981	0.969	0.779
301-B	650	2.0	0.955	0.15	0.956	0.925	0.864
		1.5	0.90	0.116	0.906	0.942	0.835
301-B	656	2.0	0.91	0.139	0.959	0.931	0.837
		1.5	0.87	0.099	0.971	0.951	0.820
301-B	NASA 35	2.0	0.99	0.166	0.951	0.917	0.895
		1.5	0.96	0.127	0.963	0.937	0.886

T1341

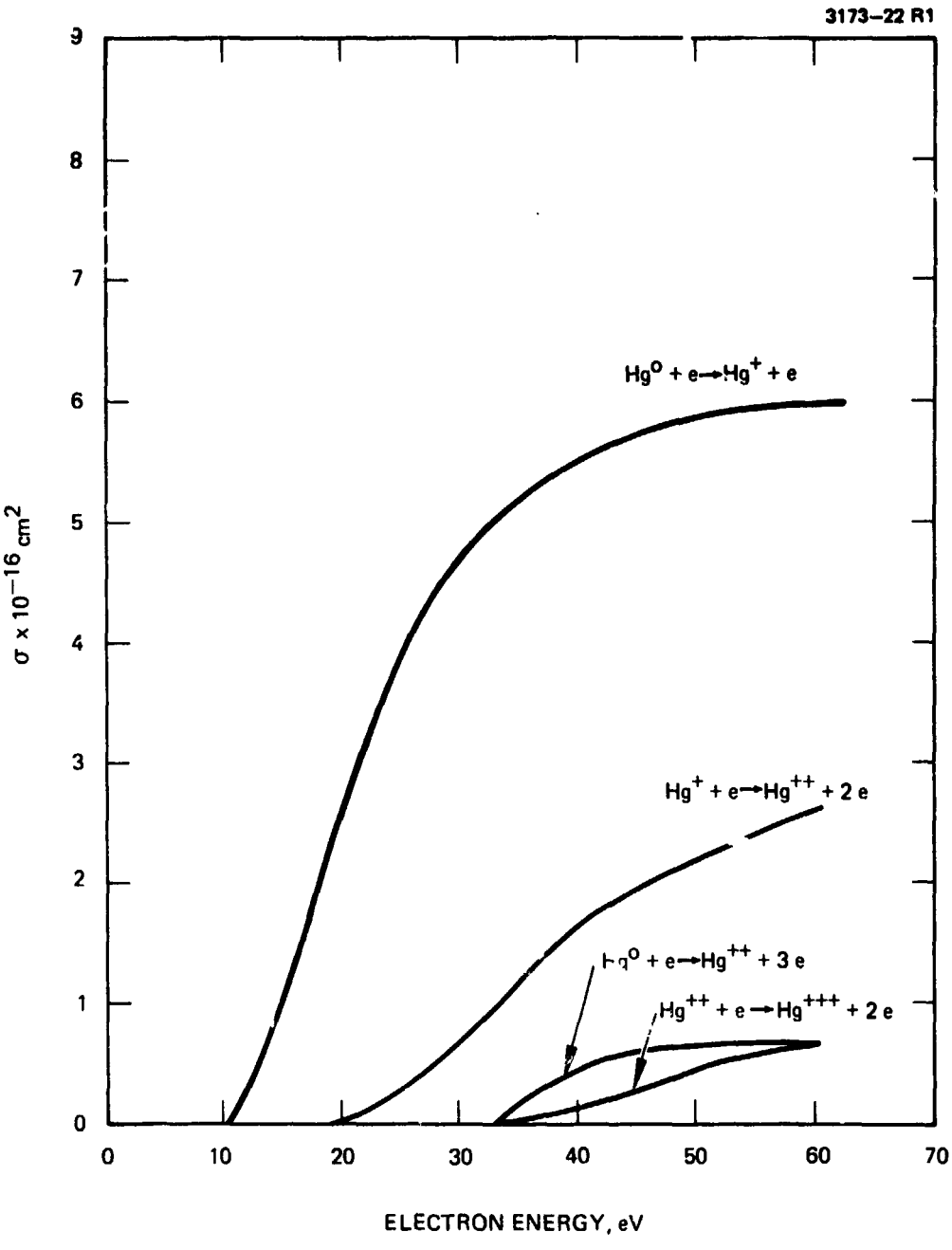

Fig. 43. Cross section curves for reactions shown.

volume to surface area). Examination of neutral particle residence time is found to be about 10^{-3} to 10^{-4} s based on the following assumptions:

- Neutral atoms have thermal velocity corresponding to temperature of discharge chamber walls
- Volume collisions are negligible
- Mean distance traveled from boundary to boundary is several centimeters.

Volume collisions do occur, however, and have been estimated[7] at 4×10^5/s for electron-atom interactions and 2×10^6/s for electron-ion interactions under typical discharge conditions. These collision frequencies are expected to vary with thruster geometry and operating conditions as do other parameters. However, if the ratio of electron-ion to electron-atom interactions remains unbalanced in this predominance, it can be seen that the double ionization becomes signifcant whenever the percentage of ionization is increased. Consequently, it appears that high propellant utilization and low double ionization are mutually exclusive unless a means can be found to remove ions from the discharge volume by way of the ion extraction system at a much higher rate than neutral atoms leave the thruster (by the same path). One such means has been demonstrated with the use of a grid system (NASA 35) where transmission for ions is very high while that for neutrals is low. This resulted in the improved thruster total efficiency as mentioned above.

A determination of electron, ion, and neutral particle densities is a third means of evaluating the multiple ion formation in 30-cm thrusters. In general, increases in electron or single ion densities or a reduction in neutral density tend to enhance the production of double-charged ions. For a fixed thruster configuration, operating parameters such as discharge voltage, discharge current, beam current, mass utilization, and accel-decel ratio are of prime importance. The effect of discharge voltage and beam current on the total double ion content was shown in Fig. 41. As discussed previously, both single

and double ionization cross sections are a function of discharge voltage leading to similar variations in the ion density distributions. Thus, a given thruster condition cannot be evaluated simply in terms of the double ion content, but must be evaluated in terms of single ion performance as well.

V. POWER CONDITIONER/THRUSTER INTERACTIONS

The primary goal of the power conditioner/thruster interaction investigation was to verify or modify the power conditioner and control specifications set forth under the earlier Low Voltage Thruster Program (NAS 3-14140) for operation of the EM thruster design. Most of this activity was carried out with the laboratory version of the EM thruster design as represented by thruster SN 301-A/B described in Section II. As discussed below, only a few minor variations in the power conditioning/control system were required to obtain satisfactory thruster operation under stable control over the full range of operation from cold start through full power operation. These specifications, verified here, and incorporated into the test console used in the endurance testing of the prototype EM thruster (SN 701) (Contract NAS 3-15523) have provided completely automatic control over the test including several emergency shutdowns and restarts initiated by test facility malfunctions.

This section also includes a brief discussion of discharge current oscillations and the observed effects on the power conditioner. While these oscillations have not been proven detrimental to thruster efficiency or other aspects of thruster performance, they are troublesome in achieving repeatable control characteristics and place mor stringent requirements on power conditioner regulation circuitry. Although the discharge chamber parameters responsible for the current oscillations have been somewhat narrowed down, and relatively low level oscillations have been achieved, no design modifications can be recommended at this time which will assure elimination or reduction of discharge current oscillations.

A. Power Conditioning System Description

The three-bay test console shown in Fig. 44 was developed to provide a portable power processing and control system for testing 30-cm thrusters. The major elements of the total system are the power processor unit, the thruster control system consisting of the

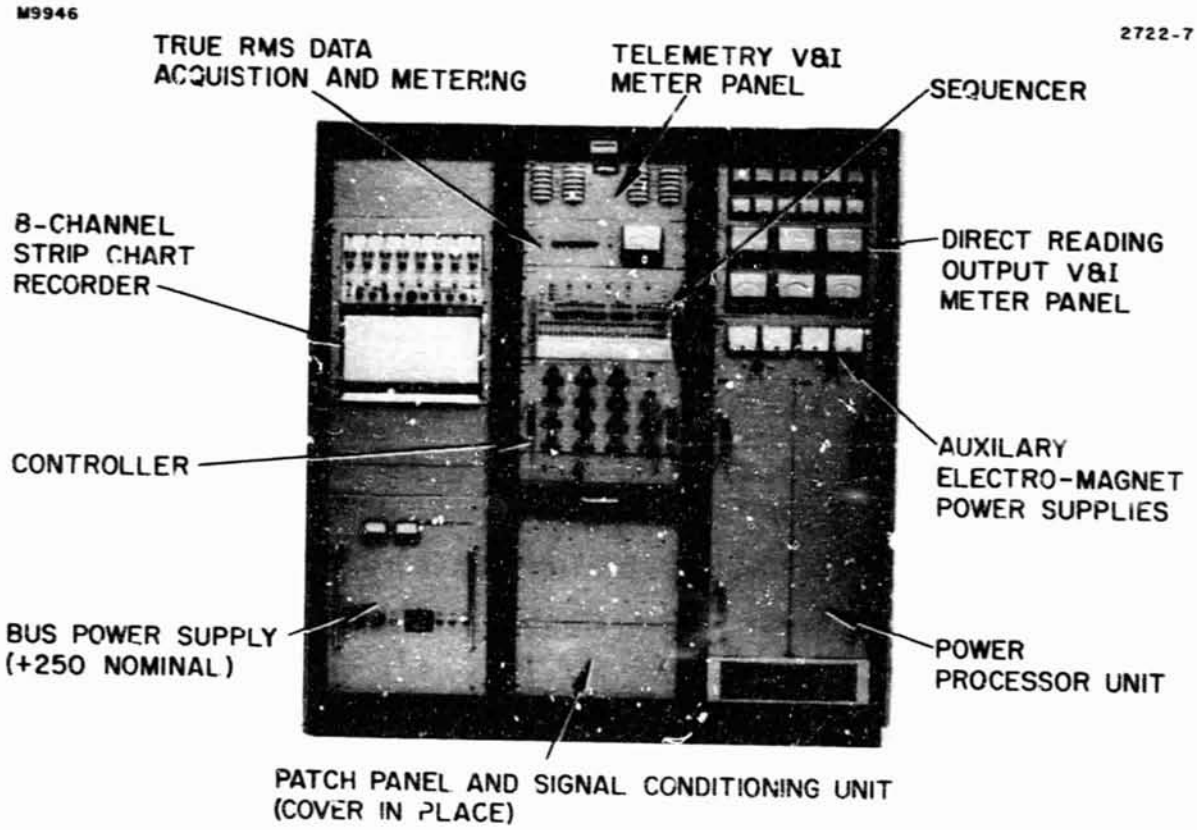

Fig. 44. 30 cm thruster power processor test console.

sequencer and controller, and the various units which comprise the instrumentation. A description of each of these elements is presented in the following subsections.

1. Power Processing Unit (PPU)

Prime propulsion thrusters as typified by the 30-cm ion thruster require between 10 and 12 sources of regulated voltage and current to achieve and maintain an operational run state. The power processing circuitry contained in the test console for powering such thrusters during their development and evaluation testing was implemented with flight-type circuit designs and is comprised of 11 supplies. Each is remotely programmable on either voltage or current over its full output power range with a 0 to 5 Vdc input signal. In addition, each provides 0 to 5 Vdc telemetry signals at system common which are proportional to the output voltage and current of the supply.

Table 18 lists the major design features of the supplies in the power processing unit.

2. Control System

The thruster control system may best be described by listing the tasks it is called upon to perform:

(1) Open-loop manual control of each supply

(2) Closed-loop control of selected supplies based upon voltage and current telemetry derived from the PPU

(3) Automatic high voltage overload detection and recycle circuitry as well as additional automatic corrective response capabilities

(4) Automatic thruster startup and shutdown capability

(5) Sufficient control capability to allow parametric studies to be carried out.

A simplified block diagram of the thruster control system is presented in Fig. 45. The interface between the control system and its load, i.e., the PPU/thruster combination is represented by the vertical dashed line at the right. With minor exception, all data

TABLE 18

Power Supply Specifications

Supply	Maximum Rating Continuous Operation	Regulation Mode and Accuracy	Mechanization Technique
Screen	1500 Vdc at 3 A	V, ± 1%	8-staggered phased pulse-width modulated 10 kHz inverters with series connected dc outputs to achieve full power
Accelerator	-2000 Vdc at 0.2 A	V, ± 2%	In-line switching regulator to establish input voltage to 10 kHz square wave output inverter
Discharge	50 Vdc at 20 A	I, ± 2% plus V limiting	3-pulsewidth modulated 10 kHz inverters with series connected ac outputs feeding final output rectification and filtering
Main vaporizer Cathode vaporizer Cathode heater Isolator heater Neutralizer vaporizer Neutralizer heater	20 Vac at 7 A	I, ± 3%	Magnetic amplifier pulsewidth modulated power control on primary of output transformer. All supply modules driven by single 5 kHz inverter
Cathode keeper Neutralizer keeper	60 Vdc at 1 A 60 Vdc at 2.5 A	I, ± 2%	

T1225

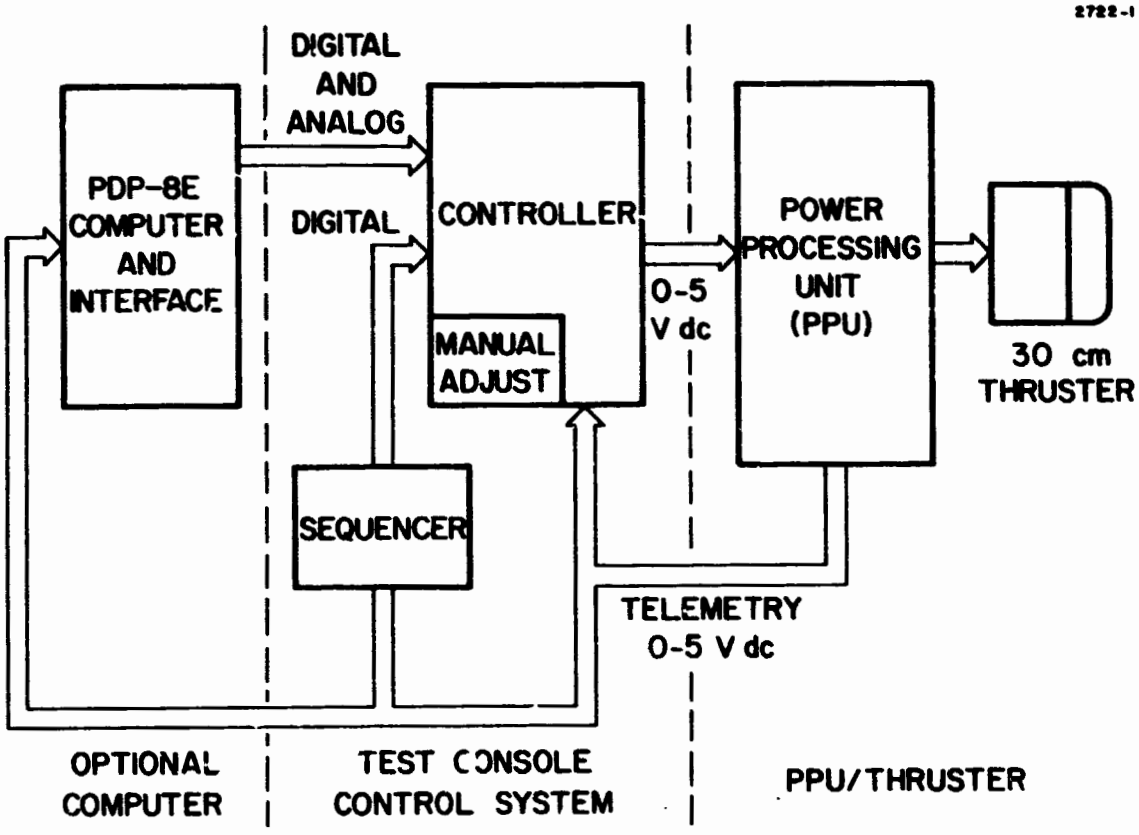

Fig. 45. Thruster control system.

traversing this interface do so in the form of 0 to 5 V analog signals. This highly standardized interface allows great flexibility in the choice of controller circuit configurations.

3. Controller

The controller is designed to stand alone and to be fully operational in the absence of any direction from either the sequencer or the computer. In this mode the controller performs the following functions:

(1) Open loop, manual control of the PPU on an individual supply basis

(2) Closed-loop control of the neutralizer, discharge voltage and beam current via the neutralizer vaporizer, cathode vaporizer, and main vaporizer supplies, respectively

(3) Automatic high voltage overload detection of the screen and accelerator supplies as well as automatic cutback and recycling of these and other supplies in the event of such an overload

(4) Standardized sequencer and computer interface capability.

4. Sequencer

Although the controller described in the previous section provides the necessary capability to operate the thruster during steady-state conditions, it lacks the ability to automatically direct the startup and shutdown of the ion engine. The startup procedure selected for implementing the sequencer is a five-segment command sequence which brings the thruster in stages from a cold start to a fully operational state. The shutdown selected is accomplished in only two steps and is intended to maintain uniform temperature distribution throughout the engine structure during cooling.

Although each sequence (startup or shutdown) is initiated only by means of an external command, the decision to advance from one stage to the next within a given sequence is based upon time and telemetry information.

5. Instrumentation

The instrumentation included as an integral part of the test console is varied and reasonably extensive. Instrumentation for monitoring the various dc output voltages and current of the power processor just prior to routing the power to the thruster is located in the right-hand bay directly above the power processing unit. The voltages and currents of the discharge, accelerator, and screen supplies are monitored with calibrated 5 in. ±1% mirrored scale meters. Other dc parameters, cathode and neutralizer keeper voltages and currents, neutralizer coupling voltage, neutralizer emission current. and the current between the power processor common and facility ground are measured with 2 in. ±3% meters. All of the above metering is assembled into the form of a meter panel in which the meters are submounted because of the high voltages behind plexiglass for operator safety.

A 16-channel true rms data acquisition system is employed for monitoring the 5 kHz pulsewidth modulated square wave outputs of the six heater/vaporizer supplies. The data signal inputs to the rms Data System are derived from isolated voltage and current instrumentation transformers located at the power output leads of the individual supply modules. The heater current or voltage to be monitored is selected by a multipole pushbutton switch on the front panel of the instrument, or by an external binary code 4-bit word. Each channel has an attenuator pad to scale the incoming ac signal for calibrating the rms conversion. The output of the rms converter is routed to a 5 in. ±1% mirrored scale meter for manual data collection by an operator. An additional buffered output is provided for remote readout when collecting data under computer control.

B. Control Specifications for EM Thruster

1. Steady State Beam Current, Discharge Voltage and Neutralizer Control Loops

The steady-state control loops implemented in the HRL 3 Bay power conditioning system are, with minor exceptions, very

similar to those employed in the earlier model power conditioning system used in the Low Voltage 30-cm Ion Thruster program NAS 3-14140. In particular the beam current controller and discharge voltage controller are, except for minor scaling changes to allow operation at higher beam current, almost identical and the reader is referred to this earlier report for detailed descriptions of these subsystems. As previously described, stable beam current is maintained by proportional control of the main vaporizer power supply using an error signal obtained by comparing sensed beam current with a beam reference signal. Stable discharge voltage is maintained by proportional control of the cathode vaporizer supply using an error signal obtained by comparing sensed discharge voltage with a discharge voltage reference signal.

The operation of the neutralizer is somewhat different than before, since the neutralizer heater is now separated from the neutralizer vaporizer heater. An additional heater supply, having identical power capability as the other five heater supplies, has been included to operate the neutralizer cathode heater and is not part of the proportional control loop. Otherwise, the neutralizer control loop is virtually the same as before. Neutralizer keeper voltage, V_{NK}, is the only quantity available for control of the neutralizer vaporizer and coupling of neutralizer electrons into the beams. As before, neutralizer keeper voltage is maintained by proportional control of the neutralizer vaporizer supply using an error signal obtained by comparing sensed V_{NK} with a preset voltage reference signal. Each of the three control loops has a trimpot for adjusting maximum loop limit level to prevent or minimize the tendency for the thruster to reach unstable portions of thruster transfer characteristics.

Analytical determinations of the accuracy, response and stability of these three control loops cannot be made without the detailed knowledge of small and large signal thruster transfer characteristics and their functional dependence on many thruster operational parameters. Measurement of these transfer characteristics was not attempted under this program.

The control loop configurations and transfer gains of those elements in the power conditioning have been empirically determined to give the best overall results in terms of propellant and electrical efficiencies and smooth, reliable operation in experience gained over several thousand hours of thruster operation.

2. Thruster Start Up and Shutdown Sequence

As mentioned previously, the HRL PPU console has implemented within it a fully automatic startup sequencer, which allows reliable cold thruster startup to a stable run level based on time and telemetry information. A sequential flow diagram, together with the various supply warm up and run level setpoints, is shown in Fig. 46. The supply current and voltage values corresponding to the various setpoints are shown in Table 19. The sequencer provides for manual override of automatic stateword selection to any other desired state or manual hold of a given state for an arbitrary period of time. In addition, the sequencer provides for thruster fault recovery in the event of a keeper or discharge ignition loss, as shown on the flow diagram. High voltage overload recycling is accomplished in other circuitry and will be discussed separately.

A typical time progression of events from cold start initiation to steady state closed loop run level is depicted in Fig. 47.

The sequencer also provides for ordered thruster shutdown to maintain uniform thruster cooling. This sequence was not evaluated with the EM thruster design.

3. High Voltage Overload Recovery

Additional circuitry has been included in the control system to provide recycling from high voltage overload. A typical time profile of high voltage recycle events is shown in Fig. 48. Improvements which have been incorporated in the overload recycle (OLRC) implementation include:

- Raising of cathode keeper current setpoint until high voltage has been restored

TABLE 19

Setpoint Chart

	Off	SP1	SP2	SP3
Main Vaporizer	0A	1.0A	0.8A	0.3A
Cathode Vaporizer	0A	1.5A	-	-
Neutralizer Vaporizer	0A	1.5A	-	-
Accelerator	0V	-500V		
Screen	0V	1100V	-	-
Main Isolator	0A	1.9A	-	-
Cathode Isolator	← outboard variable supply →			
Discharge	0A	10A	0.75A	-
Cathode Heater	0A	4.4A	-	-
Neutralizer Heater	0A	5.0A	-	-
Cathode Keeper	0A	0.5A	0.8A	-
Neutralizer Keeper	0A	1.3A	-	3.0A
Magnetic Baffle	← outboard variable supply →			

T1352

- Raising of neutralizer keeper current setpoint until high voltage has been restored
- Maintaining the discharge-cathode vaporizer loop active during recycle while changing the loop reference setpoint.

It was found to be desirable to raise the keeper currents during a trip and OLRC to prevent loss of keeper ignition. Although there is no undisputable explanation for it, this technique effectively eliminates keeper outages which were frequent without it.

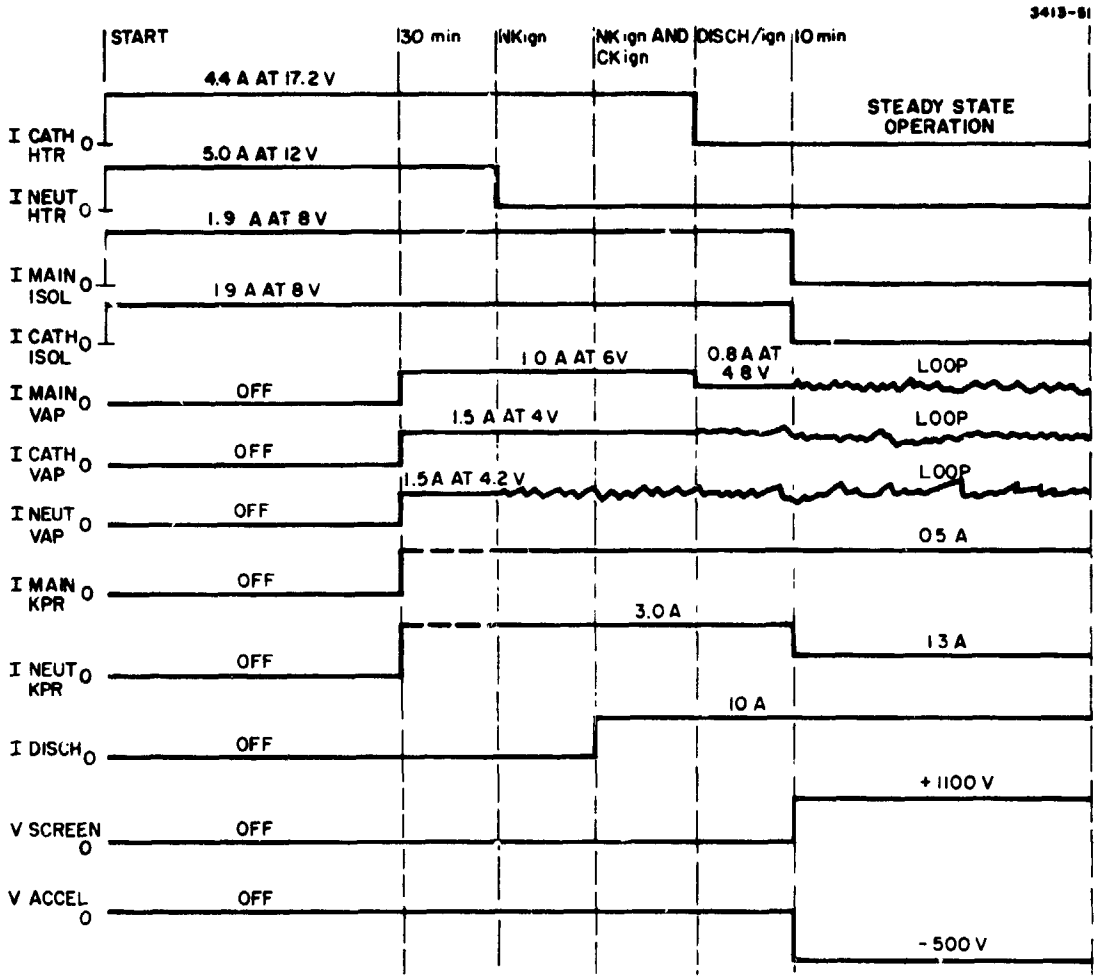

Fig. 46. Start up sequence.

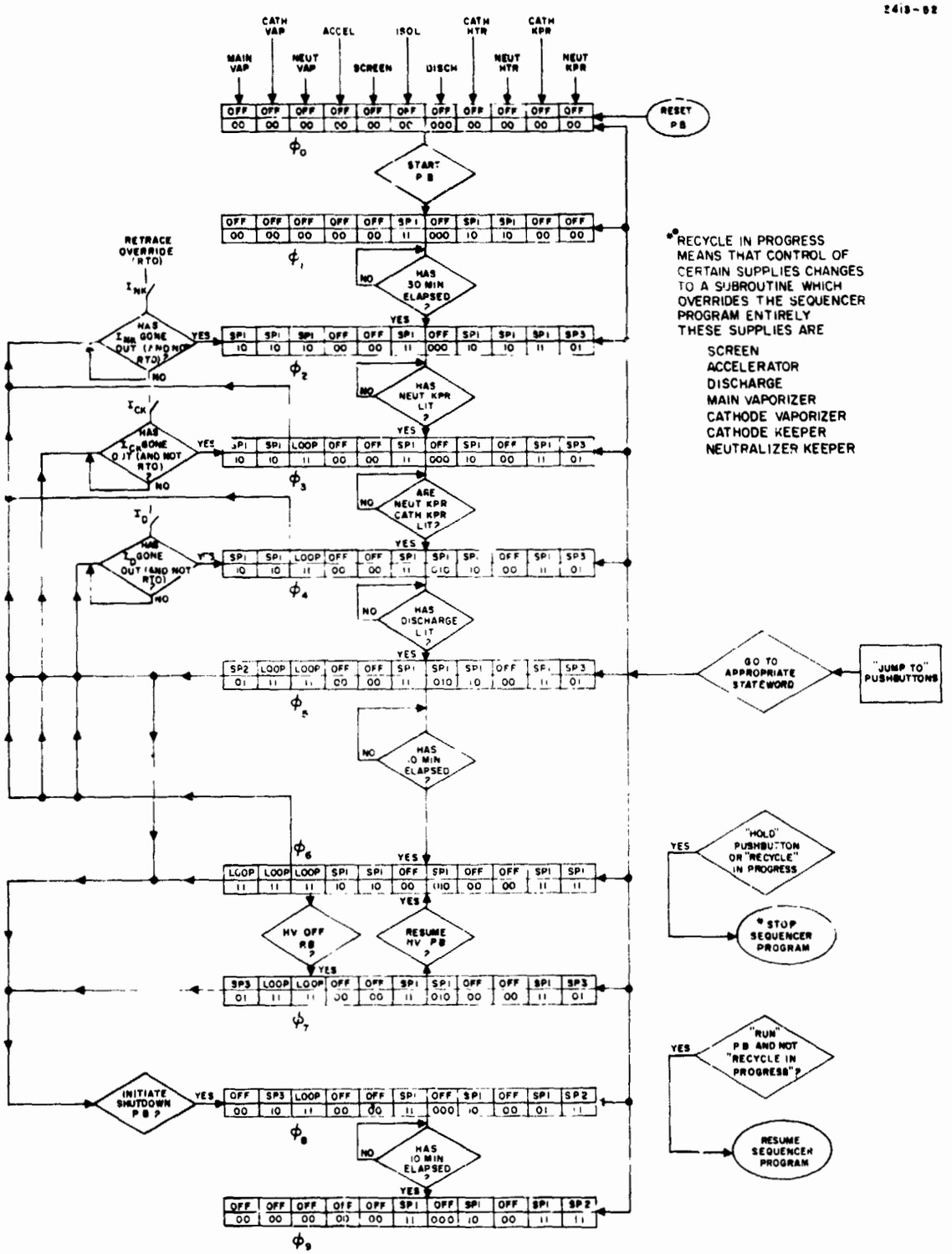

Fig. 47. Hughes Research Laboratories 3-bay console sequencer stateword transitions.

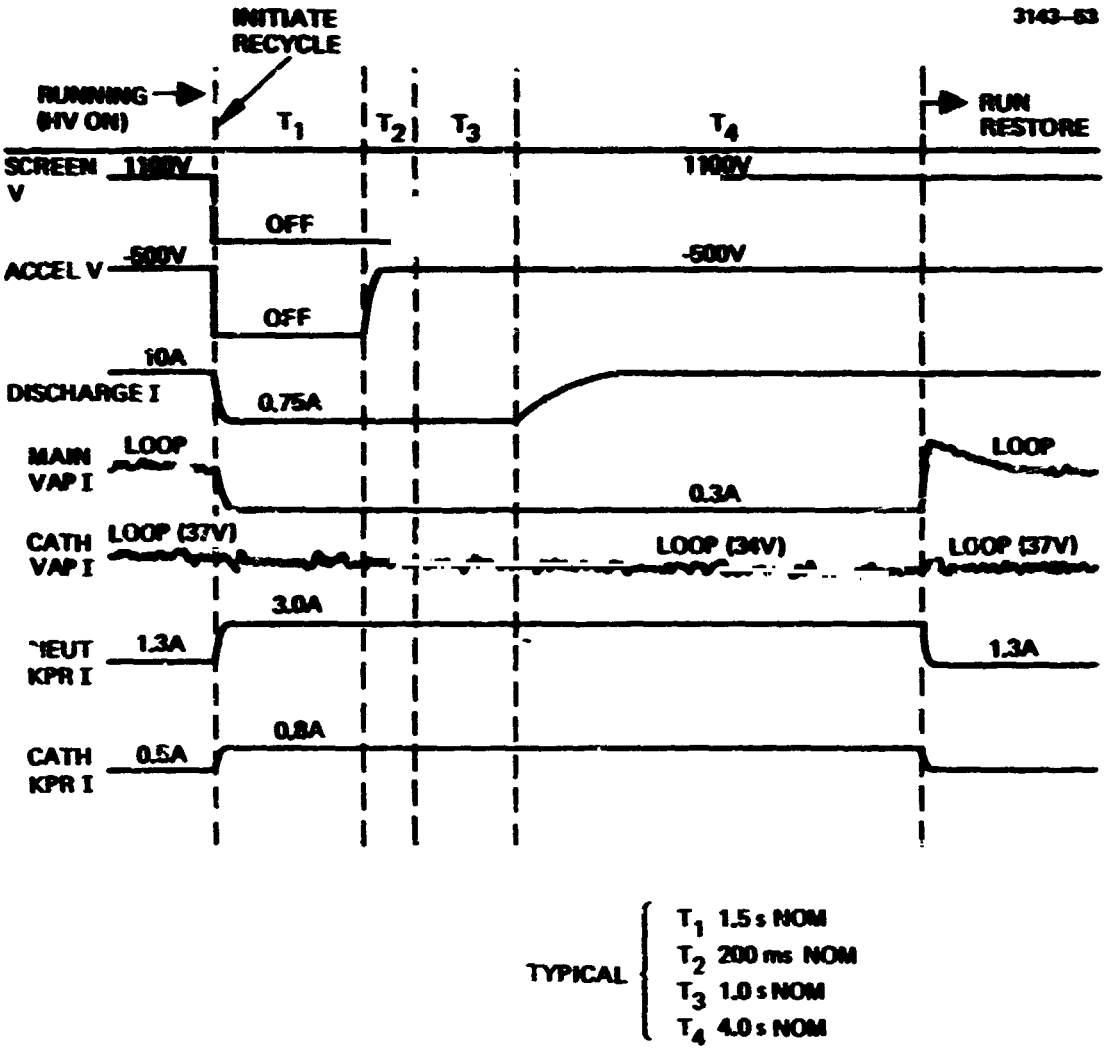

Fig. 48. High voltage recycle voltage versus time.

The discharge voltage OLRC configuration was chosen to minimize or eliminate discharge voltage overshoot which occurred on high voltage reapplication. Since the discharge impedance is lower under beam off conditions, this particular implementation makes flow control during OLRC more precise so that the discharge impedance preceding high voltage application will be the same as the steady-state run level.

C. Discharge Oscillations – Cause and Effect

Severe modulation of the discharge current had been observed early in the program during operation of the radial hybrid magnetic field discharge chamber. The modulation was primarily an oscillation in discharge current at a frequency of about 850 Hz. This oscillatory behavior was attributed to excessive magnetic field strength in the "baffle gap" which isolates the cathode and main discharge plasmas. Its principal effect was modulation of the ion beam and adverse interaction with thruster control loops. At this frequency, control loop error signals were continuously driving the power conditioning to respond to the oscillating discharge voltage, beam current, and neutralizer keeper voltage. As a consequence the oscillation was also manifested as a relatively large oscillation in current supplied by the dc power supply which simulates the solar panel bus. This factor, as much as any, resulted in discontinuing the development on the radial hybrid discharge chamber geometry.

Early in the development of the diverging magnetic geometry discharge chamber, a frequency spectrum analysis of all thruster currents was made and no oscillatory behavior was observed. As in the detection of the oscillation in the radial hybrid geometry, a secondary symptom first disclosed the presence of a discharge current oscillation under this program. During a routine power processor checkout, a relatively high number of high voltage recycles were experienced without any evidence of breakdown in the grid system. Observation of discharge voltage and current waveforms produced oscillographs like those shown in Fig. 49. While it is difficult to discern in the oscillographs

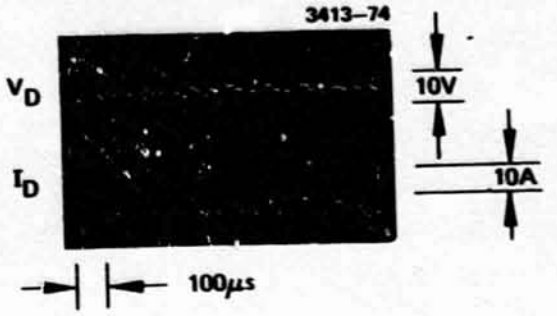

a) MAGNETIC BAFFLE CURRENT 5A

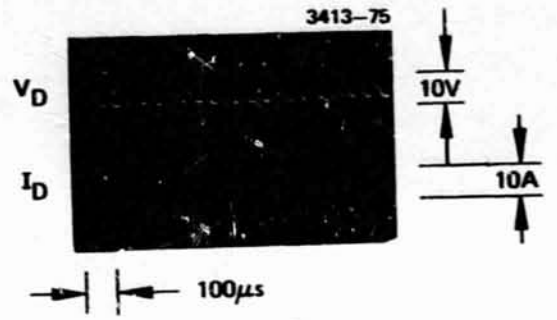

b) MAGNETIC BAFFLE CURRENT 7A

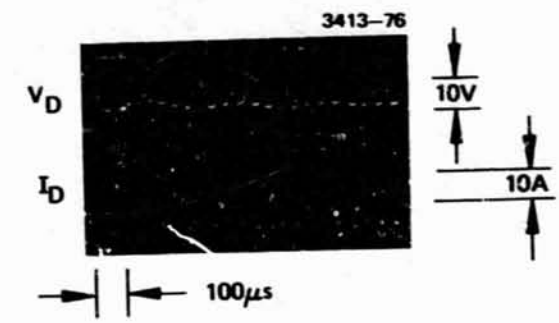

c) MAGNETIC BAFFLE CURRENT 10A

Fig. 49. Comparison of oscilloscope waveforms of discharge voltage and current for thruster operation at 1.5 A beam current, 37 V discharge voltage and 7.5 A (average) discharge current (thruster 701A).

shown, the discharge voltage and current waveforms are shifted in phase and the oscillation has relatively repetitive behavior at a frequency of 22 to 23 kHz. In Fig. V-6 (a), the oscillation in discharge current varies between 6 A and 14 A with an average value of 7.5 A (which the meters indicate). As magnetic baffle current is increased, oscillation frequency and amplitude increase (see Fig. 49 (b) and (c)). Under certain conditions, current supplied by the discharge supply (including beam current) can exceed the overload level of 20 A on extreme peak values, initiating an overload recycle. Although complete elimination of this type of oscillatory behavior would be preferable, oscillations may be fundamental to efficient operation of hollow cathode thrusters of this general design and, therefore, maintaining the amplitude and frequency in a tolerable range may be a necessary compromise.

Although control loops are not seriously perturbed by this type of oscillation, the set point reference values which provide control loop error signals seem to require readjustment periodically to maintain the reference quantities under control. Discharge voltage seems most affected, and neutralizer keeper voltage seems least affected. This behavior is thought to result from variations in the oscillation waveform, both with time and from thruster to thruster. Figure 50 shows an example of the oscillation waveforms for another thruster of the same generic design. Since the control circuitry senses an error signal continuously, in proportion to the waveforms shown, the control loop response results in some form of averaging as a result of vaporizer thermal response.

These are the only detrimental effects which have been attributed to the discharge current oscillations. No deterioration in electrical or propellant efficiency has been related to these oscillations, nor has double-charged ion production been found to increase signifcantly as a result of the corresponding discharge voltage oscillation. Near the close of this program, and continuing under Hughes internal research and development program, discharge parameters responsible for these current oscillations have been explored. Figure 51 shows modifications to the experimental thruster which facilitate variations in the cathode pole piece and baffle support geometry. A number of thruster

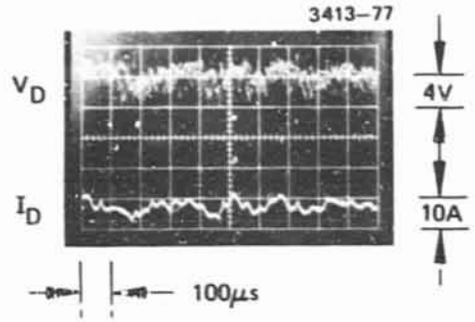

a) MAGNETIC BAFFLE CURRENT 5A

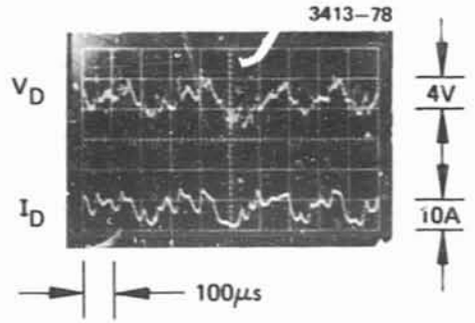

b) MAGNETIC BAFFLE CURRENT 7A

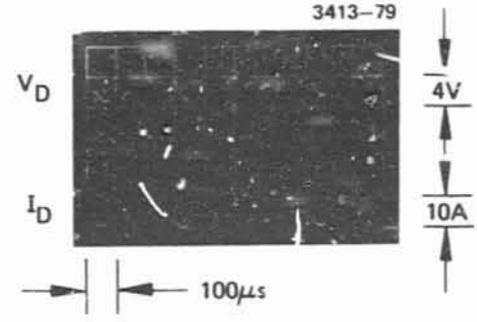

c) MAGNETIC BAFFLE CURRENT 10A

Fig. 50. Comparison of oscilloscope waveforms of discharge voltage and current for thruster operation at 1.5 A beam current, 37 V discharge voltage and 7.5 A (average) discharge current (thruster 701A).

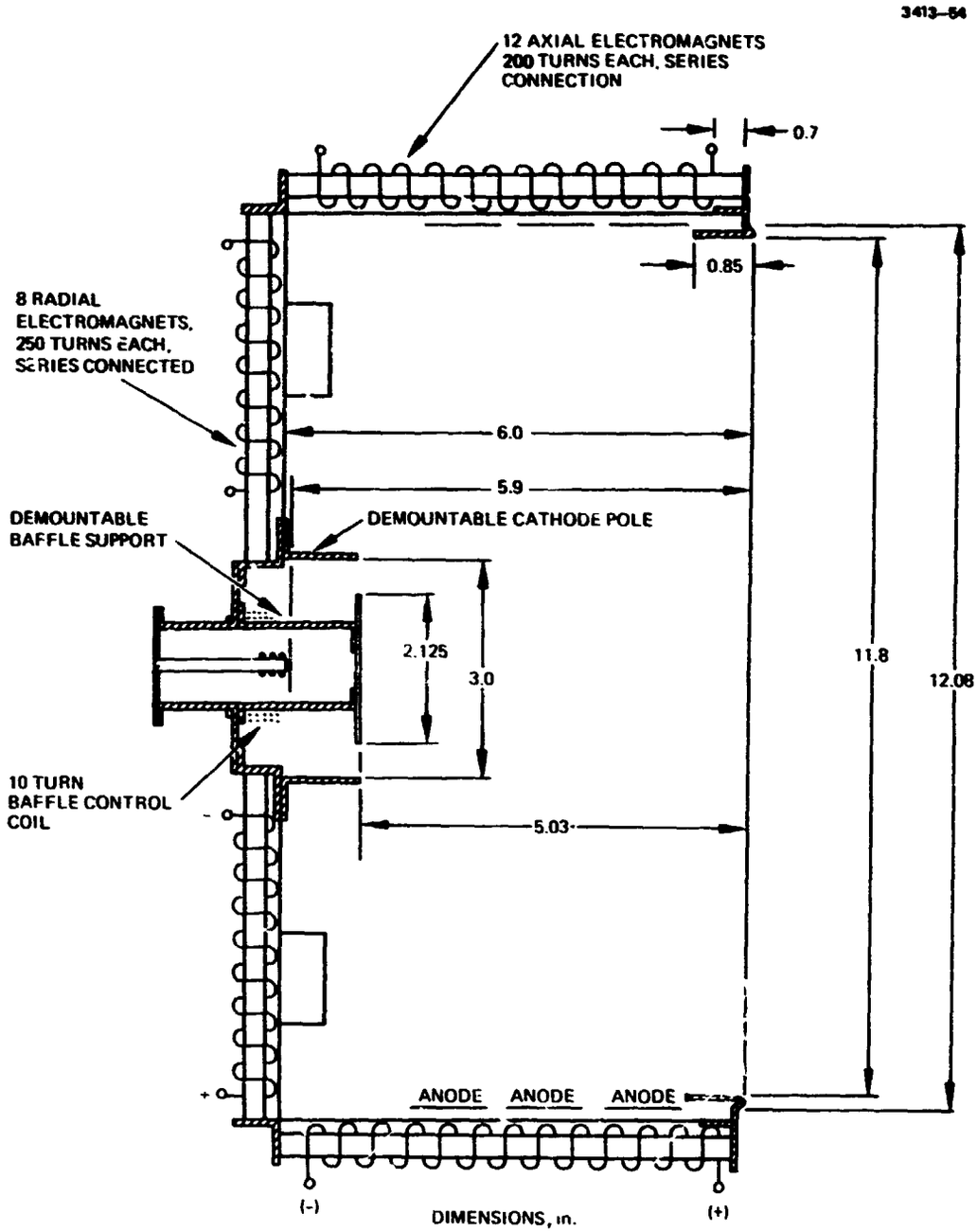

Fig. 51. Schematic drawing of versatile electromagnet thruster configuration.

variations have been evaluated which produce changes in the frequency and amplitude of the discharge current oscillations, but a modification to completely eliminate them has not been found. For instance, replacement of the magnetic baffle support and control coil with a nonmagnetic baffle of the type used in early thrusters reduces the amplitude of oscillation somewhat and shifts the frequency to the 40 to 50 kHz range. Installation of a magnetic baffle geometry with only two baffle support posts (instead of four) has little if any effect on the oscillation amplitude, but modifies the waveshape considerably and reduces the oscillation frequency to the 7 to 14 kHz range.

Closer examination of the magnetic field in the vicinity of the cathode orifice disclosed that an unanticipated axial field strength of 10 G exists in the cathode region of the magnetic geometry (EM thruster design) having the short cathode pole piece (2.54 cm long). Installation of the longer cathode pole piece formerly used (5.1 cm) reduces the magnetic field at the cathode orifice. Initial thruster operation with this pole piece resulted in the discovery of a discharge mode with relatively small oscillations in discharge current. As seen in the current waveform shown in Fig. 52, the discharge current oscillation amplitude is reduced to approximately ±0.5 A on a 10.5 A average, and the frequency shifted to the 40 to 50 kHz range. Unfortunately, operation in this mode of low oscillation was possible for only a very small range of thruster parameters. It is an indication, however, that efficient discharge operation can be achieved without large amplitude oscillation. The configuration for providing this type of operation over the entire thruster operating range remains to be discovered.

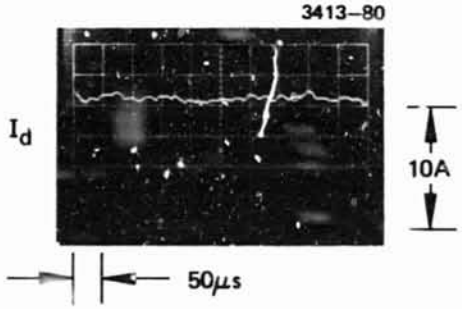

Fig. 52.
Discharge current waveform obtained with 5.1 cm pole price and baffle support.

VI. THRUSTER COMPONENT TECHNOLOGY

Development of component technology was not originally included among the goals for this program; however, it became necessary to participate in some component development to fully evaluate the EM thruster design. This consisted primarily of initial testing of new component designs with modifications when necessary. In some instances several iterations on new component designs were required to obtain satisfactory thruster operation. The discussion here is restricted to final component configurations and successful fabrication or assembly techniques evaluated under this program.

A. Ion Optical Systems

Description and specifications of the ion optical systems developed are discussed in Section III. The discussion here relates to fabrication and assembly techniques which were found essential to successful thruster operation with the dished grid ion optical system. Most of these findings have been incorporated in the assembly procedures generated under the EM thruster program.

1. Initial Assembly of Electrodes

Foremost in the initial assembly of the dished grid ion optical system is the achievement of conformal surfaces over the active portion of the accelerator system (grids should be in good contact when placed together without spacers). Secondly, both electrodes should be free of internal stresses and the peripheral flat areas should be planar so that good contact is made when the electrode is placed on a surface plate. If these conditions are met, it should be possible to assemble the electrodes on the mounting system shown in Section III with good alignment, grid-to-grid spacing, and thermal stability. These conditions cannot always be achieved, even with several attempts

at stress relieving; in this case, the completion of a useful assembly is improbable.

The next critical step is the attachment of the stiffening rings to the electrodes which must be accomplished without distorting them or building in internal stresses. This has been done successfully by furnace brazing in a rigid support structure or by fastening with 0-80 screws. The latter technique was preferred for assemblies used exclusively under this program, because it is faster and has less risk involved. (The success of furnace brazing an assembly of this size requires careful control over a number of conditions.)

2. Preparation of the Mounting Structure

Having successfully assembled the electrodes, the next requirement is to adjust the support ring to provide planar surfaces for mounting. In principle this is accomplished by the rigid tubular structure, however a significant amount of adjustment of the screen grid brackets and accel insulators is necessary to obtain the support structure in correct alignment. No infallible technique was found to insure accurate assembly of the tubular support ring and electrode mounting brackets, and an alternative has been developed under internal programs and tested briefly near the close of this program. This mounting structure and the complete grid system assembly are shown in Figs. 53 and 54. Further evaluation is required; however, this mounting promises to eliminate much of the uncertainty experienced in obtaining plane, parallel support for the screen and accel electrodes.

3. Final Assembly and Alignment

Final assembly requires accurate aperture alignment or beam vectoring occurs. Since the screen and accel electrode hole patterns are purposely misaligned to compensate for beam divergence, this alignment is not trivial and a number of techniques were tried unsuccessfully. The technique which has been most successful aligns the grids while in contact in a special fixture and provides a means of

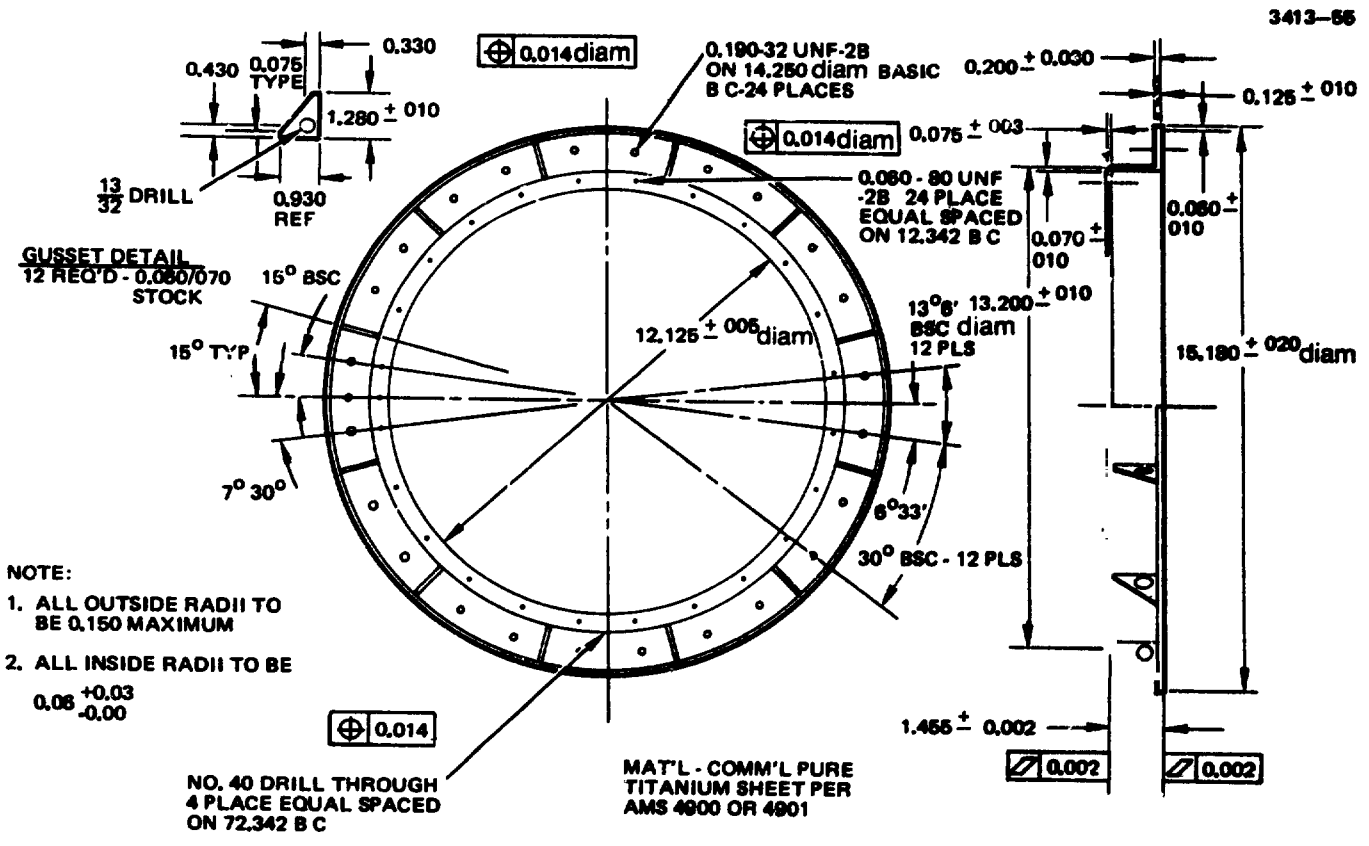

Fig. 53. Mounting structure and complete grid system assembly.

M10403

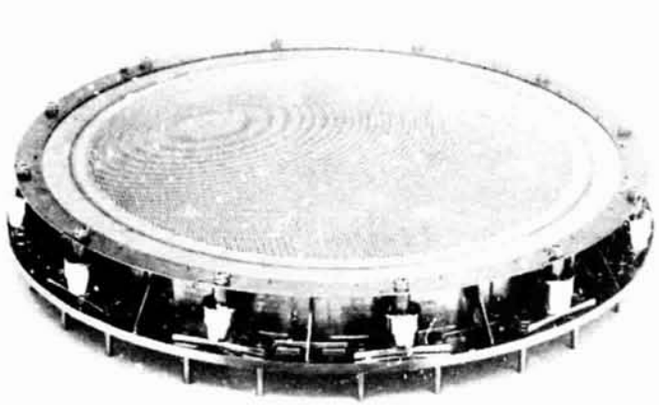

(a) Downstream view

M10404

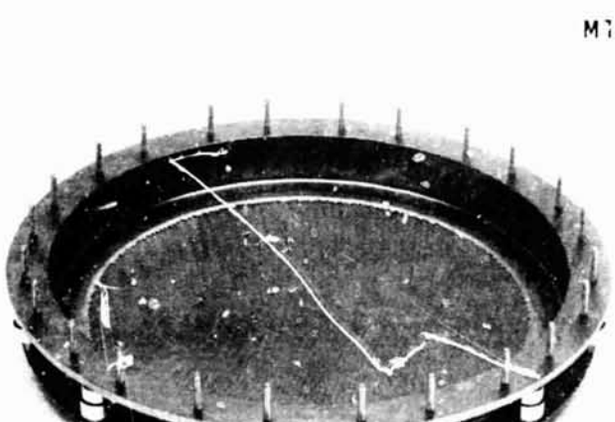

(b) Upstream view

Fig. 54. Grid system assembly using the advance mounting structure.

accurately drilling alignment holes in the outer, inactive mounting area. An alignment tool inserted in these alignment holes assures aperture alignment when the electrodes are assembled on the mounting structure.

Adjustment of the electrode spacing is relatively simple if the support structure mounts are plane, parallel and the electrodes are conformal. The acclerator spacers are all cut to the same length so that the nominal accel to grid electrode spacing is 0.05 to 0.07 cm in the central region, and the assembly spacing is documented by measuring the spacing at the locations shown in Fig. 55 with wire "feeler" gages. If any of the spacings measured on the 4.5-cm radius circle fall outside this tolerance, it is necessary to attempt to "adjust" the spacing by using washer shaped shims on the accel mounts and remeasuring until satisfactory spacing uniformity is achieved. Reproducible performance from grid set to grid set has been established by use of this technique, though it may take numerous iterations to achieve the required spacing uniformity if the use of shims is necessary.

4. Initial Operation of Ion Optical System

Initial operation of the ion optical system is usually accompanied by frequent breakdown between the electrodes and can result in permanent damage if some caution is not exercised during a "breakin" period. This period is significantly shortened if the electrodes have been lightly electropolished and care has been taken to keep them free from dust, moisture, and other volatile contaminants. Initial operation at total voltages of 1000 to 1200 V and beam currents of 1 A to 1.5 A for several hours in good ambient vacuum (less than 5×10^{-6} torr) was found to minimize breakdown between the electrodes during the run-in period.

B. Discharge Chamber and Subassemblies

Redesign of the discharge chamber under the Low Voltage 30-cm Thruster Program introduced several changes in component designs

30 cm OPTICS ASSEMBLY RECORD
SCREEN ACCELERATOR SPACING CHART

DATE: _____
TECH: _____

MOUNTING RING ASSEMBLY S/N _____
ACCELERATOR ELECTRODES S/N _____
NOTES: _____

SCREEN ELECTRODES S/N _____
NOTES: _____

TYPE _____
DRAWING NO. _____
APERTURE dia _____
SPACING CTR/CTR _____
THICKNESS _____

DRAWING NO _____
APERTURE dia _____
SPACING CTR/CTR _____
THICKNESS _____

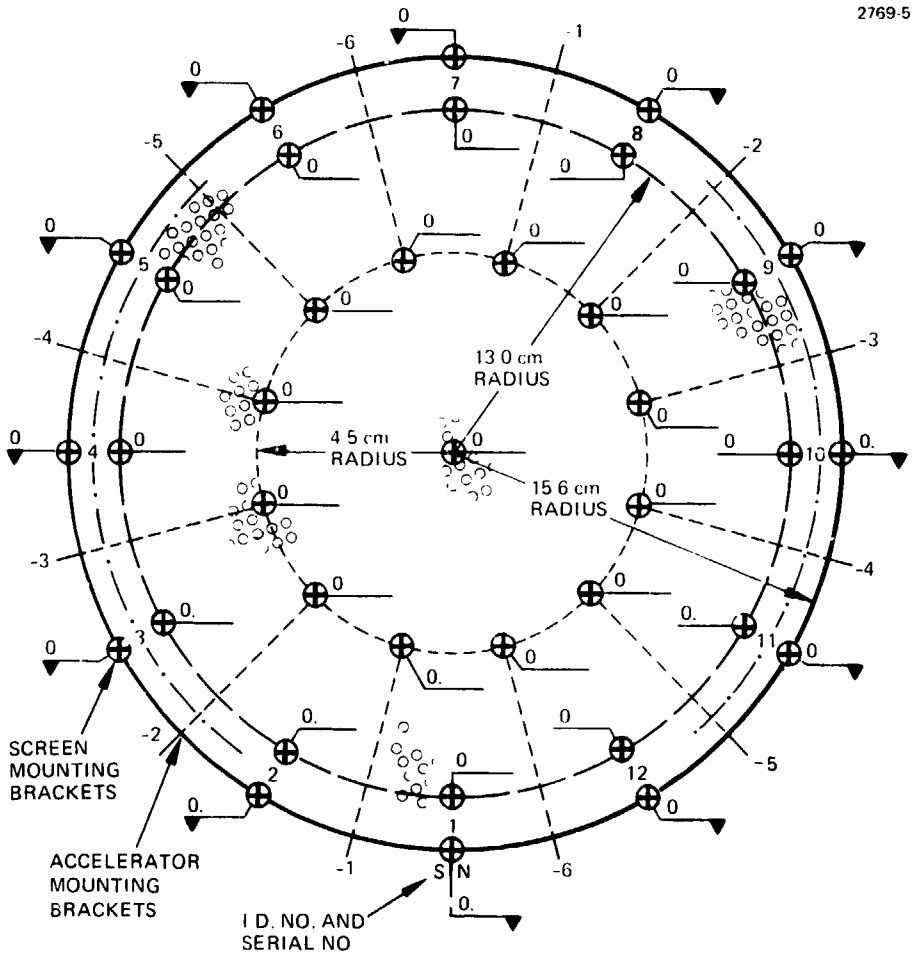

Fig. 55. Final grid spacing data sheet.

intended to alter the thermal characteristics of the thruster. Initial evaluation and design iterations were performed under this program. Primary considerations were operability within EM thruster power processor specifications and thermal characteristics which satisfied design criteria. The thruster investigated was described earlier in Section II and incorporated the new component designs and aluminum support beams, but did not include all titanium construction and gimbal mounts as designated for the EM thruster discharge chamber.

1. Thruster Cathode

The cathode design proposed for inclusion in the EM thruster had two new features which required verification. First, the main thruster cathode was thermally isolated from the electrical isolator and new thermal characteristics were anticipated. Secondly, the cathode heater design had been changed from a brazed on swaged heater to a flame sprayed type. This required the development of a new thermal model to provide guidance in locating the cathode insert so that acceptable temperature (800°C) is not exceeded under starting or running conditions.

A series of cathode thermal profiles, both in bell jar tests and in operating thrusters, were obtained at HRL and at LeRC with cathodes of essentially this design. From this data a semiempirical thermal model has been derived and used to effect a thermal balance for the cathode under various operating conditions. This data is presented in Figs. 56, 57 and 58. The data has also been used to estimate the thermal profile along the cathode under various conditions as shown in Fig. 59. Perhaps the most important points to note here are that when heated by the discharge there is a large (~150°C) temperature gradient between the cathode and the insert due to the limited conduction along the cathode tube under the heater and that there is also a large thermal gradient along the insert itself because of its location behind the heater. The much cooler cathode support (250°C in the present design compared to the previous 450°C) also contributes to the decrease in temperature at the upstream end of the insert. The cathode was

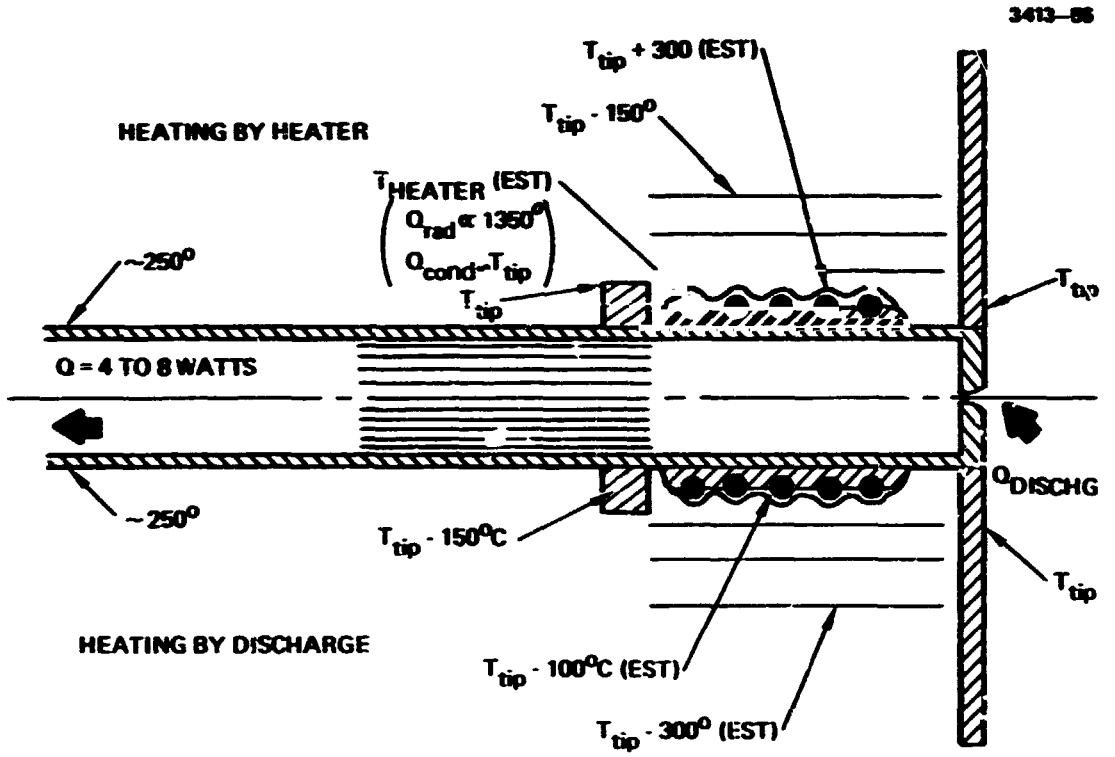

Fig. 56. Cathode model used in thermal analysis.

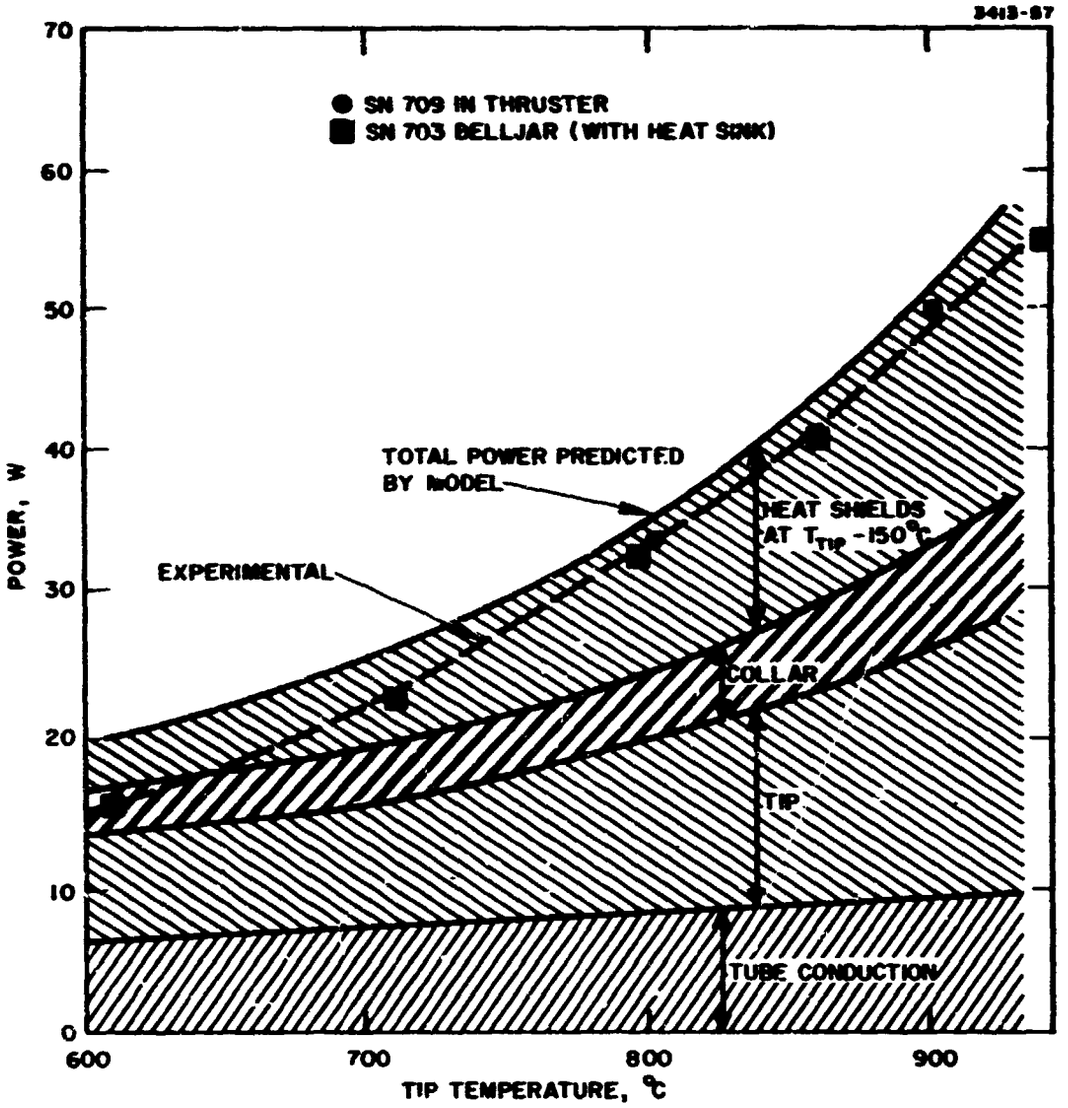

Fig. 57. Power balance during heatup before ignition.

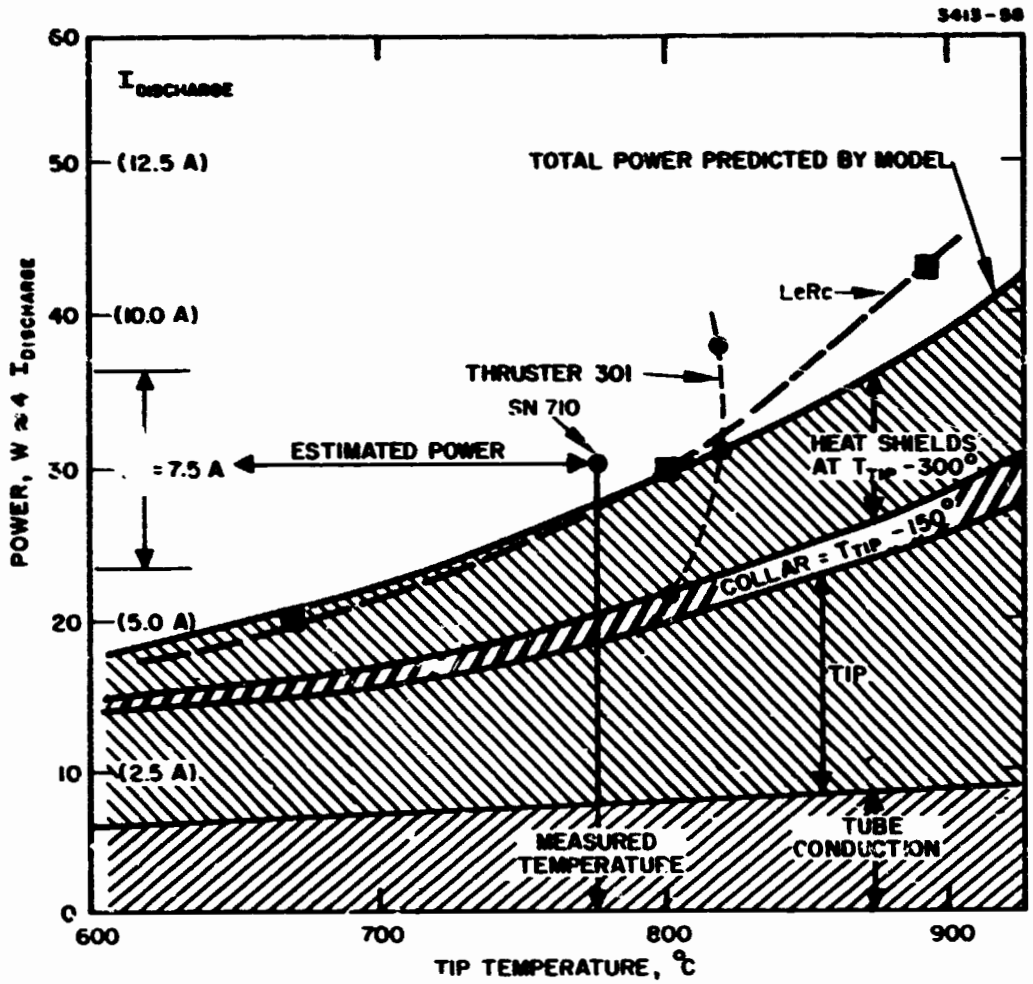

Fig. 58. Power balance when cathode heated by discharge.

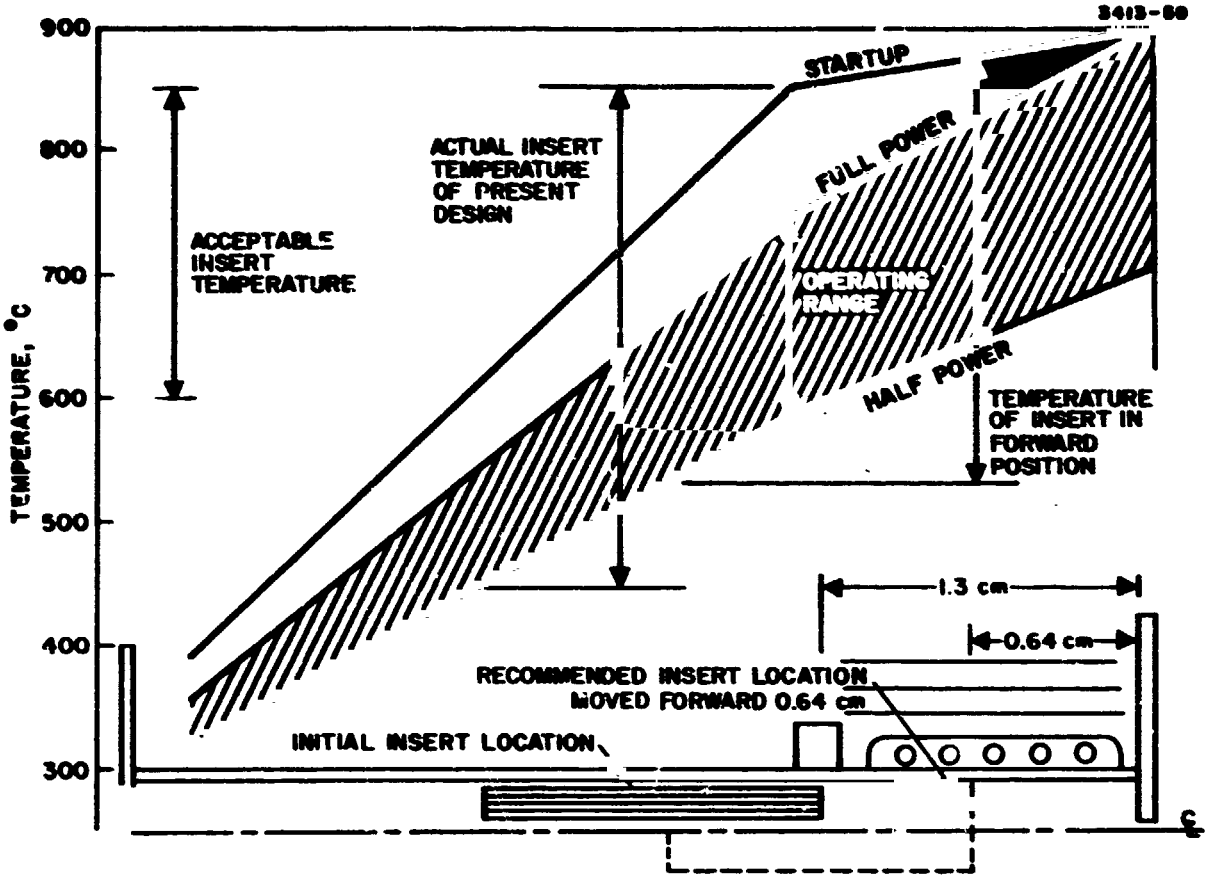

Fig. 59. Cathode temperature profiles predicted by thermal model of Fig. 55, for various operating conditions.

observed to start with some difficulty with the insert in its initial location, and based on the temperature profile shown in Fig. 59, the insert was moved forward to 0.64 cm from the cathode tip, thus bringing the downstream end of the insert to 850°C at 55 W of heater power. A cathode was modified in this manner, installed in the EM discharge chamber design thruster (SN 301-A), and tested with thermocouples located as shown in Fig. 60. Table 20 gives some representative thermal data for both startup and run conditions. Installation of this modification in SN 301-A restored reliable cathode ignition without difficulty – typically with less than 100 V keeper voltage for 60 W of tip heater power. The subsequent EM thruster cathode design evolved makes use of the cathode, radiator and heat shield configuration shown in Fig. 56, with the cathode insert located 0.64 cm from the cathode tip. The cathode orifice geometry was unchanged.

2. Isolator-Vaporizer Assemblies

Separation of the cathode and cathode isolator – vaporizer assembly was first instituted under this program for thermal evaluation. Both the cathode and main vaporizers are now isolated from the high voltage of the discharge chamber by the same isolator design (see Figs. 61 and 62). These design changes were instituted as a result of insulator deterioration which was attributed to operation at temperatures greater than 300°C and conversion of contaminants to semiconductors. Design features which corrected this condition are the double, re-entrant insulator coverings, removal of heaters from insulator line-of-sight, and thermal isolation from the discharge chamber through a mounting flange of adjustable thermal conductivity. After several iterations on the thermal conductivity of the tube connecting the cathode and cathode isolator, equilibrium temperatures shown in Table 20 were obtained at the points monitored (see Fig. 60). For operation in the normal test environment, these temperatures were considered satisfactory and no further modifications were recommended. No measurable isolator leakage has been observed in this design under this program.

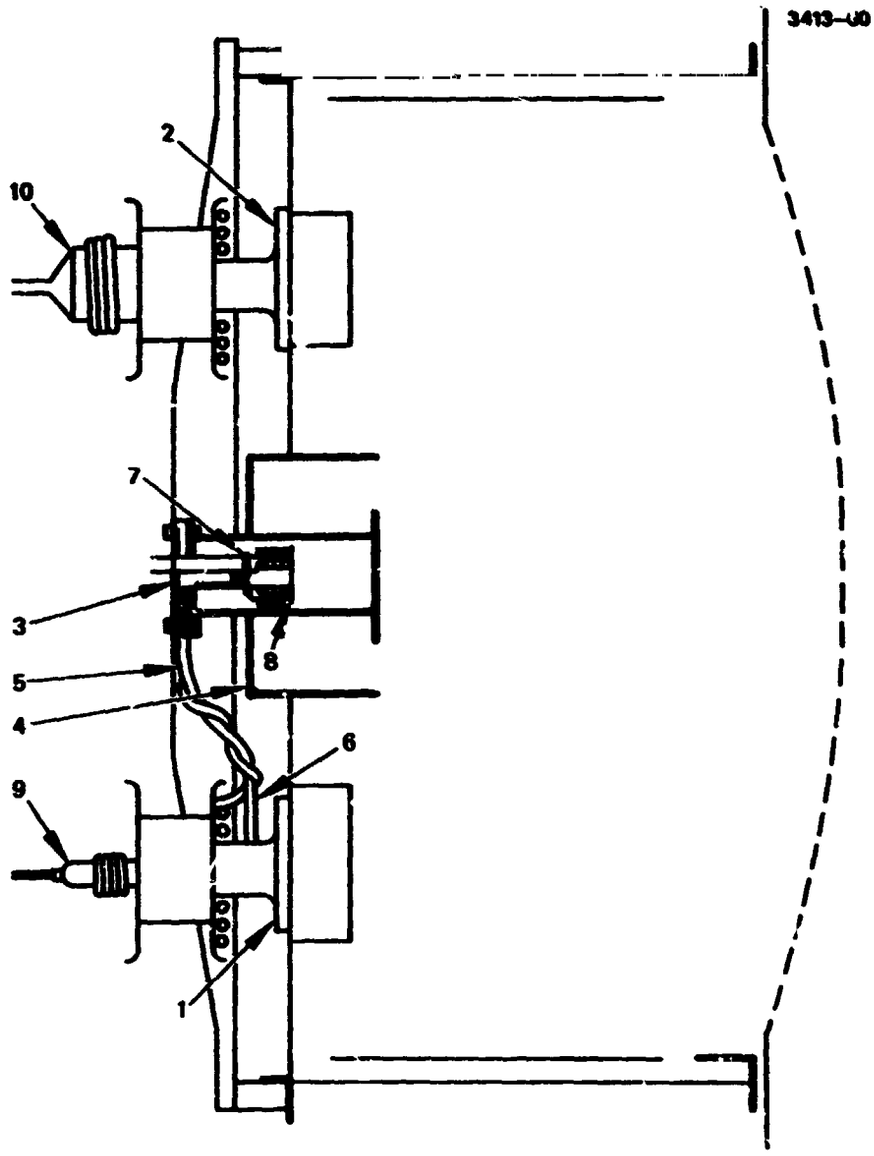

Fig. 60. Schematic drawing of thruster discharge chamber showing thermocouple locations for data given in Table 20.

TABLE 20

Thermal Data for Thruster SN 301-A with Heat Shielded Cathode (SN 710)

Beam Current J_B	Power Inputs, W						Temperatures, °C									
	Discharge Power	Cathode Heater	Main Isolator	Cathode Isolator	Main Vaporizer	Cathode Vaporizer	Cathode Isolator	Main Isolator	Cathode Plate	Cathode Flange	Feed Tube	Feed Tube	Cathode Collar	Cathode Radiator	Cathode Vaporizer	Main Vaporizer
0	0	26.4	16.8	16.4	0	0	140	210	193	9[illegible]	224	280	641	692	1[illegible]8	108
0	0	41.4	16.8	16.4	5.1	7.5	209	259	272	170	292	331	780	818	322	230
0	0	53.5	16.8	16.4	5.1	7.5	236	273	318	216	330	355	865	896	365	240
1.5	271	Off	Off	Off	7.5	5.5	220	227	332	311	317	232	735	906	322	280
0	0	48.3	16.8	16.4	5.1	7.5	229	256	294	195	312	313	825	851	350	229
2.0	370	Off	Off	Off	9.8	5.9	247	249	72	357	353	258	797	955	325	290
0	0	27	16	16	0	0	142	173	188	100	218	285	640	695	170	200
0	0	54	16	16	5.1	7.5	219	252	298	207	310	342	842	874	316	261
0.5	94	Off	Off	Off			172	177	258	214	242	182	665	760	332	240
1.5	278	Off	Off	Off	7.5	5.5	220	222	301	295	292	228	625	820	331	281

T1353

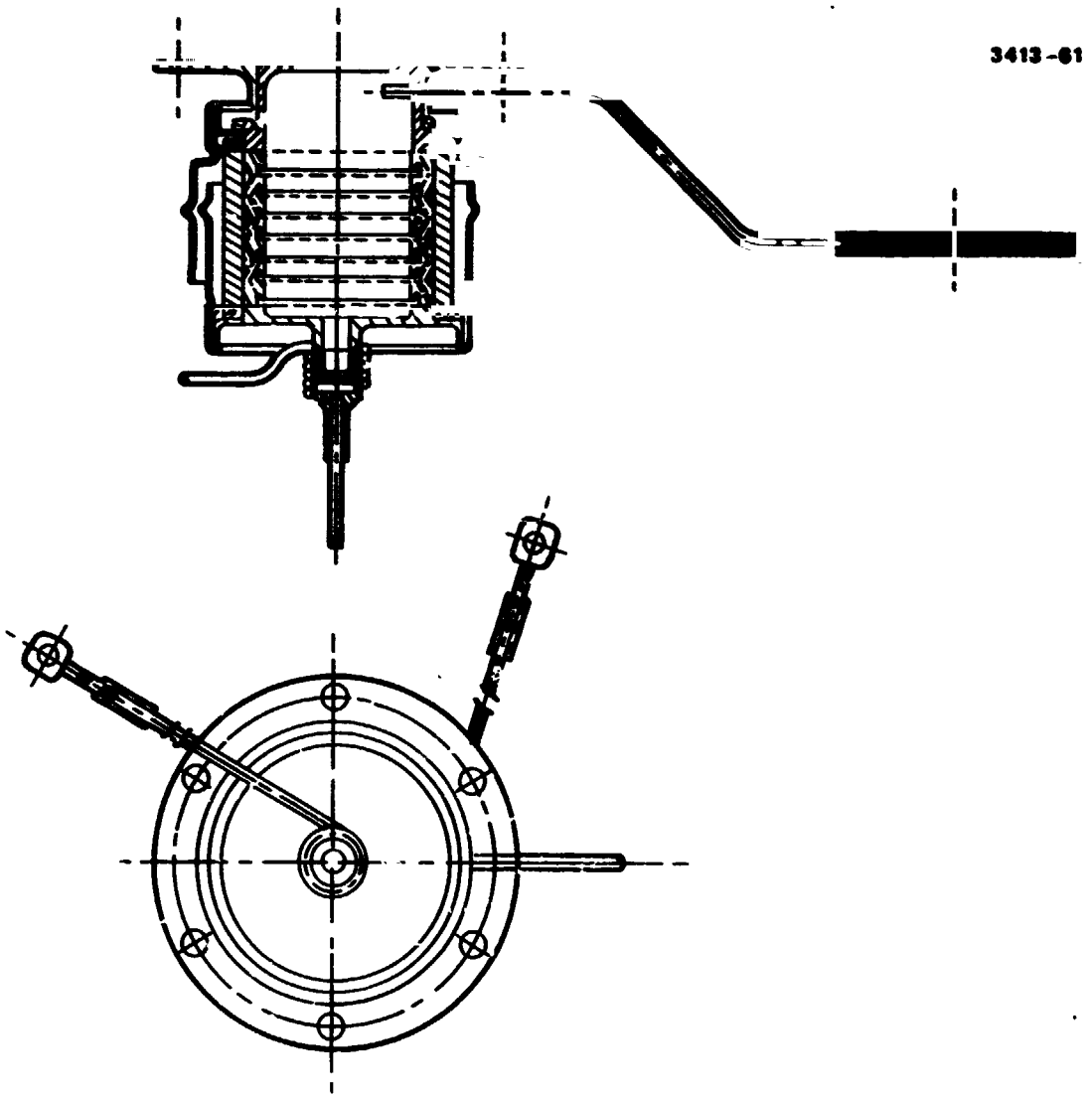

Fig. 61. Cathode isolator-vaporizer — assembly P/N D1026622.

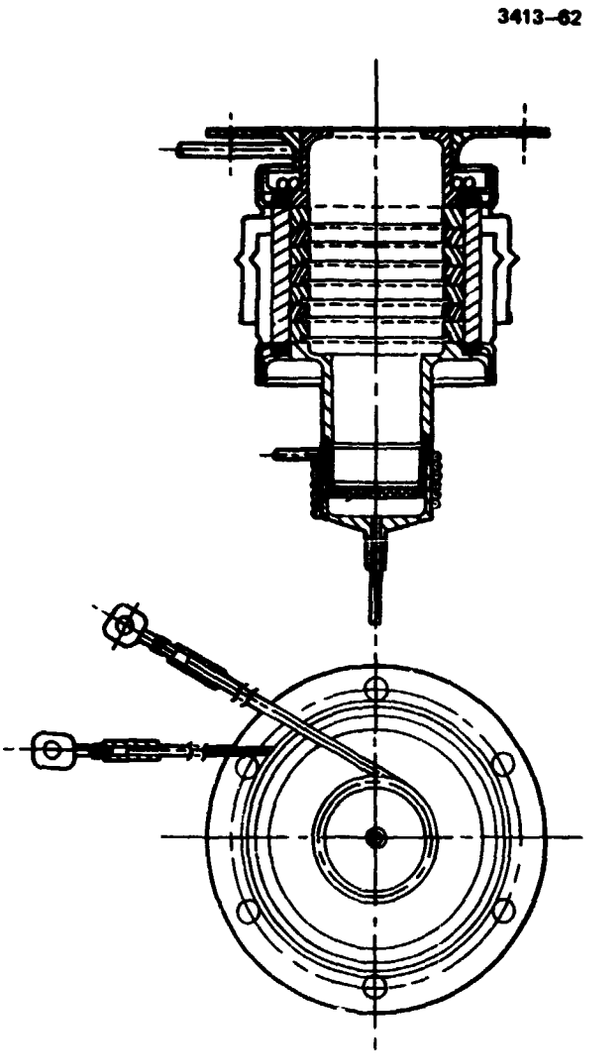

Fig. 62. Main isolator-vaporizer — assembly P/N D1025275.

3. Neutralizer Cathode Design

As in the case of the thruster cathode, introduction of the flame sprayed alumina encapsulated heater design significantly changed the neutralizer cathode temperature distribution and required modification of the keeper electrode geometry to provide clearance for the heater lead. Fig. 63 shows the final configuration verified. The cathode orifice and tip thickness were fixed at 0.038-cm diam and 0.127 cm, respectively, with keeper aperture diameter specified as 0.64 cm. Cathode to keeper spacing which provided the best control function was 0.127 cm. When operated in the usual control mode the temperature distributions shown in Fig. 64 were obtained. With the insert located 0.95 cm from the cathode tip as shown, the temperature was well within the specified "safe" range, however keeper ignition on initial start-up was marginal if heater power was limited to 50 W (power processor specification). Under any circumstances, heater power in excess of 75 W was found to damage the encapsulation of the heater wire and relocating the insert 0.64 cm from the tip was recommended.

C. Summary

The component development activity under this program, as discussed in this section, was directed primarily towards verifying specific designs or providing design alternatives for engineering model thruster development. Except for structural qualification, these designs are proving to be quite satisfactory as evaluated under the Endurance Test Program (NAS 3-15523). Some components may require further development to improve reproducibility, structural characteristics or fabrication facility. Component designs which may be identified as having potential difficulties include cathode tip heaters, vaporizer assemblies, permanent magnet/iron pole assembly and the neutralizer assembly. These designs are currently being examined for further improvement under the engineering model thruster development programs.

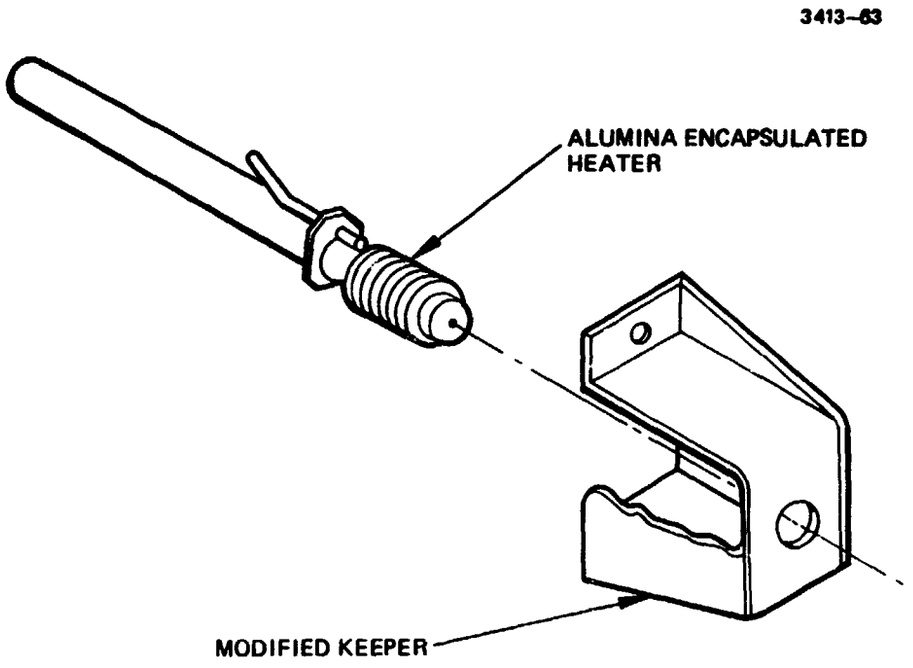

Fig. 63. Neutralizer cathode and modified keeper geometry.

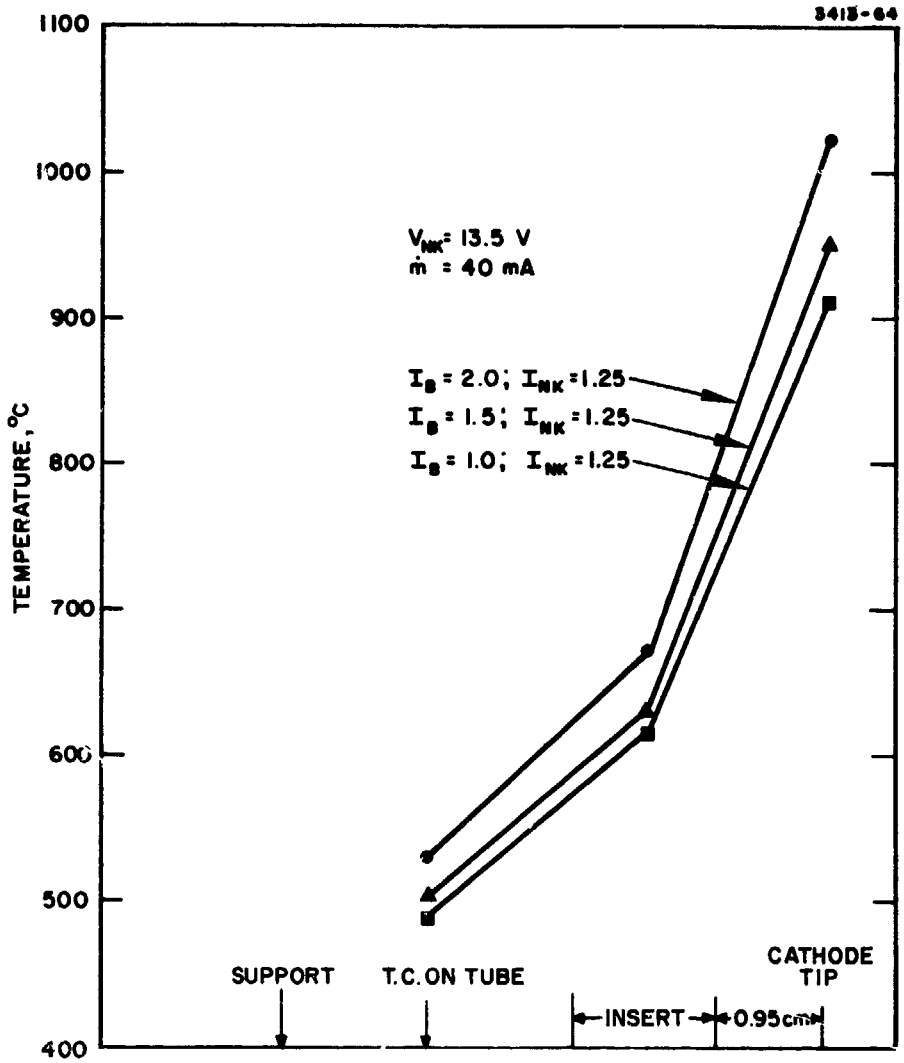

Fig. 64. Neutralizer thermal profile for neutralizer assembly.

VII. CONCLUSIONS

The 2.5 kW 30-cm mercury ion thruster has achieved remarkable gains in efficiency, structural stability, and projected lifetime as a result of the combined efforts of the NASA LeRC and HRL Laboratories under this and other associated programs. The Low Voltage 30-cm Thruster Program (NAS 3-16528) provided the structural design and evaluation together with the improved fabrication techniques necessary for advancing the hardware status to that of an engineering model. The Endurance Test Program (NAS 3-15523) identified early failure modes which have consequently been eliminated by improved designs. The role and responsibility of this program in this combined effort was one of design modification evaluation. Problem areas were identified and solutions were provided. Thrust losses resulting from double charged ions and beam divergence were carefully documented for the first time. NASA LeRC personnel coordinated these efforts and provided essential test and design data from NASA internal programs when necessary. The principle accomplishments of this program were the initial evaluation and design iterations which insured that the prototype EM thruster fabricated was capable of operation at the design specifications. As concerning this program, the initial thruster (SN 701) operated with many new component designs at satisfactory temperatures and a total efficiency of 71% corrected for double charged ion and beam divergence thrust losses.

A further goal of this program was to determine whether overall efficiency could be increased to 73% or greater through reduction of double charged ion thrust losses by either thruster modifications or changes in operational techniques. While this goal was not met or surpassed, several factors have been identified which show promise of meeting this goal. Further gains are anticipated by increasing the ion optical system screen transmission (open area) and decreasing accelerator grid transmission. One modification of this type evaluated under this program produced an increase in propellant utilization without an offsetting increase in double charged ion production, thereby increasing overall corrected thruster efficiency to 72.8% at full power.

Another factor which offers a possibility for improved performance is the reduction of oscillations in discharge current. These discharge current oscillations have been linked with magnetic fields in the cathode orifice region and at least one discharge configuration has been evaluated in which the oscillations were almost eliminated and the double charged ion production was measurably reduced. Consequently, while an important milestone in thruster development has been reached with the development of the engineering model thruster, worthwhile gains in lifetime and stability, if not efficiency, may still be possible through further investigation of the influence that these factors have on double charged ion production.

Interactions between thruster and power processor were not pursued under this program to any extent greater than necessary to provide stable operation for thrusters being evaluated. Thruster design modifications introduced into the EM thruster produced minimal impact on the power processor specifications and the control system designated under the prior 30-cm thruster program (NAS 3-14140).

On the basis of operational stability and reliability observed in the tests performed under this program, the discharge chamber and ion optical system components developed for the EM thruster design performed satisfactorily. It should not be necessary to modify these designs unless new constraints are imposed or fabrication difficulties arise.

In summary, the work performed under this program comprised an assortment of advanced thruster design verifications, evaluations, and documentations. The end result is an engineering model thruster which incorporates technological advances in nearly every design detail. This was accomplished without significant delay or redirection of the programs responsible for development, fabrication, and structural and endurance testing of the EM thruster. Moreover, an assessment of critical design features was made possible by providing a background of information concerning both capabilities and shortcomings significantly before the prototype EM thruster hardware was available. On the basis of these assessments, recommended areas for further consideration have been identified.

APPENDIX

DISCUSSION OF COLLIMATED MASS SPECTROMETER PROBE TECHNIQUES AND DATA ANALYSIS

This appendix presents the details of the collimated mass spectrometer ion beam probing system; including the methods of data acquisition and computerized analysis for obtaining beam divergence and double charged ion thrust loss factors.

A. MASS SEPARATOR

The probe unit is shown in Fig. 65 and schematically in Fig. 66. It consists of a collimator, an E x B separator section, a drift tube. a separation aperture, and a collector. In order to focus on a sufficiently small area of the accelerator grid, a collimator with an acceptance half angle of 0.3° was chosen. Thus, at an axial distance of 38 cm the probe viewing area is 0.132 cm^2. The magnetic field is provided by a small 1400 G permanent magnet. The electric field plates are perpendicular and equal in length to the magnetic poles. The location of mass separator in relation to the thruster is shown in Fig. 67, where θ is the probe angle relative to the beam axis, and r is the thruster radial position. Both the angular and radial positions of the probe are maintained with the use of stepper motors. A typical probe output trace is shown in Fig. 68; where the collector current is plotted as a function of voltage applied to the E. -field deflection plates.

B. DATA ACQUISITION TECHNIQUE

A data scan is taken by fixing the dispersion angle, θ, and measuring at a number of thruster radial positions, r, the single and double ion probe collector currents i^+ and i^{++}. These measurements are then repeated for a number of different angles. The data are collected on paper tape which furnishes direct input into the computer.

3173-10

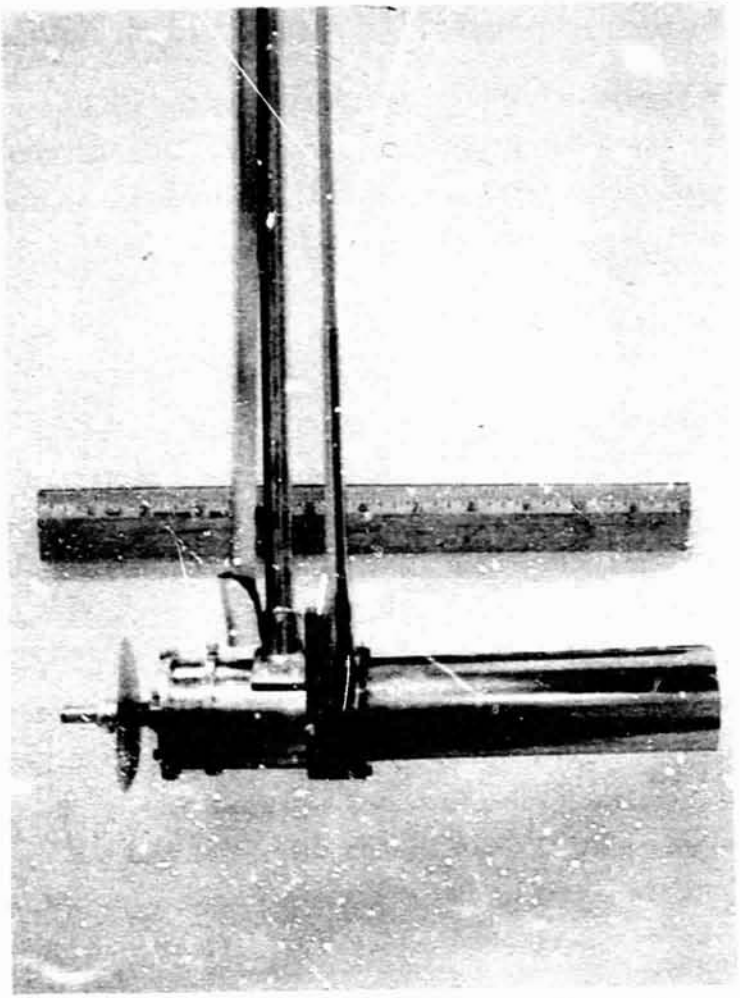

Fig. 65. Collimated mass spectrometer probe.

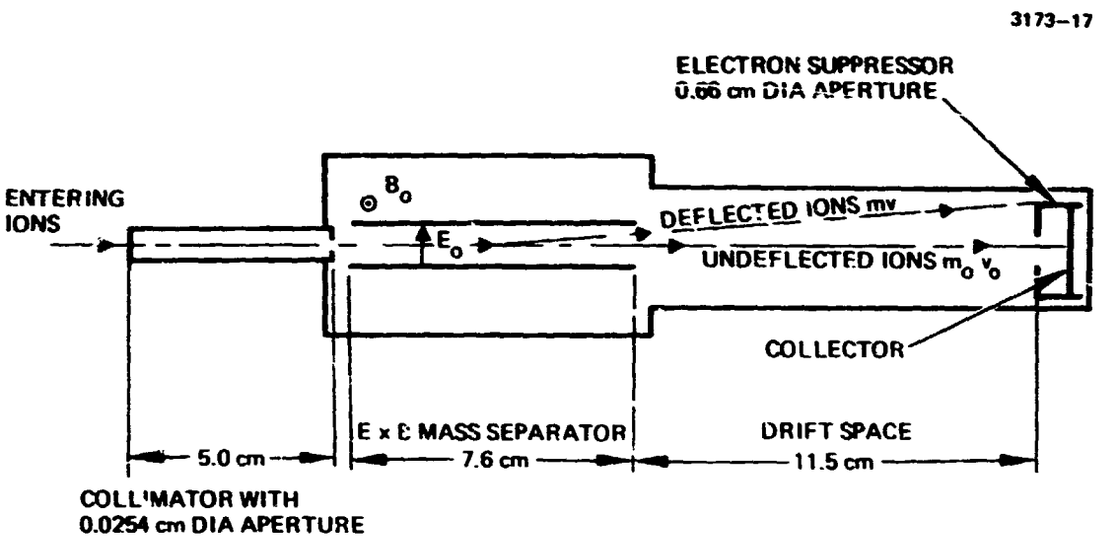

Fig. 66. ExB mass separator probe schematic.

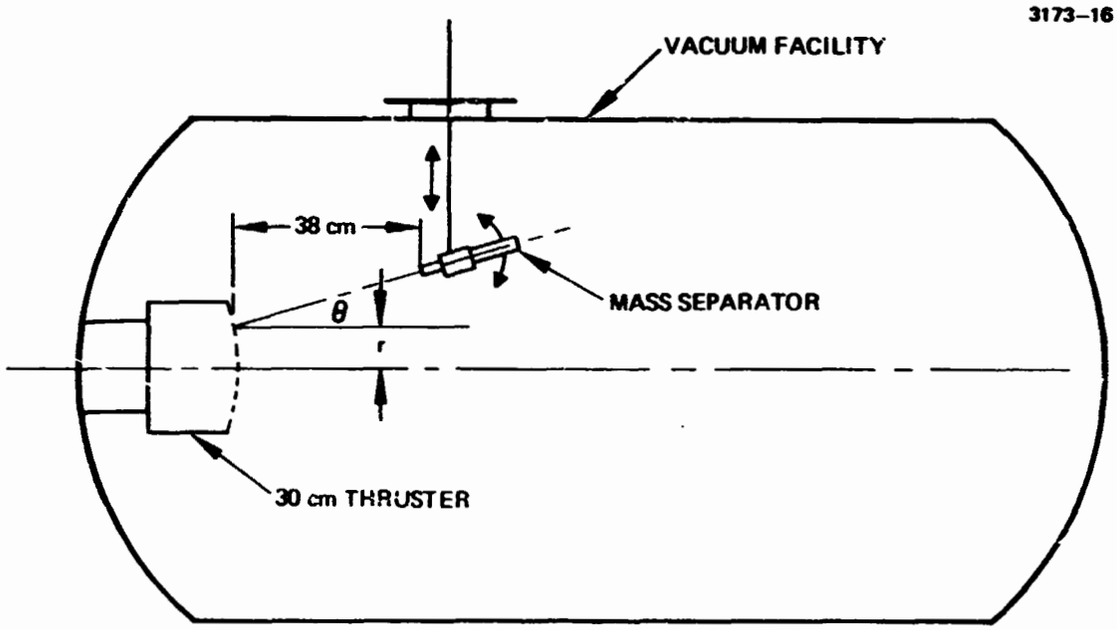

Fig. 67. Thruster and mass separator position in vacuum facility.

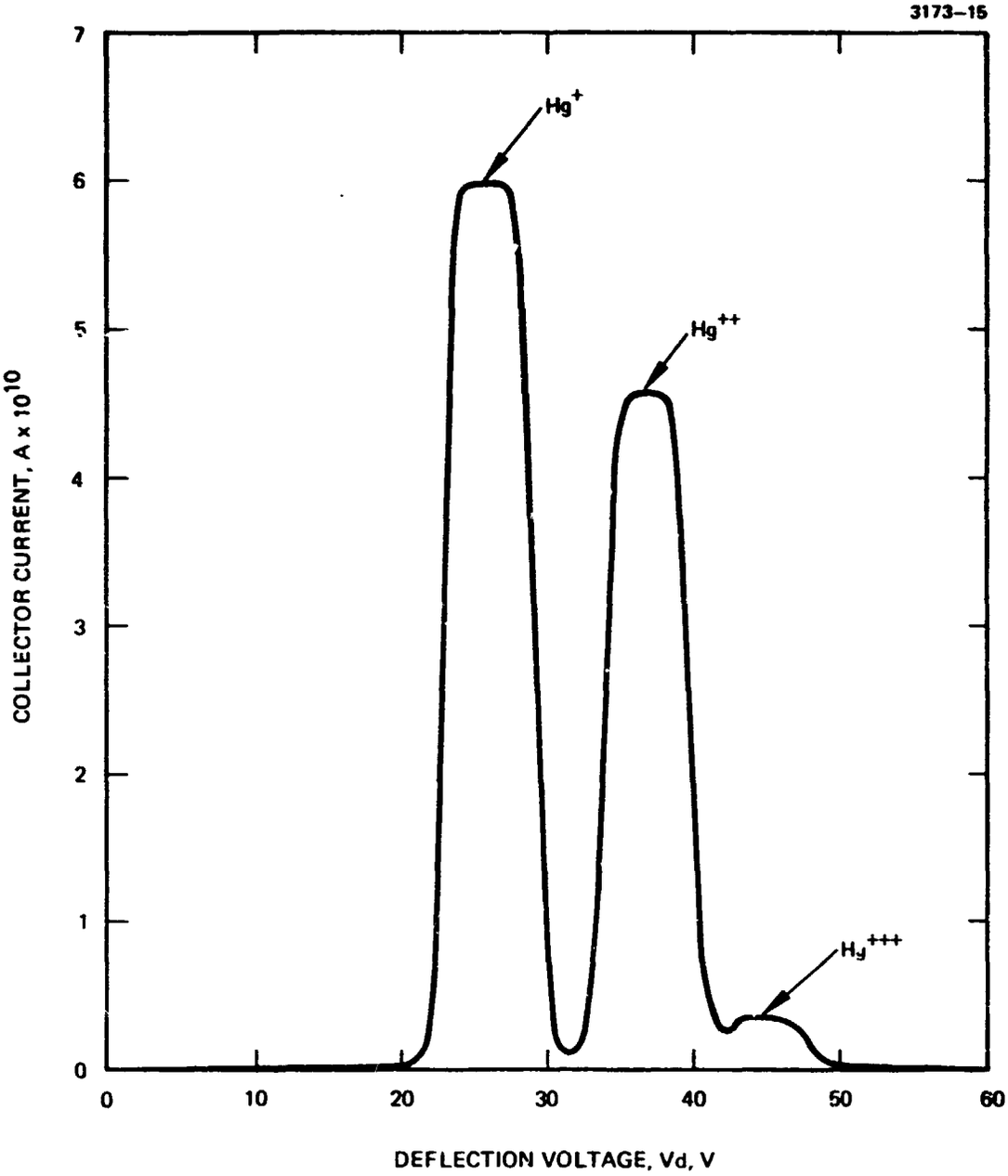

Fig. 68. Charge-species separator output trace (I_B = 2.0 A, V_D = 42 V).

In the development of the computer program for data analysis, one of the primary objectives was to use the minimum number of data points subject to the constraint that the accuracy of the reduced data should be at least comparable to that of the raw analyzer probe data (estimated 3 to 5%). By minimizing the data collection time it was ensured that the thruster operating conditions would remain as constant as possible during the data scan, and also relieve the operator of the time-consuming task of taking more data than was really necessary. In these initial experiments, a number of scans with a different number of data points were run and it was found that four equally spaced r values and seven equally spaced θ values were near optimum. A larger number of r data points produced essentially the same results while a smaller number produced discontinuous appearing curves. While six values of θ for each r value was usually satisfactory, seven were better for grids with larger dispersions. The final technique chosen and used in all the cases discussed below was to use four r values and seven θ values resulting in a total of 56 data points per run (28 each for i_+ and i_{-+}).

C. DATA ANALYSIS AND COMPUTATION

As described above, the experimental data represents the angular current distribution, $i(\theta)$, measured in the vertical plane emanating from four elemental accel areas on the vertical radius of the accelerator grid. Each of the four sets of $i_+(\theta)$ and $i_{++}(\theta)$ data points are integrated over θ to obtain the total $J_+(r)$ and $J_{++}(r)$ current densities at these four radial positions. By integrating the J_+ and J_{++} current densities over the accel grid the total current fluxes I_+ and I_{++} are obtained which are used for calculating the thrust and mass utilization correction factors α and β, where

$$\alpha = \frac{\text{Thrust Corrected for } Hg^{++}}{\text{Thrust Computed from Measured Beam Current and Voltage}}$$

$$= \frac{I_+ + \frac{1}{\sqrt{2}} I_{++}}{I_+ + I_{++}}$$

$$\beta = \frac{\text{Ionized Propellant Flowrate}}{\text{Measured Propellant Flowrate}} = \frac{I_+ + \frac{1}{2} I_{++}}{I_+ + I_{++}} .$$

Similarly, the total thrust factor is found by current weighting the elemental thrust factor found by calculating the average cos θ at each of the four radial positions. The detailed calculations are described below. All these calculations assume axial symmetry both about the elemental areas and about the thruster center line. The program first reads in the input data generated on paper tape. Each of the seven lines of data is preceded by a line number. Each line has eight data points (four i_+ and four i_{++}) which correspond to a particular angle and four equally spaced radial positions (at r = 0, 1/4 r_o, 1/2 r_o, and 3/4 r_o where r_o = 14.5 cm). The program assumes the seven theta values are taken 5° apart and the minimum theta value must be typed in for each run. The program then plots out the input data. Since the actual data points are plotted, it is easy to detect a bad data point which occasionally occurs if the thruster arcs repeatedly during a data scan. After plotting the data, the program numerically evaluates the following integrals corresponding to the radial positions at r = 0, 1/4 r_o, 1/2 r_o, and 3/4 r_o:

$$J_{++}(r) = \int_{\epsilon_{min}}^{\epsilon_{max}} i_{++}(\theta, r)\, d\theta \qquad (1)$$

$$J_+(r) = \int_{\theta_{min}}^{\theta_{max}} i_+(\theta, r)\, d\theta \qquad (2)$$

$$TFAC(r) = \int_{\theta_{min}}^{\theta_{max}} (i_+ + i_{++}) \cos\theta\, d\theta \Big/ \int_{\theta_{min}}^{\theta_{max}} (i_+ + i_{++})\, d\theta\ . \qquad (3)$$

For these calculations, the integration limits θ_{max} and θ_{min} are the maximum and minimum data angles, plus 15° and minus 15°, respectively. At these end-points the currents are set equal to zero. These integrals are numerically evaluated by multiplying the $i(\theta)$ at the midpoint of each interval by the width. Between data points the numerical integration routine evaluates the $i(\theta)$ function by a second order interpolation routine. This simple method described above was found to give results which agreed closely with much more elaborate library routines using either Simpson or Legendre integration which were tried in the initial program checkout phases. The values for these twelve integrals (four each for J_+, J_{++} and TFAC) are printed out on a temporary file which can be integrated at the teletype. Note that the thrust factor TFAC (r) defined above is an elemental value and must be current weighted to find an average value for the thrusters.

The total current beam profile $J_{tot}(r)$ is generated by adding at each r, the single and double current densities described above. This profile along with similar ones for $J_+(r)$ and $J_{++}(r)$ are plotted and numerically integrated (using the same method as described above) as follows:

$$I_+ = \int_0^{R_{max}} J_+(r)\, 2\pi r\, d\, r \qquad (4)$$

$$I_{++} = \int_{o}^{R_{max}} J_{++}(r)\, 2\pi r\, d\, r \tag{5}$$

$$TFAC = \frac{\int_{o}^{R_{max}} TFAC\,(r)\, J_{tot}\,(r)\, 2\,\pi\, r\, dr}{\int_{o}^{R_{max}} J_{tot}\,(r)\, 2\,\pi\, r\, dr} \tag{6}$$

For these integrations the current densities are set equal to zero at r_o = 14.5 cm and a second order interpolation routine is used to evaluate the current density between data points. For the TFAC (r) a linear extrapolation between the 1/2 r_o and 3/4 r_o radial positions is used for TFAC (r_o).

The α and β efficiency factors are calculated as follows:

$$T_{Act}/T_{Meas} \triangleq \alpha = (I_+ + 0.707\, I_{++})/(I_+ + I_{++}) \tag{7}$$

$$\eta_{m\ Act}/\eta_{m\ meas} \triangleq \beta = (I_+ + 0.50\, I_{++})/(I_+ + I_{++}) \tag{8}$$

A summary of these efficiency factors, the total thrust factor, and the ratio of the total double current to the total current is printed out on a file which can be interrogated at the teletype.

D. RESULTANT COMPUTER OUTPUT

The computer generated plots using experimental data are shown in Figs. 69 and 70. The plotted analyzer data points versus theta are shown in Fig. 68 for both the single- and double-ionized current components. These data show the grid is well compensated since the current peaks close to the θ = 0 line. The synthesized

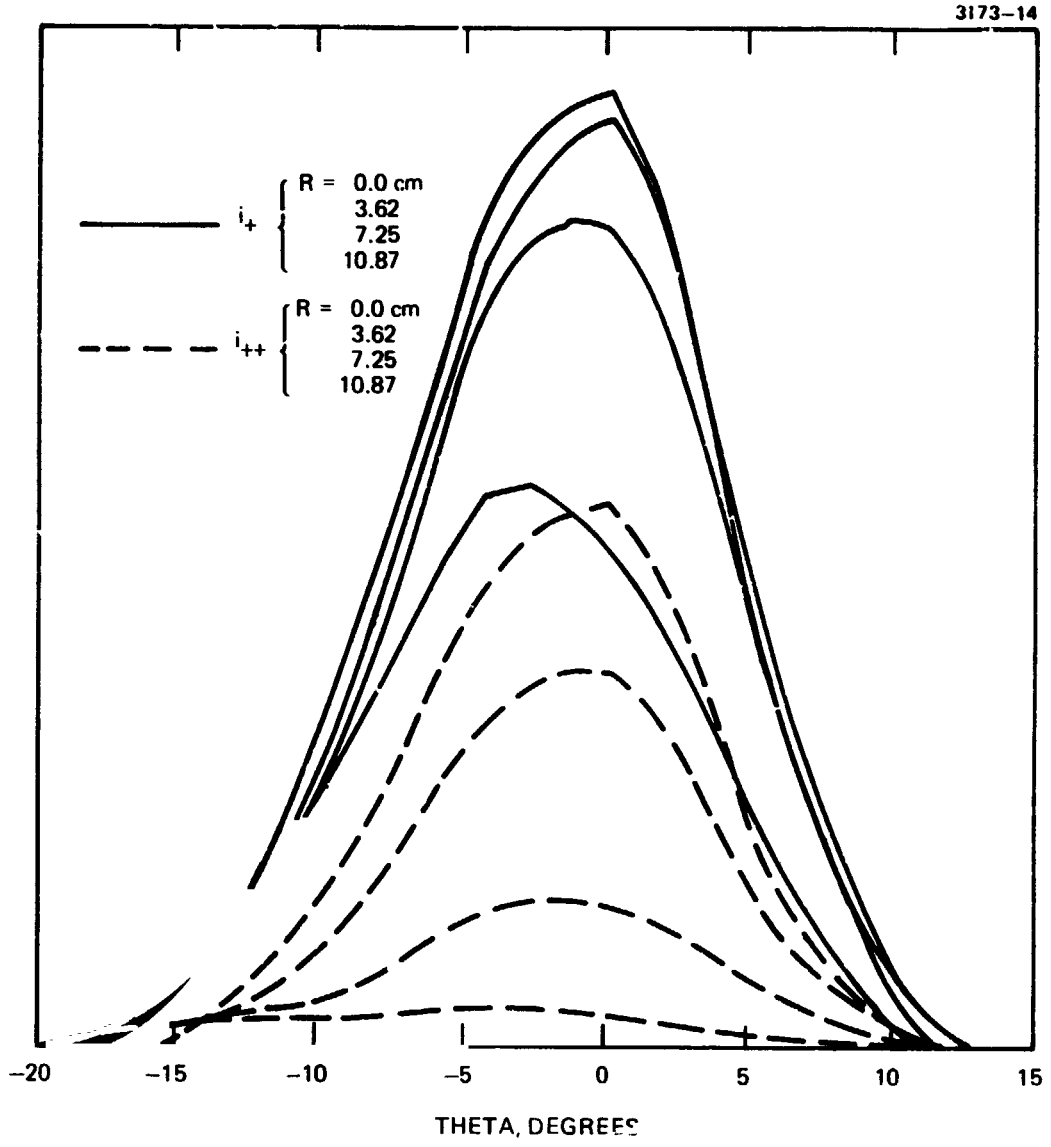

Fig. 69. Computer generated plot of measured ExB analyzer probe currents as a function of theta for R = 0, 3.62, 7.25, and 10.87 cm.

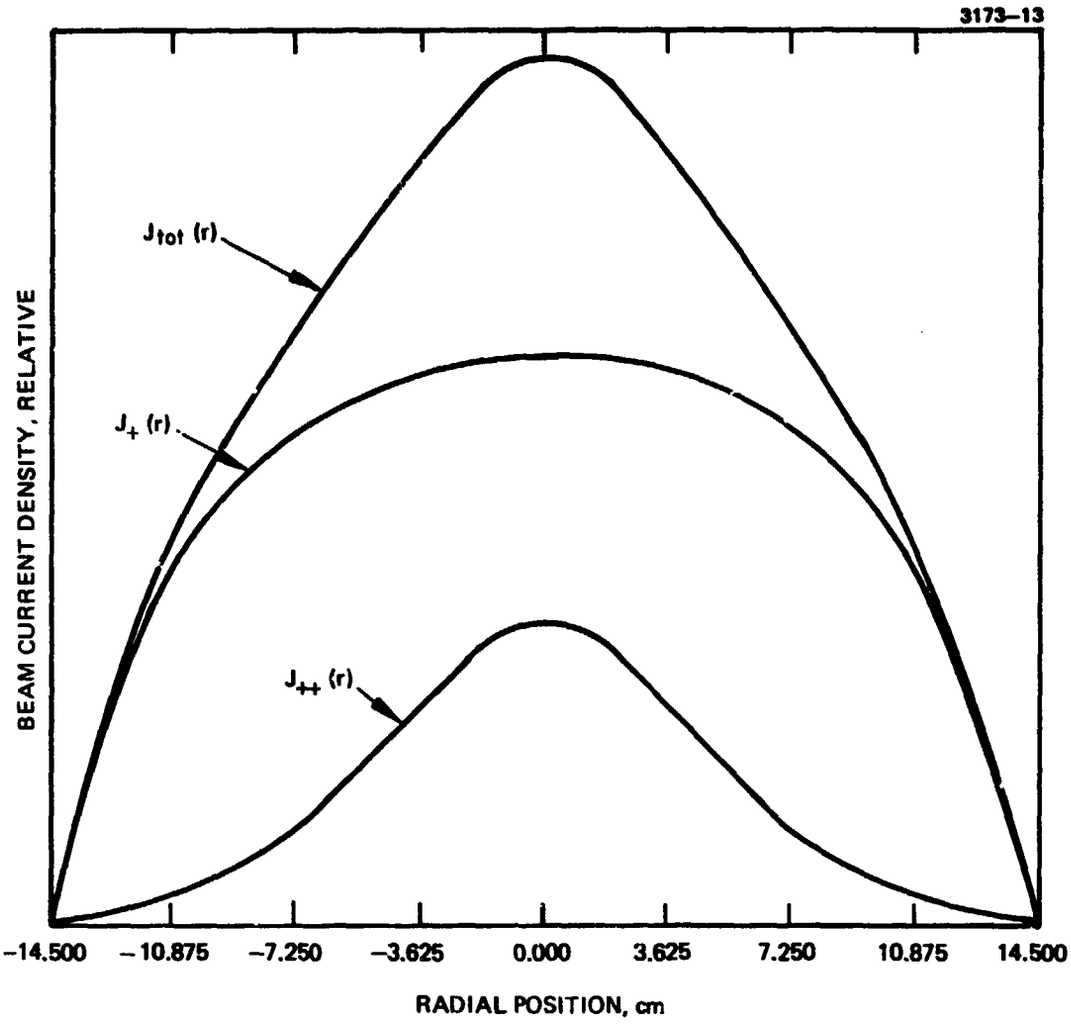

Fig. 70. Current density profiles for total single- and double-ionized current components at the accelerator grid as generated by computer analysis of mass spectrometer data obtained in a 30 cm thruster beam. (I_B = 2.0 A).

current density profiles shown in Fig. 70 show the typical behavior always observed in which the double-ionized current component peaks on the axis and drops rapidly as the beam edge is approached. For these current density profiles the negative r portion of the curve was generated by simply reflecting the positive half. As mentioned above, the probe only scans one radius of the grid so any nonaxially symmetric thruster behavior would result in erroneous computed results. A computer print-out of the summarized data for this case is shown in Table 21. This data shows the calculated value for the ratio of the double ion current to the total current, the thrust and mass utilization correction factors and a tabulation of the integrated angular current densities and the elemental thrust-factors for the four radial positions.

E. TEST CASE USING IDEALIZED DATA

In order to verify the inherent accuracy of the computer program an idealized situation was considered in which all the derived parameters could be calculated in closed form. The input data for this test case was calculated by assuming a gaussian distribution for the doubly and singly charged angular current distributions and a cosine distribution for the total current density profiles. In addition, the amplitude of the doubly charged angular current distribution was assumed to be exactly half the singly charged distribution for all r positions to produce a theoretical ratio of total double ion current to total current of exactly one third. The functional forms assumed are shown below where $A_o = 0.8$ and $\theta_o = 5^o$ for all radii.

$$i_+ (\theta, 0) = A_o \exp\left[-\frac{1}{2}\left(\frac{\theta}{\theta_o}\right)^2\right] \tag{9}$$

$$i_+ \left(\theta, \frac{r_o}{4}\right) = 0.9237\, i_+ (\theta, 0) \tag{10}$$

TABLE 21

Computer Print-out of Reduced Data. Case 1 is from Actual Experimental Data; Case 2 is from Data Used for Program Check-out

Case 1

	R=0	R=1/4R0	R=1/2R0	R=3/4R0		
J+=	8.831	8.608	7.840	5.552		
J++=	4.609	3.265	1.420	0.491		
TFAC=	0.995	0.995	0.995	0.993		
SUMMARY:	ITOT=	4305.503	I++=	679.653	TOTAL TFAC=	0.994
	I++/ITOT=	0.158	ALPHA=	0.954	BETA=	0.921

Case 2

	R=0	R=1/4R0	R=1/2R0	R=3/4R0		
J+=	10.033	9.269	7.092	3.840		
J++=	5.016	4.635	3.546	1.920		
TFAC=	0.996	0.996	0.996	0.996		
SUMMARY:	ITOT=	4628.063	I++=	1542.688	TOTAL TFAC=	0.996
	I++/ITOT=	0.333	ALPHA=	0.902	BETA=	0.833

T1354

$$i_+ \left(\theta, \frac{r_o}{2}\right) = 0.707\, i_+ (\theta, 0) \qquad (11)$$

$$i_+ \left(\theta, \frac{3}{4} r_o\right) = 0.383\, i_+ (\theta, 0) \qquad (12)$$

Note that the above amplitudes vary with r as cos $\pi/2\ (r/r_o)$ and were chosen in order to produce a cosine distribution for the total current density profiles. The input data for this case is shown in Table 21.

The calculated profiles using the input data of Table 21 is shown in Figs. 71 and 72. Note that reconstructed curves appear gaussian as would be expected. Similarly the total current profiles are smooth cosine curves.

F. THEORETICAL CALCULATION

We will now independently calculate all the results shown in Table 21 by using the mathematical properties of the functions from which the input data was generated.

1. Angular Current Distribution Integrals

Using the tabulated[1] properties of the gaussian error function, i.e.,

$$\int_{-\alpha}^{\alpha} \exp\left(-\frac{1}{2}x^2\right) dx = \sqrt{2\pi}$$

$$= \int_{-4}^{4} \exp\left(-\frac{1}{2}x^2\right) dx \text{ to } 0.001\% \qquad (13)$$

Equations 1 and 2 become using eqs. 9 and 13.

[1] Burington "Handbook of Mathematical Tables and Formulas"

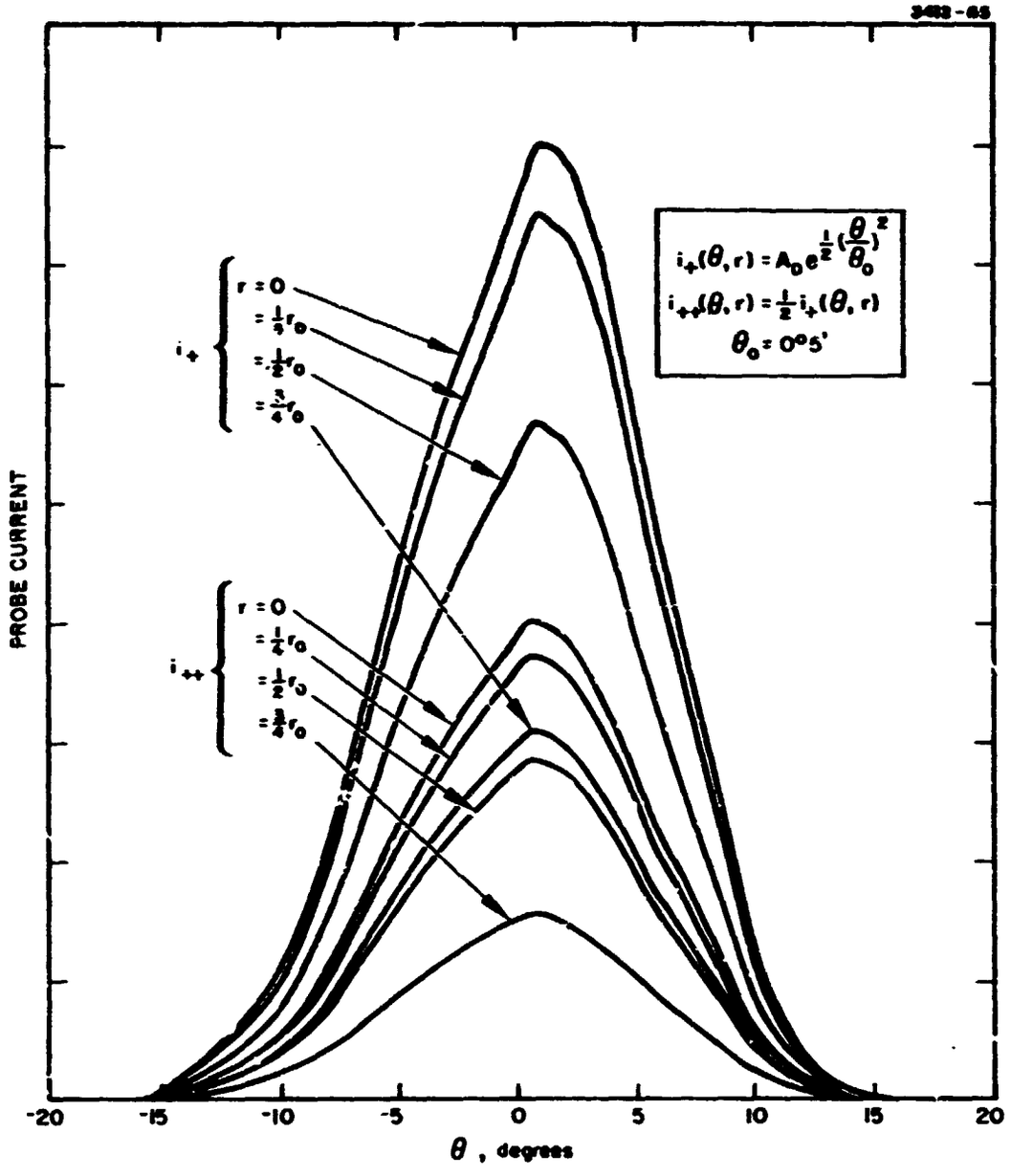

Fig. 71. Computer generated plot for idealized case using angular current density with gaussian theta dependence.

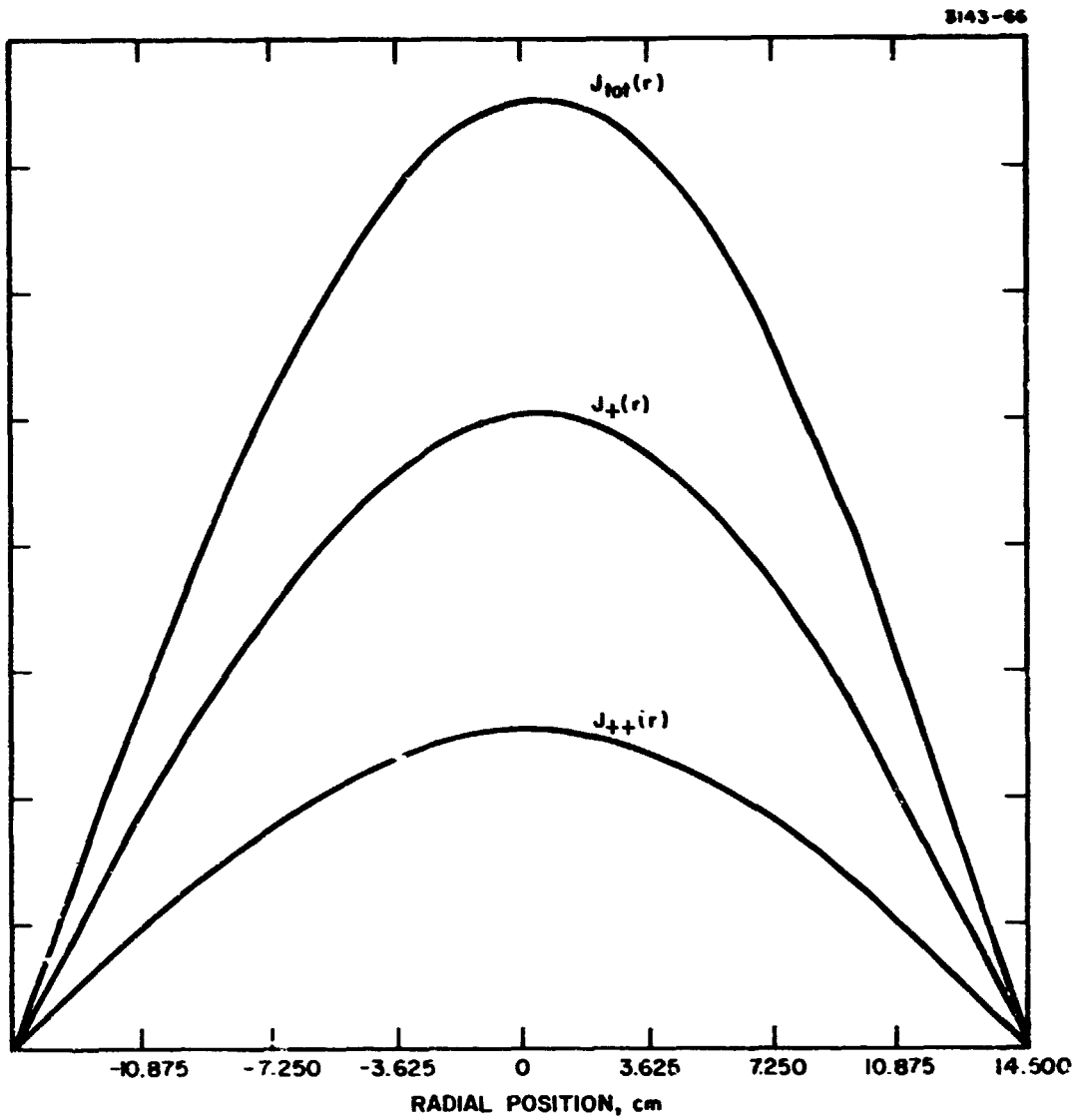

Fig. 72. Computer generated current density profiles for total singly- and doubly-charged current components at the accelerator grid. Curves were generated using idealized data.

$$J_+(0) = \int_{\theta_{min}}^{\theta_{max}} A_o \exp\left(-\frac{1}{2}\right)\left(\frac{\theta}{\theta_o}\right)^2 = A_o\,\theta_0\,\sqrt{2\pi} \qquad (14)$$

Numerically since $\theta_o = 5^o$ and $A_o = 0.8$

$$J_+(0) = (0.8)(5)\sqrt{2\pi} = 10.026$$

$$J_{++}(0) = \frac{1}{2} J_+(0) = 5.0132 \qquad (15)$$

Using eqs. 10 through 12

$$J_+\left(\frac{r_o}{4}\right) = 0.9237\, J_+(0) = 9.261$$

$$J_{++}\left(\frac{r_o}{4}\right) = 4.6305 \qquad (16)$$

$$J_+\left(\frac{r_o}{2}\right) = 0.707\, J_+(0) = 7.089$$

$$J_{++}\left(\frac{r_o}{2}\right) = 3.544 \qquad (17)$$

$$J_+\left(\frac{3}{4} r_o\right) = 0.383\, J_+(0) = 3.838$$

$$J_{++}\left(\frac{B}{4} r_o\right) = 1.919 \qquad (18)$$

Comparing these exact calculations with the computer generated values shown in Table 21, we see that for all cases the agreement is good to the third decimal point.

2. Thrust Factor Calculation

Because for this idealized case all radii have the same theoretical thrust factor you need only calculate one. Using eqs. 14 and 3, the thrust factor at any radius is

$$TFAC(r) = \frac{\int_{\alpha}^{\alpha} Ae^{-\frac{1}{2}\left(\frac{\theta}{\theta_o}\right)^2} \cos\theta \, d\theta}{\int_{-\alpha}^{\alpha} Ae^{-\frac{1}{2}\left(\frac{\theta}{\theta_o}\right)^2} d\theta} \qquad (19)$$

Since a standard integral form is

$$\int_{-\alpha}^{\alpha} e^{-px^2} \cos qx \, dx = e^{-q^2/4p}\sqrt{\frac{\pi}{p}} \qquad (20)$$

we have, using eqs. 14, 19, and 20

$$TFAC(r) = \sqrt{2\pi}A_o e^{-\frac{1}{2}\theta_o^2} \frac{A\theta_o}{\sqrt{2\pi}} = \exp\left(-\frac{1}{2}\theta_o^2\right) \qquad (21)$$

Since $\theta_o = 5^o = 0.03726$ radian

$$TRAC(r) = \exp\left(-\frac{1}{2}\right)(0.087)^2 = e^{-0.003807}$$

$$= 0.9962$$

Again the agreement is excellent since the computer program calculated 0.996 for all radii and for the total thrust factor.

3. Total Current Integrals and Efficiency Factors

Inspection of the r dependence for the singly and doubly charged current densities in eqs. 15 through 18 show the expected $\cos(\pi/2\ r/r_o)$ radio dependence. The total singly charged current assuming axial symmetry and a cosine distributions is given by

$$I_+ = A \int_o^{r_o} 2\pi r \cos\left(\frac{\pi}{2}\frac{r}{r_o}\right) d r \qquad (22)$$

Using the standard form

$$\int x \cos a x\, d x = \frac{1}{a^2} \cos z x + \frac{x}{a} \sin a x \qquad (23)$$

Equation 22 becomes

$$I_+ = \frac{4 A_o r_o^2}{\pi} [\pi - 2] = 1.4535\ A_o r_o^2$$

and numerically,

$$I_+ = 1.4535\ (10.026)\ (14.5)^2 = 3063.9$$

$$I_{++} = 1.4535\ (5.0132)\ (14.5)^2 = 1532.0$$

$$I_{+o+} = 459.9$$

Comparing the latter two with the computer generated values shown in Table 21 we see the agreement is within about 0.6%.

The ratio of total I_{++} current to the total current is

$$I_{+}/I_{+o+} = \frac{1532}{4595.9} = 0.3333$$

Using eqs. 7 and 8

$$\alpha = \frac{3063.9 + 0.707\,(1532)}{4595.9} = 0.9023$$

$$\beta = \frac{3063.9 + 0.5\,(1532)}{4595.9} = 0.8333$$

which agree exactly with the computer calculations.

Since all the theoretical results agree within a fraction of a percent to the computer generated calculations, we can confidently use this program knowing that any error introduced is negligibly small compared to the expected experimental errors.

REFERENCES

1. W. Knauer, et al., "Discharge Chamber Studies for Mercury Bombardment Ion Thrusters," NASA CR-72440, September, 1968

2. T. D. Masek, "Plasma Properties and Performance of Mercury Ion Thrusters, AIAA Paper No. 69-256, March, 1969, New York, N. Y.

3. R.D. Moore, "Magneto-Electrostatically Contained Plasma Ion Thruster," AIAA Paper No. 69-260, March, 1969, New York, N. Y.

4. J. Hyman, Performance Optimized Small Structurally Integrated Ion Thruster System," NASA CR-121183

5. H. J. King, et al., "Thrust Vectoring Systems," NASA CR-121142

6. D. Zucarro, "A Configurational Analysis of the Effects of Electrode Geometry on the Mass Utilization Efficiency of Ion Thrusters," Interdepartmental Correspondence, Hughes Research Laboratories, Sept. 1973.

7. W. Knauer, "Power Efficiency Limits of Kaufman Thruster Discharges," AIAA Paper No. 70-177, 1970, New York, N. Y.

8. H. J. King, et al, "Low Voltage 30 cm Ion Thruster," NASA CR 120919, February, 1972